A dissertation submitted for the degree of Doctor of Philosophy

Study on Soil-Screw Interaction of Exploration Robot for Surface and Subsurface Locomotion in Soft Terrain

February 2011

by

Kenji Nagaoka

Department of Space and Astronautical Science

School of Physical Sciences

The Graduate University for Advanced Studies (Sokendai)

JAPAN

Acknowledgment

At completing this dissertation, I would like to extend my gratitude to all the people regarding my research activity over the past five years.

Above all, I would like to express my deepest gratitude for my PI, Professor Takashi Kubota. He has always encouraged me to aspire for getting my doctoral degree during research life at the ISAS. I could pursue my studies and enhance my humanity under his distinguished direction. Words cannot describe my gratitude for him.

I would also like to extend my sincere gratitude to my supervisor, Professor Satoshi Tanaka. His suggestions and scientific knowledge brought a different perspective to my research.

I wish to express my gratitude for Professor Ichiro Nakatani, Professor Tatsuaki Hashimoto, Professor Tetsuo Yoshimitsu, Professor Shin-ichiro Sakai, Professor Nobutaka Bando, Professor Masatsugu Otsuki, Dr. Andrew Klesh and Dr. Genya Ishigami. Through my seminar presentations or individual discussions, their valuable suggestions enabled to cultivate my research. In particular, Professor Otsuki helped me conduct various experiments, and he gave me numerous advices in this five years. Without his continual support, I could not complete my dissertation.

I would like to sincerely appreciate Ms. Mayumi Oda, the secretary of the Kubota lab. Her helps allowed me to do my research smoothly. Also, I wish to give my special thanks to my labmates and great alumnae/alumni. Life in the lab with them were very precious to me, and I thank them for having such productive days.

I acknowledge for Shimizu-Kikai, especially President Hideki Yamazaki. His supports and advices enabled me to accomplish this study.

I greatly appreciate Mr. Eijiro Hirohama and Ms. Takemi Chiku, the stuff of the JAXA Space Education Center in 2008. Thanks to their graceful supports, I had participated the NASA Academy 2008 at the NASA Goddard Space Flight Center. That summer was definitely a very pleasurable time for me, and I could lean and experience countless things during the project.

I also express my appreciation all the members of the ISAS football club. The daily exercise with them gives momentary happiness to my hectic life.

Last of all, I am deeply grateful for my parents, Yoshiaki and Junko.

January 31, 2011

Kenji Nagaoka

Abstract

This dissertation addresses an interaction between an Archimedean screw mechanism and soil for surface and subsurface locomotion in soft terrain based on experimental and theoretical analyses. The main objective of this research is understanding of an unknown soil-screw interaction. This research is expected to contribute to an application of a helical screw mechanism to unmanned exploration robots and automated machineries. The screw mechanism elaborated in this dissertation has been an attractive device that enables both traveling (subsurface locomotion) and drilling (subsurface locomotion) in the soft terrain since ancient times. On the other hand, an approach to the interaction has not been enterprisingly discussed because of smooth machine operation by human supports on ground. To accomplish unmanned and autonomous robotic excavation and locomotion on unknown extraterrestrial surfaces, however, it is required to clarify and systematize the interaction. Explicitly considering deformability, failure and nonuniformity of terrains, this research attempts to theorizes the interaction based on not only mechanical dynamics but also soil mechanics and geotechnique. Further, this dissertation elaborates the soil-screw interaction by discussing surface and subsurface locomotion. The surface and the subsurface locomotion make a difference in their propulsive directions to direction of gravitational force. In addition, anisotropical constraints by surrounding soils can generally be assumed around a robot in the surface locomotion. Meanwhile, the subsurface one is governed by isotropical constraints of contact with the soils. The constraints also distribute three-dimensionally. Therefore, interactive mechanics between the screw and the soil differs in each locomotion environment. In this dissertation, the undissolved interaction is elaborated through synthetic discussions of the surface and the subsurface locomotion.

With respect to the surface locomotion, a traveling method by using the Archimedean screw devices is proposed as a new locomotion technique on soft soil. Generally, soil contact reacting on such screw anisotropically distributes. Thus modeling of the complicated contact state becomes a key factor. This dissertation first describes that proposed screwed locomotion method is robust to getting stuck, which is a critical issue for conventional wheeled locomotion. According to this, validity of traveling by the screw on soil is indicated by comparison with a wheel and a track. Then, this research attempts to derive the soil-screw interaction models based on skin friction and terramechanics (soil compression and failure). The simulation analyses of the models show better trafficability and maneuverability of the proposed system. Furthermore, maneuverability experiments were carried out by using a new prototyped robot equipped with dual

Archimedean screw units on sand. Through the laboratory tests, it is confirmed that various maneuvers can be achieved by changing rotational speed of each screw. Summarizing the resulted maneuvers, directions of propulsive force that the prototyped robot exerts are presented. In addition to these tests, trafficability tests of a single screw unit were conducted in sandy terrain to comprehend its characteristics of drawbar pull and slip. The experimental results provide qualitative analyses of the drawbar pull, and thereby the interaction can be discussed. Based upon these considerations, this dissertation indicates applicability and feasibility of the screw mechanism for the surface locomotion on the soft terrain.

With respect to the subsurface locomotion, this dissertation proposes a subsurface drilling robot using the Archimedean screw mechanism. Prior to detailed discussion of the interaction, this dissertation describes an advantage of a subsurface explorer. Moreover, this research qualitatively organizes how a robot achieve drilling motion in complicated subsurface environment. In accordance with this remark, this dissertation indicates effectiveness of the screw mechanism for the subsurface drilling. Then, a novel interaction model between the screw and the surrounding soils is proposed based on soil mechanism with screw geometry. In the interaction modeling, by applying cavity expansion theory, the proposed model includes an increase of soil pressure caused by laterally compressing subsoil. The validity of the model is discussed through experimental analyses. Consequently, the model enables to calculate required torque of the screw with depth. The result is expected to lead not only to understanding of the interaction but also to design optimization of screw geometry. Furthermore, an effective screw mechanism (Contra-rotor Screw Drilling mechanism) is proposed to achieve an efficient self-drilling. The new mechanism is experimentally investigated, and thereby its feasibility and proper conditions are indicated.

In this dissertation, the unknown soil-screw interaction of the Archimedean screw mechanism in the soft terrain is addressed from the standpoints of the surface and the subsurface locomotion. So far, studies on theoretical approaches of the practical application of such screw mechanism have been particularly limited although it is an interesting and useful tool for the locomotion. Therefore, this research is expected to provide an initiative of the screw mechanism. This research fosters the understanding of the complicated soil-screw interaction by discussing the applications in the surface and subsurface locomotion. Additionally, this dissertation makes a significant contribution in the field of general screw mechanism and leads to the design optimization and the motion control. The developed ideas can cover applications of manned/unmanned activities on Earth.

Contents

List of Figures

List of Tables

Chapter 1. Introduction

1.1 Background

Mankind has been attracted to the universe since early times. “The Earth is the cradle of the mind, but we cannot live forever in a cradle.”, the famous line written by K. E. Tsiolkovsky in 1911, a rocket scientist and a pioneer of astronautics in the former Soviet Union. As summarized by his quote, space is now looked on as the new frontier for mankind’s activities. Interest in space has also come from an academic viewpoint, for example, from astronomy or celestial mechanics. Contributions of space development generally cover a lot of disciplines (for instance, space science, life science, material science and engineering). As the first world’s successful space project, in 1957 the Soviet Union launched an artificial satellite into orbit around the Earth. The satellite was named Sputnik 1 (Figure 1.1), and its success began the Moon race between the Soviet Union and the USA [5]. At that time, the Moon race included a prominent political dimension because of the so-called “Cold War”. But, ironically, the race made a sizable contribution to the immediate development of space technology through bountiful budgets. As a result, the USA achieved the first manned landing on the Moon by the Apollo 11 project in 1969. Figure 1.2 shows an astronaut’s footprint on the Moon from this project. After the Moon race era, space development has been shifting from extensive manned missions to relatively small unmanned explorations aiming at scientific research in space science. Within this context, more

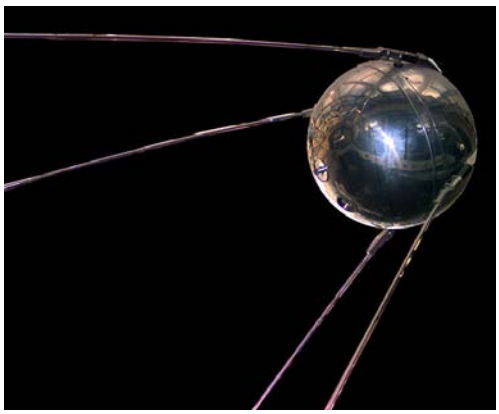

Figure 1.1 : The first world’s artificial satellite “Sputnik 1” ©USSR.

Figure 1.2 : Footprint on the lunar surface ©NASA.

and more countries are currently entering into space development. Furthermore, robotization and automation technology is becoming increasingly central to the space explorations. Space robotics is also developing rapidly with recent progress of science technology. Generally, applications of robotic technologies enable the conduction of challenging tasks in difficult terrains such as volcanoes, rescue sites or extraterrestrial surfaces. A growing number of the robotic technologies will advance future space missions as space robotics leads to accomplishments of precise works with lower cost and risk in the extraterrestrial surfaces. To realize the challenging tasks, however, epoch-making technologies of space robotics are now required.

Originally, the word of "robot" was coined by famous Czech writer K. Čapek in his science fiction play *R.U.R.* (*Rossum's Universal Robots*) which was premiered in 1921. Its etymology is the word "*robota*", meaning labour in Czech. In this play, artificial people were called "robots", and at the beginning, the word was closer to androids or bioroids, unlike the modern idea of robots. Likewise, in 1941, the term "robotics" was first used in science fiction short story *Liar!* written by prolific American writer I. Asimov. The word "robotics" was created as a cross-sectoral term including all the knowledge and technologies with respect to robots. The idea of the robot coined just 90 years ago has currently constituted the bedrock of space development. Here, as expectations for the lunar and planetary exploration by the robotic technology, an importance of surface locomotion technique and sampling materials was noted by Yoshida [119]. In particular, mobile rovers have attracted attention in the actualization of robotic exploration. For upcoming rover missions, the development of robust locomotion and investigation systems for unknown terrains will be a strong requirement in engineering design.

1.2 Motivation

1.2.1 Requirements for Space Robotics

In general, the requirements need to be considered for all components making up the space robotic technologies as follows:

- Small-sized and lightweight system as sending materials into space costs a large amount of money and there is a limit to the transportable volume/mass by rockets.
- Structural simplicity to ensure mechanical and electrical reliability.
- Redundant or robust system to deal with unforeseen situations.
- Thrifty power consumption for reduced availability of electrical power in space.
- Applicability or tolerability to harsh space environments: ultra-high vacuum, thermal condition, gravitational field and space radiation.

Unmanned exploration rovers on the lunar and planetary surfaces cannot rely on human support. Therefore, the rovers must recover from or avoid critical situations by themselves. Also, structural or mechanical reliability of the rovers becomes critical. With respect to future rover missions, an attainment of unmanned surface and subsurface locomotion (*i.e.*, traveling and drilling) in soft terrain covered with fine soils is a key technique. This research focuses on an Archimedean screw mechanism as a prospective structure achieving both the surface and the subsurface locomotion.

1.2.2 Applicability of Archimedean Screw Mechanism

An Archimedean screw spiral is an interesting and useful structure in engineering. Humans have been intensely interested in such a spiral structure since ancient times [46, 57, 65]. The Archimedean screw is a device for moving solid or liquid materials by means of a rotating helical flighting. As can be expected from the name, it is said that its invention is credited to the Greek mathematician Archimedes of Syracuse in the 3rd century BC [65]. Originally, the Archimedean screw mechanism was utilized as a screw-pump [53]. Figure 1.3(a) shows profile of a screw pump. The Archimedean screw pump is a mechanical device for transferring water from a low-lying body of water into irrigation ditches. The screw pump is typically composed of a screw flight and a hollow pipe, and the screw flight is installed inside the hollow pipe. Turning the screw flight and/or the pipe allows one to scoop up a volume of water. Likewise,

the Archimedean screw mechanism has been used for conveying not only liquid but granular materials [49, 56, 58]. As for the screw conveyors, some has studied their theoretical analysis such as a transportation efficiency. However, the screw is fixed and just motions of transported materials is considered.

Traditionally, a screwed drill has been also utilized in field excavation, the so-called earth auger [15, 16, 19]. The earth auger is a mechanical tool for removing soil, clay and shavings of rocks using working fluid by a rotating helical flight. Figure 1.3(b) shows an earth auger machine. Like the liquid in a screw-pump, excavated materials are transported along its rotational axis. While the earth auger excavation has been extensively-employed, its interactive mechanics with surrounding soil remains to be studied. Furthermore, there has been a screwed pile, which is the almost same structure with the earth auger. The screw pile has been applied with the purpose of structural stability against overturning moments, uplift forces, axial compression and lateral forces [24]. Figure 1.3(c) shows the screw piles. The screw piling foundation is becoming a typical technique in everyday construction sites because of its simplicity. The widespread use of the screw pile is attributed to its efficient pile installation rate. The screw pile has a helical flight twisting around a shaft, which is analogous to the screw pump. So far, most theoretical discussions of the screwed pile have been focused on its bearing capability. In this case, a soil-screw interaction is a moot point.

Additionally, since the 19th century, the Archimedean screw has been applied to land and amphibious vehicles [34–37]. Figure 1.3(d) shows the marsh screw amphibian developed by the US army. It has been confirmed that the vehicles provide high trafficability on difficult surfaces consisting of snow, ice, mud, marsh or sand. Specifically the surface locomotion in soil by the screws becomes more complicated than subsurface locomotion due to anisotropy of contact constraint with its environments. Discussions on theoretical soil-screw interaction remains controversial, and also the vehicle's trafficability and maneuverability have not been well understood.

1.3 Purpose and Approach

In accordance with the above considerations, although the Archimedean screw mechanism has been variously-used to machine technology, the soil-screw interaction remains to be elucidated. At present, academic studies on the undissolved interaction are extremely-limited in the world. Elucidation of the interaction is expected to make a contribution to practical enhancements, such as design optimization and drive control of the screw. The main purpose of this dissertation is

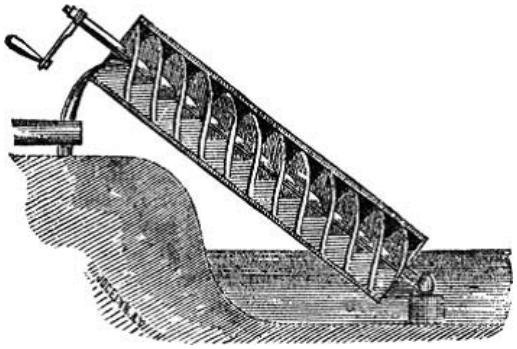

(a) Archimedean screw pump [50].

(b) Earth auger machine ©Hokuriku Eletec Co., Ltd..

(c) Screw piles ©Apollo Piling Systems.

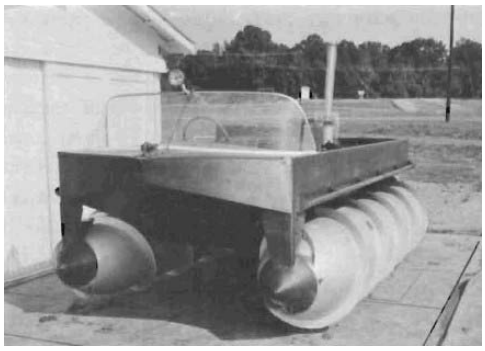

(d) Marsh Screw Amphibian [45].

Figure 1.3 : Practical applications of the Archimedean screw mechanism.

to provide the findings of an interactive mechanics between soil and the screw and to develop a new soil-screw interaction model. This interaction is discussed through considerations of:

- Surface Locomotion (traveling on soft terrain) by the Archimedean screws
- Subsurface Locomotion (drilling into soft terrain) by the Archimedean screws

For subsurface locomotion, the screw's contact constraint normal to a propulsive direction is isotropically-distributed in compressible soils. Meanwhile, for the surface locomotion, the screw is anisotropically-constrained by the soils in three-dimensional space. Therefore, the surface locomotion becomes more complicated for mobile exploration robots. An integrative discussion of both the surface and the subsurface locomotion will exhibit key ideas on the interactive mechanics. The discussion takes into account the screw's different locomotive directions to a gravitational direction.

1.4 Research Contributions

This dissertation focuses on understanding the soil-screw interaction of surface and subsurface locomotion in soft terrain. Compared with conventional screw applications, the characterization of this research is described as shown in Figure 1.4 The main contributions of this research are:

- New initiative of the Archimedean screw mechanism
  With respect to applications to the surface and the subsurface locomotion on the soft terrain, a potential capability of the Archimedean screw mechanism is systematically-studied. Also, advantages of the screw mechanism are qualitatively summarized by comparison with other mechanisms.

- Integrative discussion of the soil-screw interaction
  This dissertation introduces a synthetic idea of the the soil-screw interaction from the viewpoint of the surface and the subsurface locomotion. The interaction is discussed by both experimental and theoretical approaches for each locomotion technique.

- Formulation of the soil-screw interaction
  Mathematical formulation of the interaction is derived, and it contributes to a better understanding of the unknown interactive mechanics. The formulation also leads to optimal design and control of the screw. As for space applications, its reliability can be preliminarily evaluated by using the formulated model.

- Proposal of an effective screw drilling mechanism
  To achieve an efficient screw drilling, this dissertation proposes a new screw mechanism. Its valid conditions are experimentally evaluated.

1.5 Outline

This dissertation is organized into 7 chapters as described in Figure 1.5. The contents of each chapter are briefly summarized as follows:

Chapter 1 introduces the background and the motivation of this research, and then describes the purpose and the approach. Also, the main contributions of this dissertation are mentioned.

Chapter 2 presents mathematical definitions of fundamental screw mechanisms. Moreover, as the historical background, related works of the screw applications to the surface and the subsurface locomotion are reviewed. According to these reviews, new challenges to be discussed

are articulated.

Chapter 3 describes the soil-screw interaction modeling for the surface locomotion by the Archimedean screw mechanism. Ideas on soil-screw interaction models are discussed based on skin friction and terramechanics (soil compaction and shear). In accordance with these modeling concepts, this chapter introduces a novel model by combining skin friction and terramechanics. Unlike conventional locomotion models, the synthetic model can simulate both contact friction and soil behavior.

Chapter 4 presents the surface locomotion system by using the Archimedean screw mechanism. This chapter also proposes the Screw Dive Rover system driven by the Archimedean screw units as a new rover for traveling on the soft terrain. Prior to detailed discussions, advantages of locomotion by the screw unit to conventional locomotion gears (a wheel and a track) are mentioned. Then, in this chapter experimental trafficability and maneuverability of the Screw Drive Rover system are analyzed by laboratory tests. In addition, propulsive forces' directions to be reacted are examined based on the maneuverability and the trafficability. The resulted characteristics are discussed by comparison to simulation results in Chapter 3.

Chapter 5 addresses the subsurface locomotion by the Archimedean screw mechanism. A key strategy of how to move underground is first described qualitatively, and possible mechanisms achieving the strategy are enumerated. On the basis of this consideration, it is indicated that the Archimedean screw is one of the most useful mechanisms for subsurface drilling. Additionally, a novel soil-screw interaction model of the subsurface locomotion is developed. Parametric simulation analyses are conducted to examine the characteristics of the proposed model. The model validation is also evaluated by experimentations and numerical simulations.

Chapter 6 deals with a new effective screw drilling mechanism. To accomplish efficient drilling on the Moon, a contra-rotor screw drilling mechanism is proposed. The mechanical objective of this new mechanism is agitating compacted subsoils and canceling motor reaction torques by an unique structure. The adequacy of this mechanism is evaluated by using energetic indexes through drilling experiments. Furthermore, this chapter proposes a new subsurface explorer by applying the Archimedean screw mechanism, which can burrow into the soil by itself. Its experimental validity is examined with the developed model in Chapter 5.

Chapter 7 summarizes the contributions of this dissertation. Moreover, several future works are described as additional challenges.

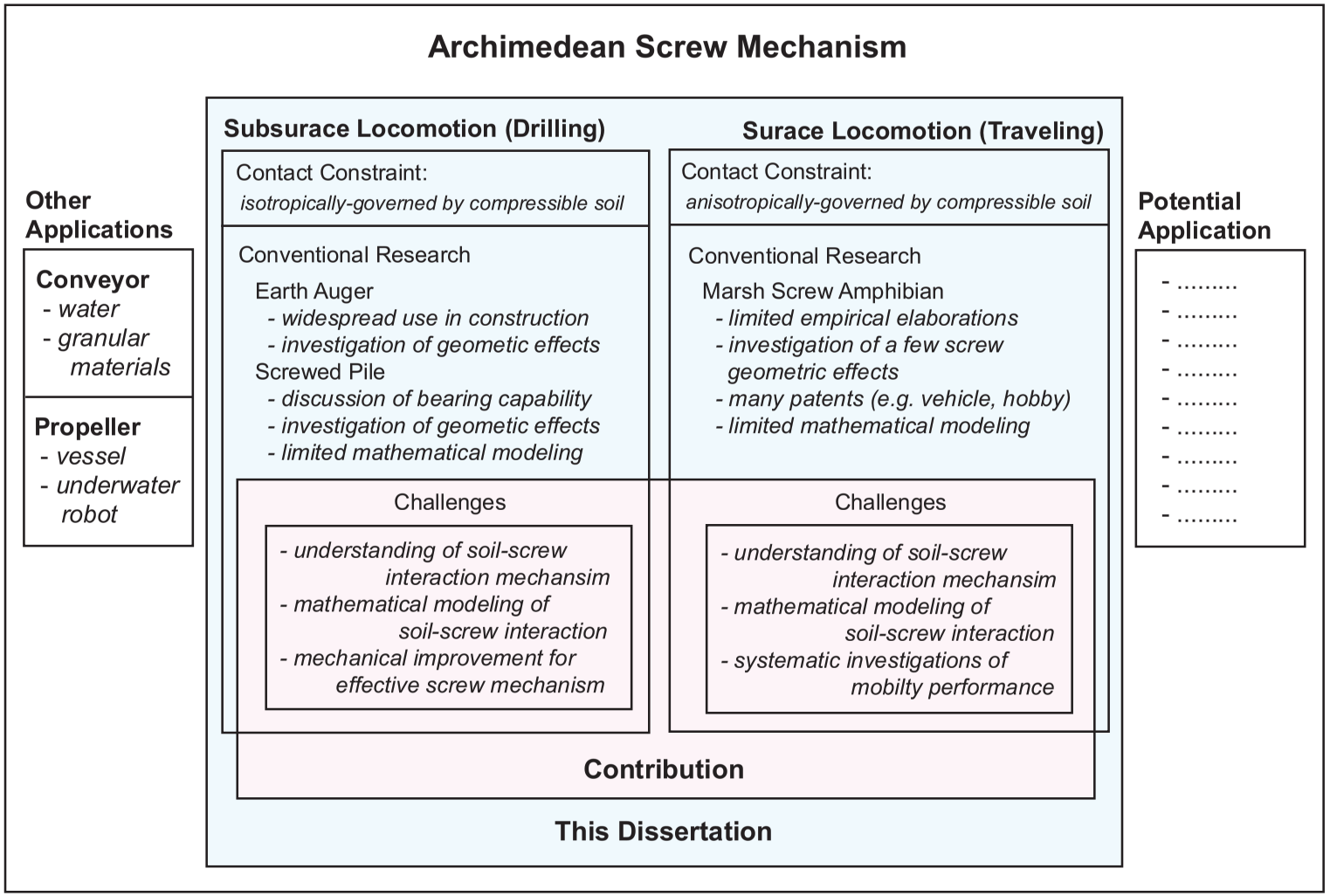

Figure 1.4 : Characterization of this dissertation.

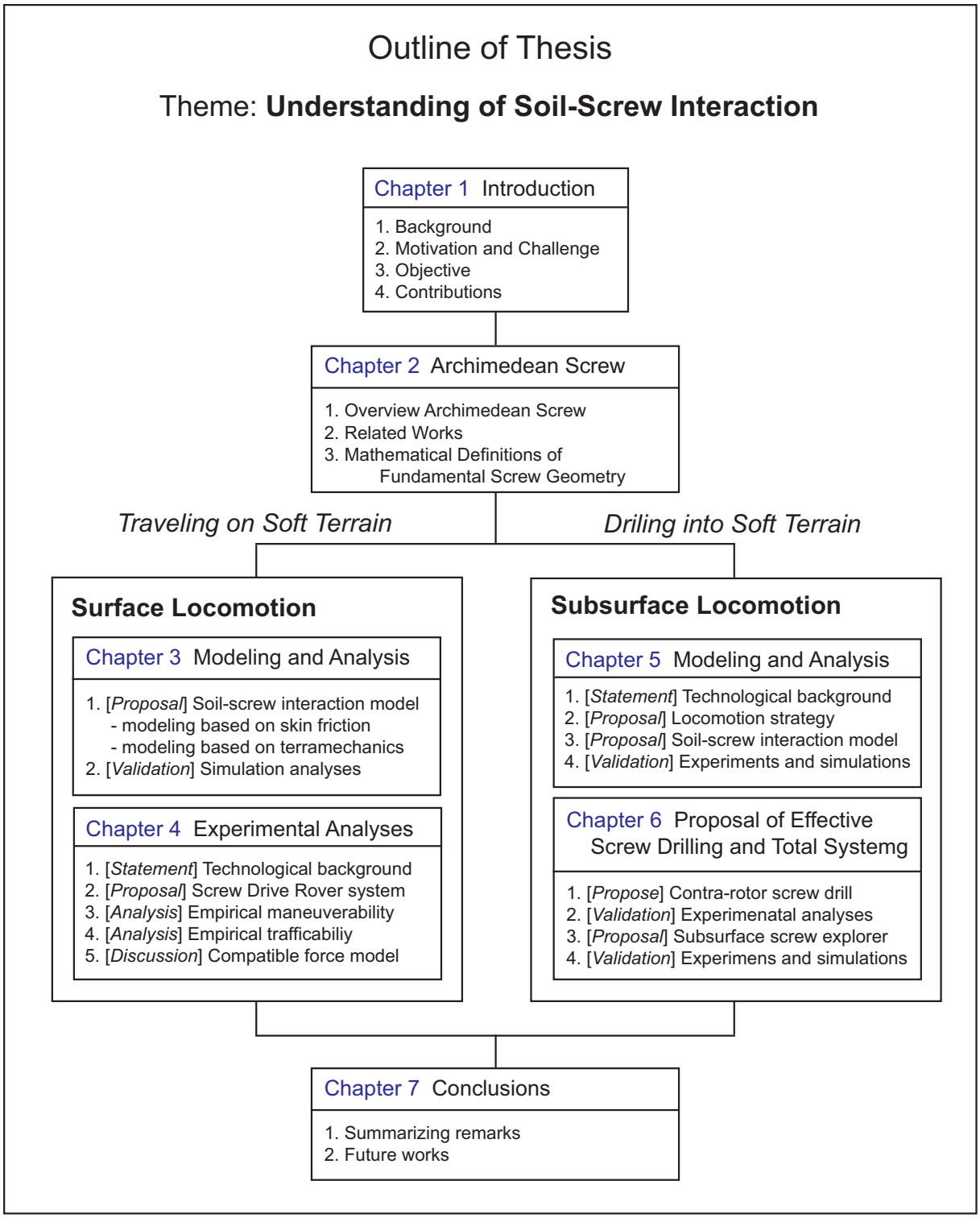

Figure 1.5 : Configured outline of this dissertation.

Chapter 2. Archimedean Screw Mechanism

An Archimedean screw mechanism is an attractive structure and has been used in various applications as described in Chapter 1. This dissertation especially focuses on its application to surface and subsurface locomotion in soft terrain (*i.e.*, traveling on surface and drilling into subsurface). In the meantime, studies on the screw has been quite limited and it includes a lot of missing parts academically. To apply it to deformable terrain such as soil, theoretical and systematic discussions are required. First of all, this chapter derives mathematical definitions of fundamental screw mechanisms as preliminary matters for the subsequent chapters.

2.1 Geometric Modeling of Screw Mechanism

In this dissertation, two types of the Archimedean screw mechanisms are considered: a logarithmic and a cylindrical helix. Here η denotes the constant inclination angle of screw flight at the center position **P** on the screw flights. As common terms, the screw length is L, the maximum inner radius of the screws is r_0 and the maximum screw radius is R_0. In addition, logarithmic and cylindrical screw models can be mathematically expressed as a function of the winding screw angle θ against a cone and a cylinder in Figure 2.1. Also, the screw thickness is neglected. As coordinates, l axis is set to be the central axis of the explorer, and r is defined as the distance from l axis as shown in Figure 2.1, respectively. Furthermore, l denotes the height from the apex of the screw and θ is set to be zero at the highest position of the screws. At a winding angle θ, r_c, r_s, and r_{sc} are defined as the inner screw radius, the outer screw radius, and the distance from l axis to **P**, respectively. The mathematic models of the helices can be defined as follows.

$$\mathbf{R} = \begin{cases} \mathbf{R}_L \exp(a\theta) & : \text{Logarithmic Helix} \\ \mathbf{R}_C & : \text{Cylindrical Helix} \end{cases} \tag{2.1}$$

and also,

$$\begin{cases} \mathbf{R} &= \left[r_c(\theta) \quad r_s(\theta) \quad r_{sc}(\theta) \quad l(\theta) \right]^T \\ \mathbf{R}_L &= \left[r_0 \quad R_0 \quad R \quad L \right]^T \\ \mathbf{R}_C &= \left[r_0 \quad R_0 \quad R \quad L - \dfrac{p\theta}{2\pi} \right]^T \\ R &= \dfrac{r_0 + R_0}{2} \end{cases} \tag{2.2}$$

where p is the screw pitch and the function parameter a is negative (*i.e.*, $a < 0$). Thus **P** can be represented as a function of r_{sc} and l in r-l coordinates. Figure 2.2 shows examples of a cylindrical and a logarithmic helix based on Eq. (2.1).

2.1.1 Screw Slope Parameter

This section introduces a method to derive geometric screw slope parameter a. The slope angle η at the point **P** on the screw flight is set to be a constant value. According to this condition, the functional parameter a can be described as a correlation function of η by differentiating **P**. Given a constant η, a is derived as follows.

$$a = \frac{-R \tan\eta}{\sqrt{(L + R\tan\eta)(L - R\tan\eta)}} \tag{2.3}$$

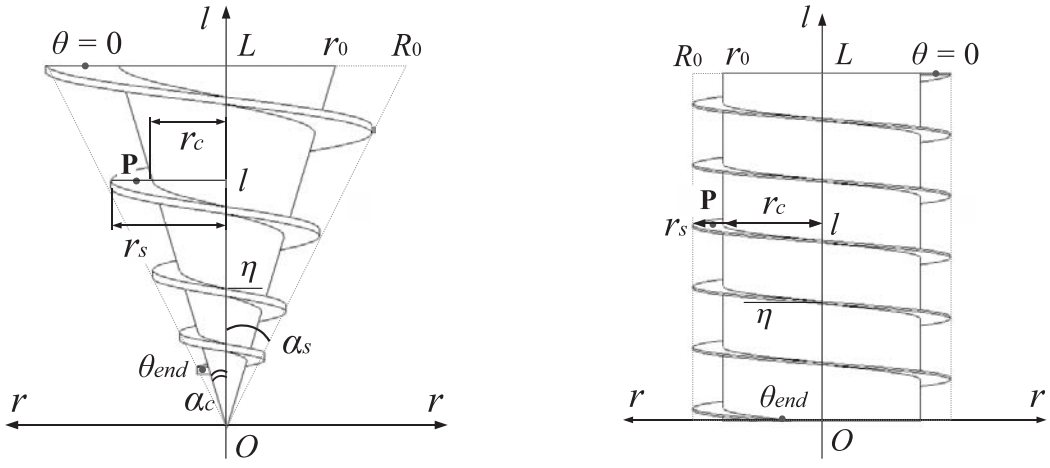

(a) Logarithmic helix. (b) Cylindrical helix.

Figure 2.1 : Geometric models of screw helices.

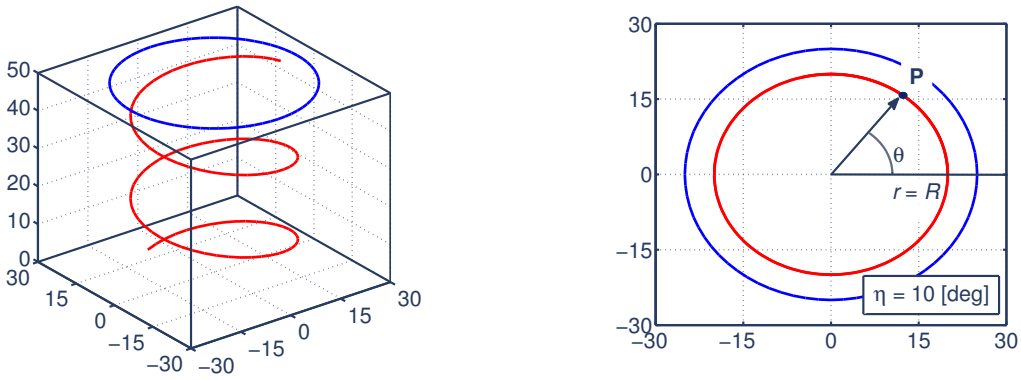

(a) Cylindrical helix.

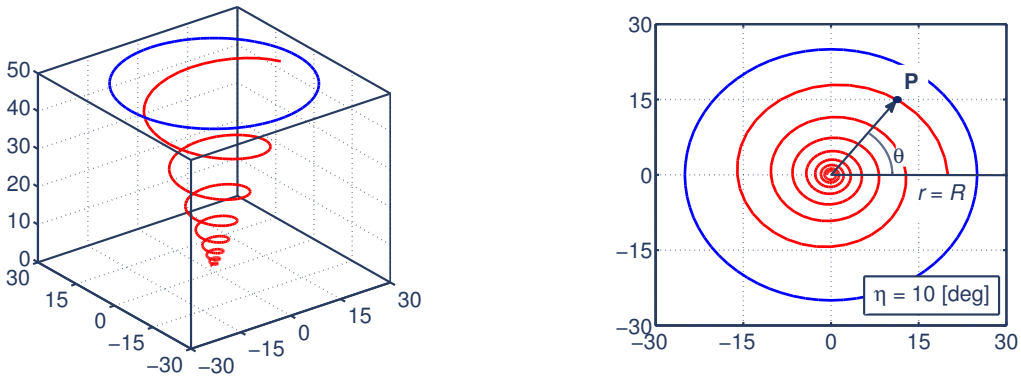

(b) Logarithmic helix.

Figure 2.2 : Mathematical drawing of screw helices.

2.1.2 Screw Pitch

While the screw pitch p of a cylindrical helix is constant, but the effective p of the logarithmic helix becomes a variable value at θ. The helical screw pinches correspond to the vertical intervals between the screw flights. The pitch p of the cylindrical and logarithmic helices can thus be defined as a differential of l between θ and $\theta - 2\pi$ as follows.

· Cylindrical Helix:

$$p = \begin{cases} \theta R \tan\eta & : 0 \leq \theta \leq 2\pi \\ 2\pi R \tan\eta & : \theta > 2\pi \end{cases} \tag{2.4}$$

· Logarithmic Helix:

$$p = \begin{cases} L\,[1 - \exp(a\theta)] & : 0 \leq \theta \leq 2\pi \\ L\,[\exp(-2a\pi) - 1]\exp(a\theta) & : \theta > 2\pi \end{cases} \tag{2.5}$$

For the Archimedean screw models, the pitches are constrained by the screw length L at the initial point $\theta = 0$.

2.1.3 Screw Surface Area

An upper surface area of the screw flight is principal geometric information for discussing the screw dynamics since it denotes an interacting area between the screw surface and the soil. The upper surface area of the screw flight enclosed by an angle θ to $\theta + \Delta\theta$ is defined as $\Delta A_{sc}(\theta)$. The surface area is assumed to be the difference between surface areas approximated by triangles. Therefore, $\Delta A_{sc}(\theta)$ can be calculated as follows.

· Cylindrical Helix:

$$\Delta A_{sc}(\theta) \approx \frac{R_0^2 - r_0^2}{2} \cdot \Delta\theta \tag{2.6}$$

· Logarithmic Helix:

$$\Delta A_{sc}(\theta) \approx \frac{R_0^2 - r_0^2}{2} \exp(2a\theta) \cdot \Delta\theta \tag{2.7}$$

2.1.4 Slip

The intrusion or the locomotion speed in a longitudinal direction of the screws and the screw rotational speed of the screw are defined as v and f. With these parameters, the slip s [19, 43], which denotes the intrusion depth or the traveling distance for one screw rotation as to the screw pitch, can be defined as follows.

$$s = \frac{pf - v}{pf} \iff sp = p - \frac{v}{f} \tag{2.8}$$

2.2 Related Works

2.2.1 Historical Background of Screw Vehicles

So far, the Archimedean screw mechanism has also been applied to land vehicles and amphibians since around the 19th century, and there have been several patents in regard to such screw vehicles [34–45, 64]. Figure 2.4 shows some of past screw vehicles. Generally, the vehicles provide high trafficability in a difficult surface consisting of snow, ice, mud, marsh or sand. The vehicles are particularly expected to be robust to slipping and getting stuck in soft soil since the mechanism can forge ahead even if it is buried in the soil. Together, their inclined screw flights lead to movement in various directions. Compared to a track, its structural simplicity is a decided advantage in unmanned rovers. Meanwhile, studies on the screw mechanism or the

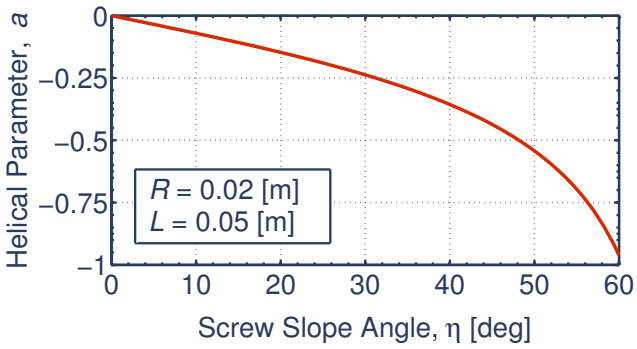

(a) Relationship between a and η.

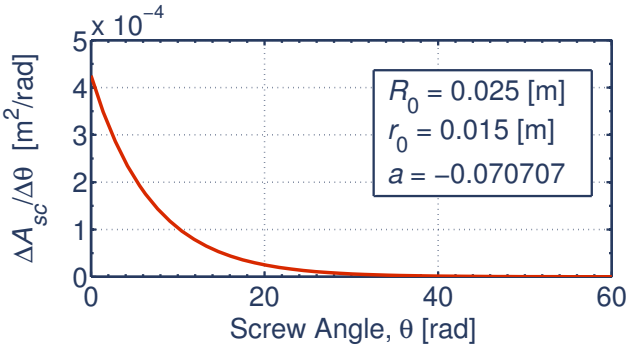

(b) Relationship between $\Delta A_{sc}/\Delta\theta$ and η.

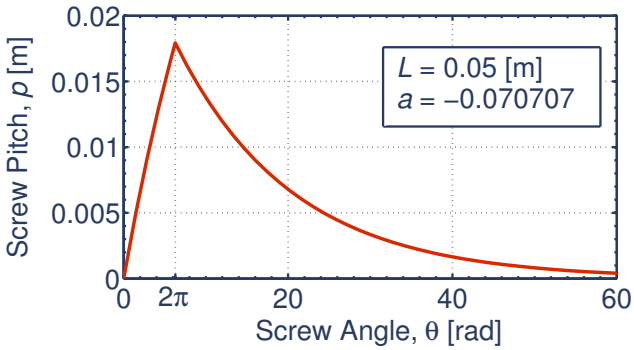

(c) Relationship between p and θ.

Figure 2.3 : Functional behaviors of logarithmic screw geometry.

vehicle have been extremely limited [38, 41, 43, 64]. Consequently, an actual soil-screw interaction remains to be elucidated from academic viewpoint. In such background of the vehicles, theoretical discussions of the screw vehicle have been conducted by Cole [38]. This work has attempted to analytically model and evaluate the vehicle's traction performance on sand, but its model was developed based on just skin friction and ignored both slippage and soil shear phenomena. Therefore, the model is inadequate to be applied. On the other hand, Dugoff *et al.* [43] especially examined the characteristics between translatory traction and a slip of a single screw

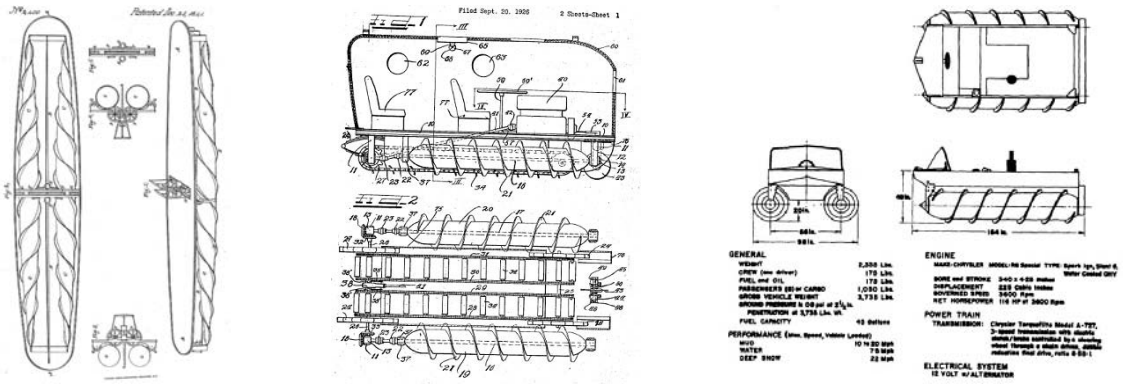

(a) Patent by Wells [34]. (b) Patent by Code [37]. (c) Marsh screw amphibian [40].

Figure 2.4 : Various types of marsh screw amphibians.

rotor by model tests. Their contributions suggested important remarks, which reported the effect of screw geometry, load and velocity on the characteristics. But its applicable scope would be confined to straight movement, and also researches on the soil-screw interaction are lacking. Consequently, the vehicles' synthetic trafficability on the soil is less well understood. For this reason, a new challenge of comprehending the soil-screw interaction comes for a practical application of the screw.

Likewise, there have been several robots using a spiral mechanism, for instance, an *in vivo* robot for laparoscopy [54, 55], a robotic endoscope [60, 62], a rotational rheometer [47] or a swimming micro-machine [48, 51, 52]. These devices move by contact with viscoelastic biological tissue or incompressible viscous fluid. Although these are equipped with the spiral mechanisms analogous to the Archimedean screw for locomotion, their targeted environments are quite different from soil. Further, mobile devices using a helical pipe/coil have been also developed [61, 63]. Their targets are outdoor soft surfaces [63] and wetlands [63], respectively. The device proposed in [63] is a patent, and thus its theoretical locomotion principle has not been considered. Understandably, their interactive models essentially differ from the the soil-screw interaction as well. Hence, individualistic modeling is practically required for each application.

This dissertation focuses on the derivation of the novel soil-screw interaction model for surface locomotion. In particular, a novel mobile rover system, which is driven the Archimedean screw units, is proposed for discussing the interaction. To understand its fundamental mobility performance, modeling and analysis of the interaction are first conducted. Next, this dissertation investigates trafficability of the single screw unit and maneuverability of the rover. The trafficability and the maneuverability are examined through laboratory tests. These empirical mobility performances will also provide important ideas for modeling the interaction.

2.2.2 Historical Background of Screw Drilling

The screw drilling devices basically consist of a single unit with a cylinder/cone and a continuous helical screw flighting. Until now, they has been used as ground applications to construction field such as an earth-auger (*e.g.* [15, 16, 19]) and a screw pile (*e.g.* [24]) as described in Chapter 1. Initially, a auger drilling tool was used as a grain auger agriculture to move grain from trucks and grain carts into grain storage bins. It is said the modern grain auger was first prototyped by Peter Pakosh in 1945. On the other hand, the original screw pile was invented by Irish engineer Alexander Mitchell in 1833 [24]. Although its structural design was simple, the screw pile was utilized as effective means of construction for lighthouses, beacons, moorings and other structures on muddy banks or shifting sands.

In general, these screw devices have the following important capabilities for a subsurface drilling technique:

- Backward fore-soil removal and transportation (achievement of making a space)
- Genesis of assisting force for intrusion by transporting fore-soil
- Dust prevention mechanism

The Archimedean screw mechanism is one of the most prospective drilling tools. Basically, a machined thread is superior in terms of intrusion with cutting materials. However it is not great at generating propulsive force by screw rotations because of the thread profile. Therefore, screw flights composed of flat and helical blades have been adopted as described in the subsequent subsections. Such screw mechanism is particularly expected to be suitable for drilling into compacted soil layer.

Meanwhile, many theoretical parts of the screw drilling remain to be elaborated. So far, there have some theoretical approaches [18, 19, 23, 30]. Hata *et al.* [18, 19] and Slatter *et al.* [23] have discussed the soil-screw interaction of the screw drilling. However, their models involve many theoretical insufficiencies as to definitions of forces, and the practical applicability of the models are not clear. Additionally, Fukada *et al.* [30] have studied the soil discharging model. In the modeling process, the soil-screw interaction has been also represented as preliminary definitions. But the model also includes lacking parts of acting forces and an unknown force remains to be defined. As for the screw piles, some have also addressed theoretical discussions [21, 22, 28, 29, 31, 32]. The theoretical analyses on the screw piles have particularly focused on an evaluation of their bearing capability. Accordingly, most of them have not modeled the soil-screw interaction. For realizing an effective and autonomous screw mechanism, its

modeling is a new challenge. Unlike most ground applications, unmanned exploration robots do not allow for human intervention. Therefore, mechanical reliability and high efficiency based on theoretical analyses should be proved for practical applications of the screw.

This dissertation aims at the derivation of the novel soil-screw interaction model for subsurface drilling. The model is introduced based on soil mechanics with screw behavior. Unlike the surface locomotion model, influences in a direction of gravitational force are particularly involved. Of particular note is that the fundamentals of the model is analogous to the model for surface locomotion.

2.3 Summary

Understanding an interactive mechanics between a mechanical tool and environment is quite important for unmanned robotic explorations. Not only the screw mechanisms, but all the tools in the soft terrain need mathematical modeling in order to efficiently use them. In this chapter, prior to detailed discussions of the soil-screw interaction, some of geometric and kinematic definitions of the helical screws were introduced. By considering them, the interaction models will be provided as functions of the screw geometry. Furthermore, the historical backgrounds with respect to screw drilling and screw vehicles were introduced from the viewpoint of their theoretical frameworks. According to these remarks, the necessity for developing a new interaction modeling was pointed out. This chapter reaffirmed that the development of the soil-screw interaction model is the key challenge to be addressed.

Chapter 3. Modeling of Screw Surface Locomotion

3.1 Challenge Statement for Robotic Surface Locomotion

Robotic exploration by mobile rovers has received attention worldwide for the achievement of progressive space missions. In the history of space exploration, Lunokhod 1 and 2 built by the Soviet Union were the first unmanned rovers [113, 115, 116]. These huge rovers moved onto the lunar surface in 1970 and 1973, and were teleoperated from Earth. Recently, the Sojourner rover [117] and the Mars Exploration Rovers (MERs) [123] operated by NASA have performed impressive exploration activities on Mars. They employ six wheels for traveling over the Martian surface, and the MERs have especially acquired scientific findings for more than 6 years [124, 126, 138]. In their locomotion mechanism, these three rovers have the rocker-bogie suspension mechanism to traverse rocky terrains [125]. Until now, there have been some lunar and planetary rovers adopted in actual missions as shown in Table 3.1 and Figure 3.1. Most of them employ wheels as their locomotion system because of reliability, simplicity and efficiency. Although the wheels were not selected to especially move on an asteroid's surface under microgravity (*e.g.*, PROP-F [116, 118] or MINERVA [121]), the wheels have contributed most to the exploration rovers (see Table 3.1). Meanwhile, the MER Spirit rover, one of the two MERs, has been mired in a Martian version of quicksand since May 2009 [13, 137]. Mission engineers have investigated how the rover might extricate itself from the sand trap by indoor experimentation and computer simulation as shown in Figure 3.2. However, on January 2010, it was announced NASA ended its removal attempts [14]. This result dramatically indicates limitations of wheeled locomotion on soft soil such as lunar and Martian regolith. Therefore, advanced gears or improved wheels must be newly developed to cope with such a difficult terrain due to the tractive limitations of the wheel discussed in Appendix B.

Generally, typical locomotion gears are classified into wheeled, tracked and legged locomotion. There have been some proposals of tracked rovers [74, 135, 136] and legged rovers [122]. In addition to these typical ones, hybrid-typed locomotion gears have also been considered, such as a leg-wheel [129, 131] or a leg-track [139]. For now, the hybrid-typed gears would have just

Table 3.1 : Achievements of unmanned exploration rovers.

	Landing Year	Target	Mass	Locomotion System	Traveling Distance	Nation
Lunokhod 1	1970	Moon	759 [kg]	8 wheels	10.54 [km]	USSR
PROP-M[1]	(1971)	Mars	4.5 [kg]	walking	-	USSR
Lunokhod 2	1973	Moon	840 [kg]	8 wheels	37 [km]	USSR
PROP-F[2]	(1988)	Phobos	45 [kg]	hopping	-	USSR
Sojourner	1996	Mars	10.5 [kg]	6 wheels	52 [m]	USA
MER Spirit	2003	Mars	185 [kg]	6 wheels	7.73 [km]	USA
MER Opportunity	2003	Mars	185 [kg]	6 wheels	24.8∼ [km]	USA
MINERVA[3]	(2005)	Itokawa	591 [g]	hopping	-	Japan

the leg, the wheel and the track, and thus they do not seem to lead to a system with synergistic effect of the two locomotion gears. In the meantime, an elastic wheel [80] has been considered as one of the possible solutions for improving trafficability of the rigid wheel. For space applications, however, it is problematic to use conventional pneumatic wheels because of a difficulty in handling air and rubber in space missions. Therefore, elastic the wheels made from metal are now being studied [93, 96]. Although the elastic wheels are better than the rigid ones, several challenges still remain to completely avoid getting stuck in the soil. In other proposals for rover locomotion system, the PROP-M rover [116, 128] (Figure 3.1(b)) and TETwalker [133] were proposed. These are very unique walking rovers unlike static walking robots on Earth.

On another hand, as a mechanism somewhat similar to the screw, there is so-called "Mecanum Wheel" invented by B. Ilon in 1971, when he was an engineer with the Swedish company Mecanum AB [114]. The mecanum wheel is now a famous gear in omni-directional robots. Previously, kinematics of the mecanum wheel moving on floor has been mainly discussed with its geometry [130]. Meanwhile, a rover adopting these wheels, named Mars Cruiser One, is being intensively investigated in Europe. Ransom *et al.* [134] has experimentally studied traction capability that the mecanum wheel testbed produces on sand. To translate the mecanum wheels into practical applications on the sand, however, much more deliberations are necessary to grasp

[1]The PROP-M rovers were employed in the Mars 2 and 3 missions operated by the Soviet Union, but the PROP-M rovers could not be deployed on Mars due to the demise of the landers [116, 128].

[2]The PROP-F rover was carried by the Phobos 2 spacecraft for Phobos, the moon of Mars, but the spacecraft went astray before reaching Mars due to the communication fault by a malfunction of the on-board computer [10].

[3]MINERVA (MIcro/Nano Experimental Robot Vehicle for Asteroid) was carried by the Hayabusa spacecraft exploring the asteroid Itokawa, but MINERVA's landing onto the surface was unsuccessful [12].

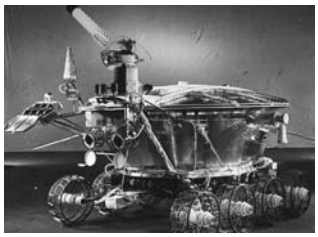

(a) Lunokhod 1 ©Lavochkin Association.

(b) PROP-M rover ©VNII Transmash.

(c) Sojourner ©NASA/JPL.

(d) MER ©NASA/JPL.

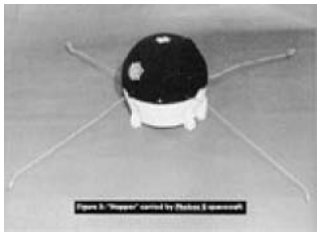

(e) PROP-F rover [11].

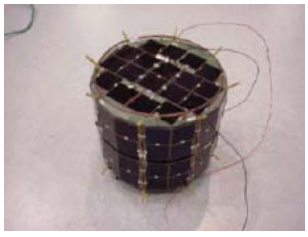

(f) MINERVA ©JAXA/ISAS.

Figure 3.1 : Space exploration rovers launched in past and current missions.

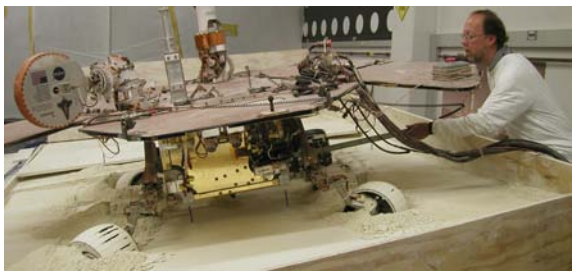

(a) Indoor experimentation.

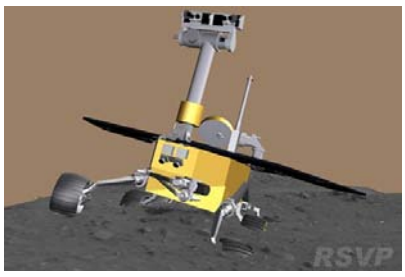

(b) Computer simulation.

Figure 3.2 : Trial-and-error approach for extricating the stuck Spirit rover ©NASA/JPL.

a complex soil-wheel interaction.

Further to these mechanisms, an innovative crawler vehicle, named Omni-Crawler, has been proposed by Tadakuma *et al.* [132]. Omni-Crawler is capable of sideways movement by using new circular cross-section units instead of traditional tracks. But crawler vehicles or tracked robots essentially consist of a lot of mechanical components, and potentially have soil clogging problem. Consequently, such a system has not been selected for rover missions due to its efficiency and reliability. Summing up, future rovers will clearly need innovative and simple locomotion gears that can prevent them from being trapped into quicksand. A better solution that meets such demand is still being sought worldwide.

This research elaborates an applicability of the old and new locomotion method using the Archimedean screw mechanism. Firstly, performance comparison of the screw mechanism with

Table 3.2 : Performance comparison of single locomotive gears on soil.

	Locomotive Directions	Tractable Contact Surface Area	Structural Simplicity	Slip & Sinkage → *getting stuck*
Wheel	backward/forward	upper half	simple	sensitive
Track	backward/forward	upper half	complex	middle
Screw	diagonally backward/forward	whole	simple	insensitive

a single wheel and a single track on soil is discussed especially from the standpoint of robustness to getting stuck into soft soil. From the comparison as shown inTable 3.2, the screw is robust to getting stuck due to its structure symmetrical to the rotational axis. Therefore, the screw is able to exert an enough propulsive force even it completely buried into the soil. The screw also needs a small number of mechanical component, and then, this advantage enhances the structural simplicity and the reliability of the rover system. To conclude, the screw is a feasible candidate for traveling on the soil.

3.2 Principle of Fundamental Surface Locomotion

To achieve robotic locomotion on rigid surface such as indoor floor or paved road, a mobile robot needs to exert a propulsive force. As shown in Figure 3.3, the force is basically divided into frictional contact with the ground, external force with environment (without ground contact) or additional thruster from the robot. However, moving on the surface accompanies frictional effects against the ground as thrust or resistance. In such locomotion, the frictional propulsion has been the most common method. Given a locomotion gear drives on the ground, the reaction force F_R exerted by the ground contact friction has the following relation.

$$0 \leq F_R \leq \hat{\mu} m_r g \tag{3.1}$$

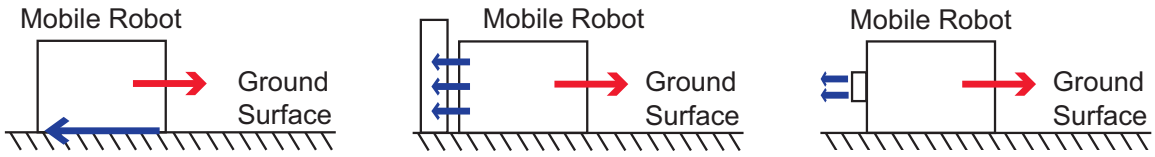

(a) Friction against ground. (b) External contact. (c) Additional thruster.

Figure 3.3 : Method of propulsive force for locomotion on rigid ground.

where m_r is robot mass, $\hat{\mu}$ is a static frictional coefficient between the robot and the ground, and g is a gravitational acceleration. Also, $m_r g$ is a normal force and thereby $\hat{\mu} m_r g$ acts as a static friction. Because deformability of the surface can be ignored, the reacted force F_R is determined not by a contact surface area of the robot but by only the total mass m_r. Therefore, DOFs (degrees of freedom) of a direction of a propulsive force become significant in robotic surface mobility on the rigid ground.

In the meantime, on deformable terrains, shape and behavior of contact surface of a locomotion gear is an indispensable factor for discussing robotic mobility. On the basis of the literature [85], it has been described that tractive performance of a tracked vehicle is better than one of a wheeled vehicle even if they have the same contact surface area in total. This difference is attributed to motion trajectory of the gear's contact surface. Despite Eq. (3.1), the surface locomotion principle on soft terrain is dependent highly on terrain characteristics. Therefore, the locomotion principle encompassing soil mechanics is necessary in practice.

3.3 Proposal of Screw Drive Rover System

This research has proposed and developed a novel rover using dual Archimedean screw units, named Screw Drive Rover. The rover is composed of a main body, hinge legs, and sinistral and dextral screw units. As for the screw unit, a helical screw flight is attached along a cylindrical shaft. The screw flight sets to be wound $\overline{N}$-times around the shaft. Further, the rover can improve its attitude stability by driving the hinge legs in synchronization. In principle, the screw units are capable of propelling the rover although they are buried into soil. Accordingly, the rover is potentially robust to slipping and getting stuck. Employing the two screw units also enables the rover to maneuver on soil.

This dissertation has developed the Screw Drive Rover prototype. Its schematic is shown in Figure 3.4. The screw slope angles are designed to be 16 degrees ($\overline{N} = 4$). The total system weights 6.4 kilograms without circuits and batteries, and its dimension is illustrated in Figure 3.4(a). The prototype has three identical DC motors (RE-max 29-22W-24V; Maxon Motor ag) with planetary gear heads (GP32C-190:1; Maxon Motor ag) and encoders (MR-ML-256; Maxon Motor ag). Two motors are separately built in the screw units respectively, and another one is carried inside the body to drive the hinge legs as illustrated in Figure 3.6. The prototype also has one motor-controller (iMCs01; iXs Research Corp.) and three motor-drivers (iMDs03; iXs Research Corp.), which are powered by Li-Ion batteries connected to DC/DC converters embedded in the body.

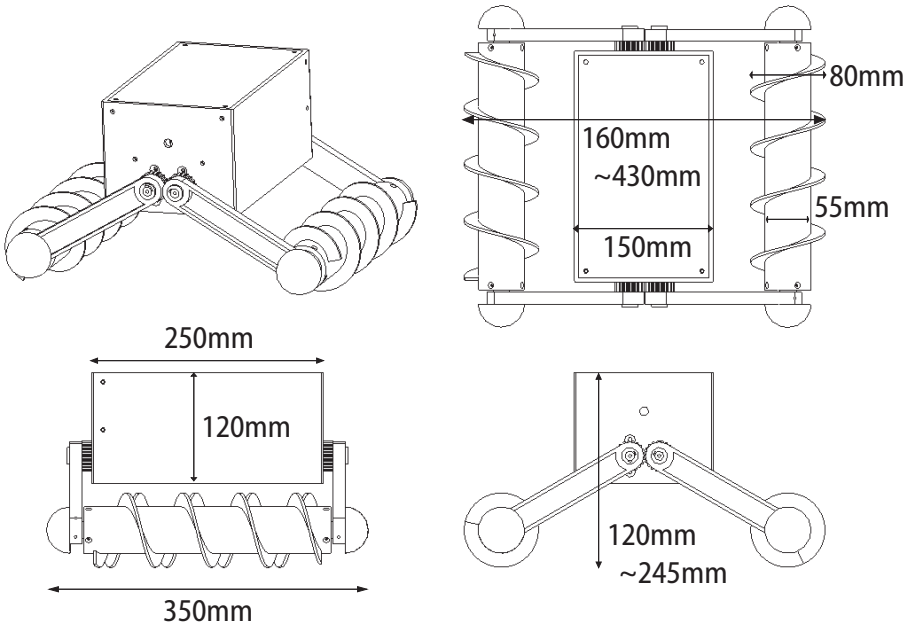

(a) 3D CAD drawing.

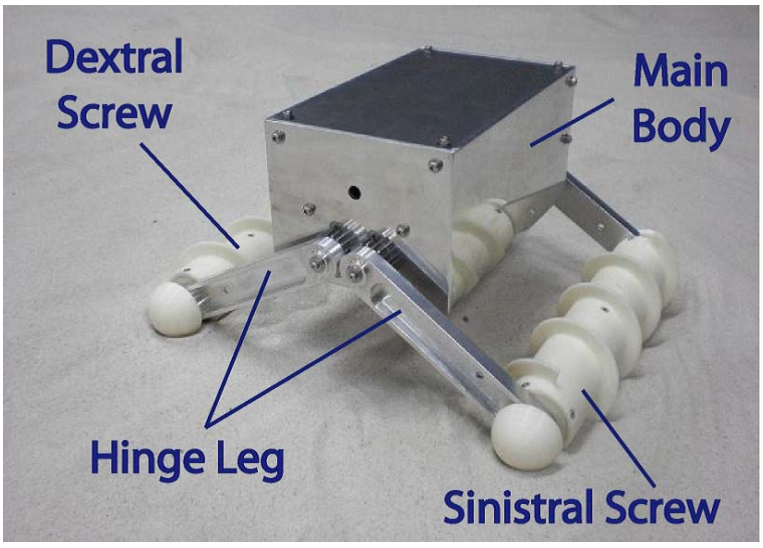

(b) Prototype overview.

Figure 3.4 : Schematic of Screw Drive Rover system.

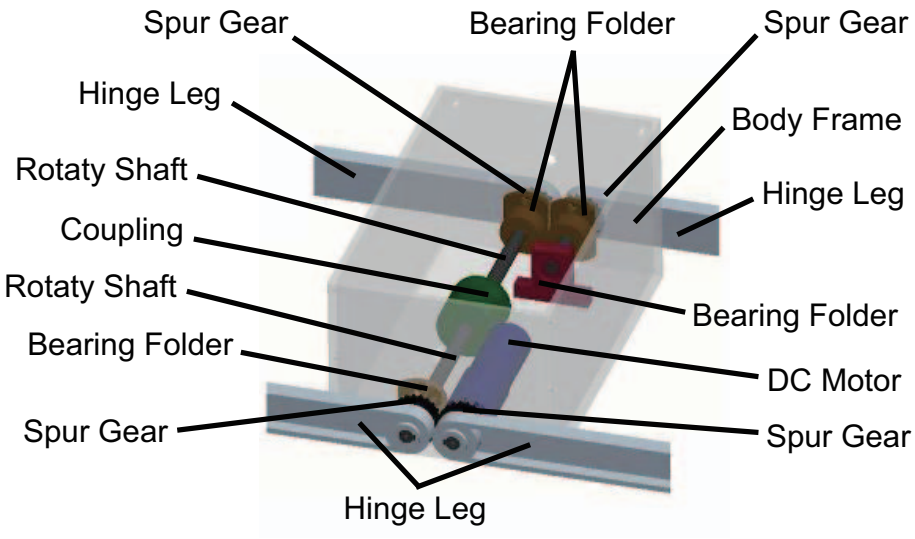

(a) Internal structure of main body and hinge legs.

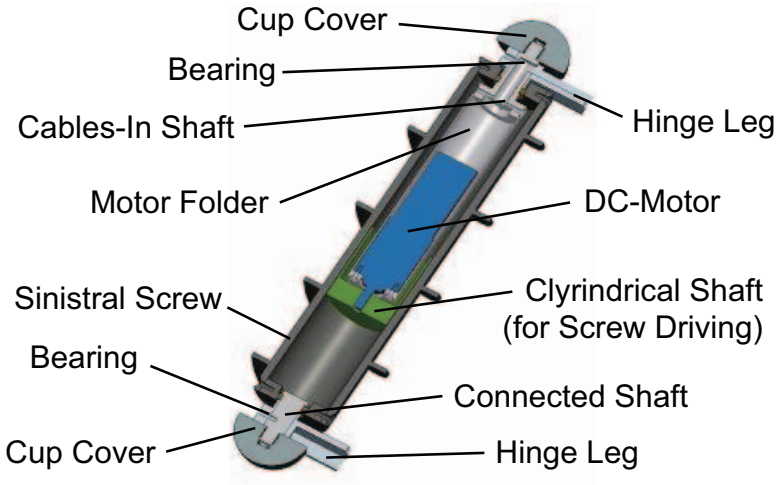

(b) Cross-section diagram of screw drive unit.

Figure 3.5 : Mechanical structure of Screw Drive Rover.

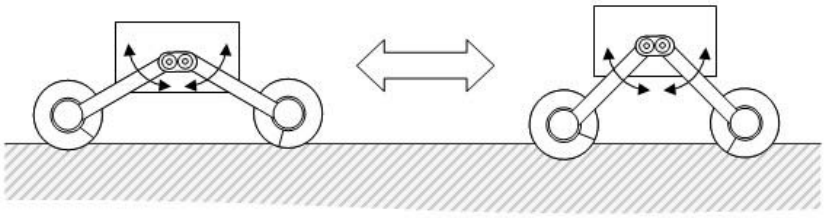

Figure 3.6 : Illustration of moving hinge legs (front view).

3.4 Mobility Analysis based on Conventional Ideas

A mathematical model of the soil-screw interaction enables to predict and control the motion of the mobile rover in unknown environment. The modeling is also expected to lead to an optimized design of the screw mechanism with mission requirements such as limitations of power, size and weight. Accordingly, this work makes the rover missions more efficient. On the other hand, the discussions of the modeling of the screw locomotion have been extremely limited until now. So this dissertation attempts to derive a novel mathematical model of the soil-screw interaction for land locomotion. In this section, the interaction modeling based on skin friction and terramechanics is conducted as conventional locomotion principles. These models provide fundamental ideas of the soil-screw interaction, and are eventually integrated into the synthetic soil-screw interaction model in the next section.

3.4.1 Skin Friction Model

To discuss the mobility performance of the rover, the skin friction model is first analyzed by numerical simulations. The model is defined by just skin friction acting on the screw flight and the cylindrical part. Generally, the coefficient of the skin friction between the screw and the soil is constant, regardless of rubbing velocity. According to the model analysis, the modeled rover achieves various motion trajectories by using the two screw units. Of particular note is that such diverse maneuverability has been demonstrated in the real screw locomotion system. As a first step of the soil-screw interaction modeling, this section addresses the modeling and its analysis based on the skin friction.

Figure 3.7 illustrates the simplified dynamics model of the Screw Drive Rover system. Here this model assumes the screw flight is wound 4 revolutions ($\overline{N} = 4$) around the cylindrical parts. The translational EOMs (equations of motion) of the rover's COM (center of mass) in the rover

coordinates $\Sigma\{X_m, Y_m, \delta\}$ are derived as follows.

$$m_r \ddot{X}_m = \sum_{i=1}^{\overline{N}} \mathrm{sgn}(\omega_r)(f_r - F_{ri}\sin\eta_r) + \mathrm{sgn}(\omega_l)(f_l - F_{li}\sin\eta_l) - C_X R_X \tag{3.2}$$

$$m_r \ddot{Y}_m = \sum_{i=1}^{\overline{N}} \mathrm{sgn}(\omega_r) F_{ri}\cos\eta_r - \mathrm{sgn}(\omega_l) F_{li}\cos\eta_l - C_Y R_Y \tag{3.3}$$

where m_r is the rover mass, $\ddot{(*)}$ is a second order differential of $(*)$ regarding time t, η_j (where $j = r,l$) is the right ($j = r$) or the left ($j = l$) screw angle, and ω_j (where $j = r,l$) is the angular velocity of the screws. Coefficients of signal functions $C_X = \mathrm{sgn}\left(\dot{X}_m\right)$ and $C_Y = \mathrm{sgn}\left(\dot{Y}_m\right)$ are also applied. In addition to these definitions, f_j and F_{ji} are defined as the propulsive forces of the cylindrical part and the screw flight, respectively. R_X and R_Y are also the frictional resistances against the rover motion in X and Y directions.

Next, the rotational equation around the rover's COM is derived by

$$I_r \ddot{\delta} = \sum_{i=1}^{\overline{N}} \mathrm{sgn}(\omega_r) F_{ri} r_{ri} \cos(\eta_r - b_{ri}) + \mathrm{sgn}(\omega_l) F_{li} r_{li} \cos(\eta_l - b_{li}) - C_\delta R_\delta L_W \tag{3.4}$$

and also,

$$\begin{cases} \eta_r = \eta_l = \eta & : \eta = \text{const.} \\ b_{ji} = \arctan\left(\dfrac{L_{ji}}{L_W}\right) & : j = r,l \\ r_{ji} = \sqrt{L_{ji}^2 + L_W^2} & : j = r,l \\ L_{ji} = \left|\dfrac{L}{2} - (i-1)p - p\sin\theta_j\right| & : j = r,l \end{cases}$$

where I_r is the inertia of moment around the COM, δ is the rotation angle around the COM, r_{ji} (where $j = r,l$) and b_{ji} (where $j = r,l$) are the distance and the angle from the COM to the acting point of F_{ji} (where $j = r,l$) respectively. Furthermore, L_W is the distance from the COM to the center of the screws, $\dot{\theta}_r = \omega_r$ and $\dot{\theta}_l = \omega_l$. Let the resistance R_δ against the rotation be given with the signal function $C_\delta = \mathrm{sgn}\left(\dot{\delta}\right)$. Here a rotation in a counterclockwise direction is defined as a positive value.

The coordinate transform matrix $\mathbf{T}$ from the absolute coordinates $\Sigma\{X, Y, \delta\}$ to the rover coordinates $\Sigma\{X_m, Y_m, \delta\}$ can be expressed by

$$\mathbf{T} = \begin{bmatrix} \cos\delta & -\sin\delta & 0 \\ \sin\delta & \cos\delta & 0 \\ 0 & 0 & 1 \end{bmatrix}. \tag{3.5}$$

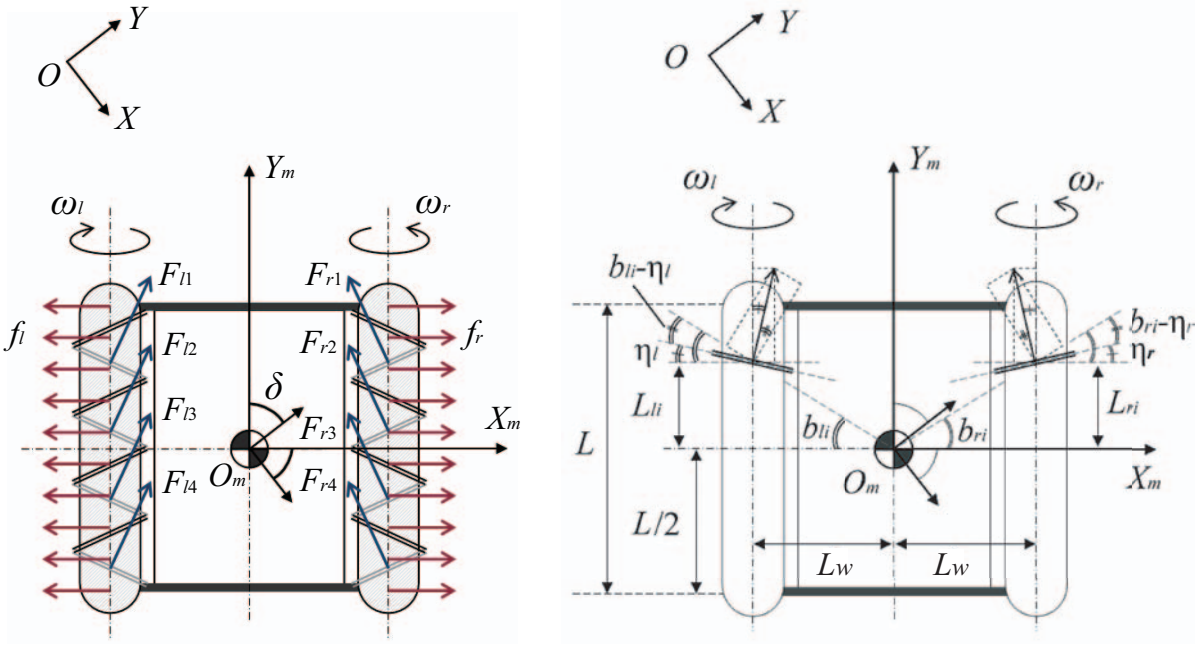

Figure 3.7 : Simplified dynamics model of Screw Drive Rover.

Accordingly, these equations enable the simulation of the dynamic motion behavior of the Screw Drive Rover system. The variation of the motion trajectories is demonstrably not dependent on the right-and-left arrangement of the screw units due to the symmetrical motion trajectory about a terrain surface.

The propulsive forces generated on the screw are affected by the screw driving modes. So, coefficients k_1 and k_2 are newly defined as the following equations. In addition to these, DC motors are also assumed for driving the screws and then the amplitude of the acting force is also defined by ω_j (where $j = r, l$) as follows.

$$\begin{cases} F_r &= \dfrac{F_{r0}|\omega_r|}{2\pi} \\ k_1 &= \left|\dfrac{\omega_l}{\omega_r}\right| = \dfrac{F_l}{F_r} = \dfrac{f_l}{f_r} \\ k_2 &= \dfrac{f_r}{F_r} = \dfrac{f_l}{F_l} \end{cases} \tag{3.6}$$

where no difference is assumed between the screws. Furthermore, the resistance factor F_{r0} is set to be $F_{r0} = \hat{\mu} m_r g/2$ (where $\hat{\mu}$ is a friction coefficient between the screw unit and the soil, and g is a gravitational acceleration).

3.4.2 Simulation Analysis based on Skin Friction Model

Through computational simulations, the dynamic characteristics of the developed model are analyzed. As nominal constant parameters, the simulation analyses set: $\hat{\mu} = 0.2$, $m_r = 5\,\mathrm{kg}$, $g = 9.8\,\mathrm{m/s^2}$, $I_r = 0.1\,\mathrm{kgm^2}$, $\eta = 30\,\mathrm{deg}$, $L = 0.25\,\mathrm{m}$, $L_W = 0.15\,\mathrm{m}$, $k_2 = 1$, $R_X = 2\,\mathrm{N}$, $R_Y = 4\,\mathrm{N}$ and $R_\delta = 14\,\mathrm{N}$. The operative acceleration factors $\left(\ddot{X}_m, \ddot{Y}_m, \ddot{\delta}\right)$ in Eqs. (3.2) $\sim$ (3.4) can have values when they indicate larger than each resistance, but otherwise they become zero.

At first, the motion trajectories are discussed. In the simulations, the velocity $\left(\dot{X}, \dot{Y}, \dot{\delta}\right)$ and the position with the attitude (X, Y, δ) are given by a step time $dt = 0.2\,\mathrm{s}$. Additionally, the variable angular velocities (where, the units are radian per second) are set as shown in Table 3.3. Figure 3.8 shows the simulated results when the starting position is set to be the origin in X-Y coordinate. Here the rover is illustrated as a pentagonal shape in Figure 3.8 to obtain the rover's

Table 3.3 : Simulation conditions for motion trajectories.

	Case 1	Case 2	Case 3	Case 4	Case 5	Case 6	Case 7	Case 8
ω_r [rad/s]	$\pi/2$	$-\pi/2$	$\pi/2$	$-\pi/2$	2π	2π	π	π
ω_l [rad/s]	$-\pi/2$	$\pi/2$	$\pi/2$	$-\pi/2$	π	$-\pi$	2π	-2π

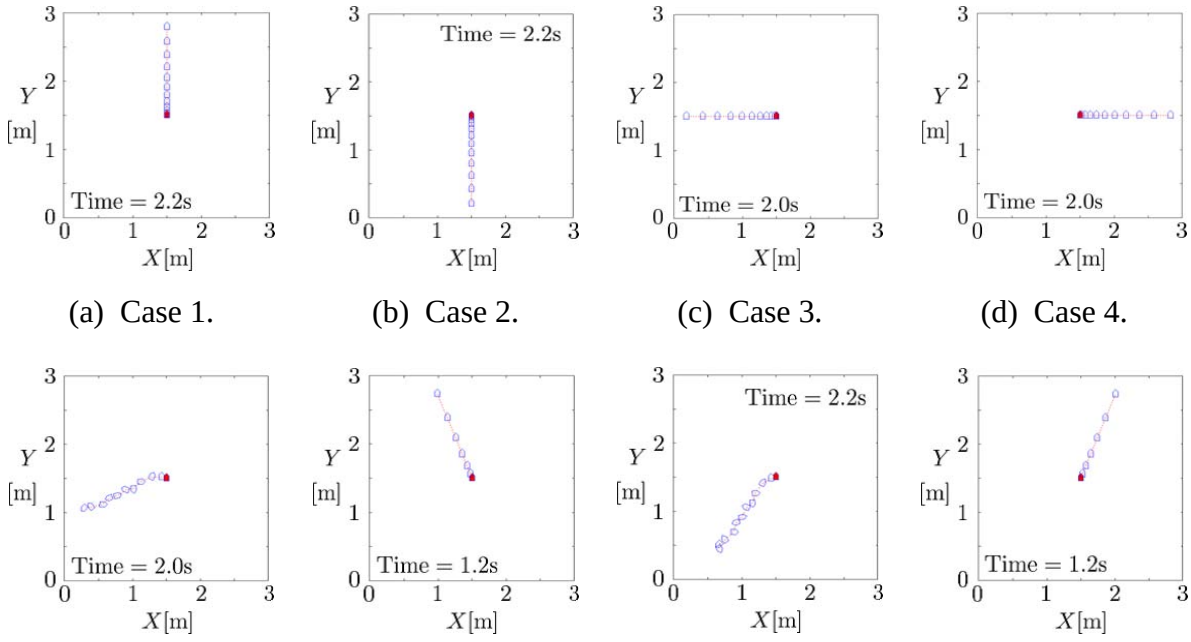

(a) Case 1. (b) Case 2. (c) Case 3. (d) Case 4.

(e) Case 5. (f) Case 6. (g) Case 7. (h) Case 8.

Figure 3.8 : Simulation results: Dynamic trajectories of the Screw Drive Rover model.

direction. From these results, it is confirmed that the modeled rover can demonstrate diverse motion trajectories. This denotes the complicacy and the diversity of the rover's motion.

Secondly, Figure 3.9 depicts the distributions of the conditions and the moving accelerations $\left(\ddot{X}, \ddot{Y}, \ddot{\delta}\right)$ under the above nominal parameters and $\eta = 60\,\mathrm{deg}$. Here the motion direction is assumed to be same with the acceleration direction for representing R_X, R_Y and R_δ. According to these graphs, the Screw Drive Rover can generate propulsive forces omnidirectionaly. Meanwhile, the body rotation correlates with the proportion of the acceleration in Y direction. This would be caused by the resistances R_X, R_Y and R_δ, and it is important to note that these simulations assume $R_X < R_Y$. Furthermore, the simulations are conducted under $R_X = R_Y = R_\delta = 0$ for

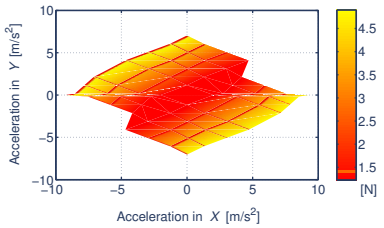

(a) F_r with resistances.

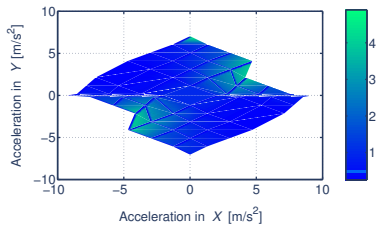

(b) k_1 with resistances.

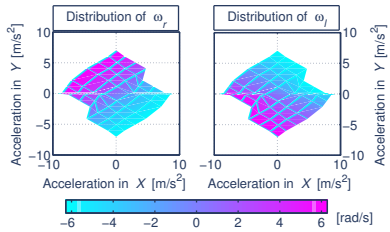

(c) ω_r and ω_l with resistances.

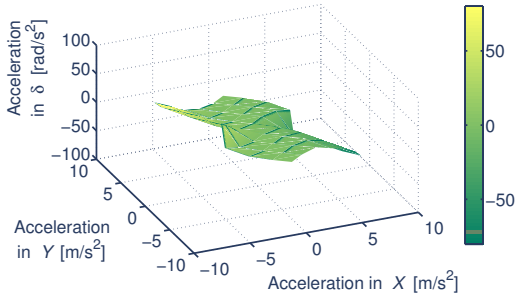

(d) 3D plots of accelerations with resistances.

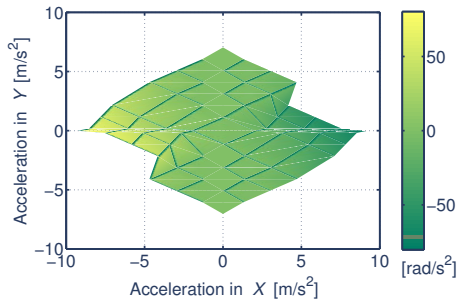

(e) 2D plots of accelerations with resistances.

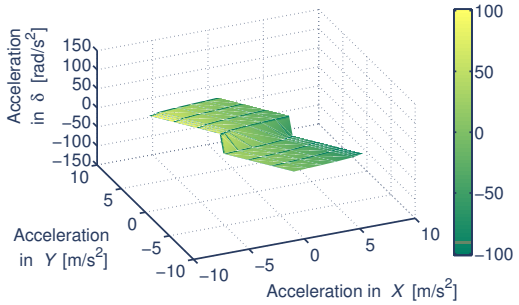

(f) 3D plots of accelerations without resistances.

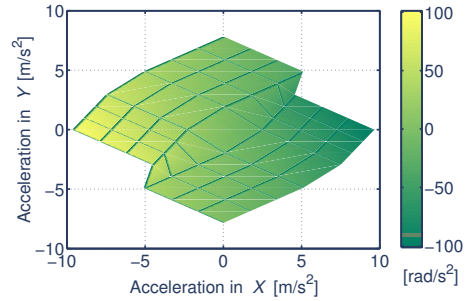

(g) 2D plots of accelerations without resistances.

Figure 3.9 : Simulated distribution of parameters and generated accelerations with $\eta = 30\,\mathrm{deg}$.

comparing investigation as plotted in Figures 3.9(f) and 3.9(g). These plots indicate emphasis to the balance of the propulsive forces and the resistances.

Thirdly, the additional simulations are examined by various η and k_2 as shown in Figures 3.10 and 3.11. In accordance with these graphs, it is easy for the rover to move right-and-left than back-and-forth with the proportion of η. The directional mobility of the Screw Drive Rover correlates with its screw geometry η. It is confirmed that k_2 does not have a much influence on the proposed model. For improving the proposed system, these discussions can lead to notable guidelines on its proper mechanical design.

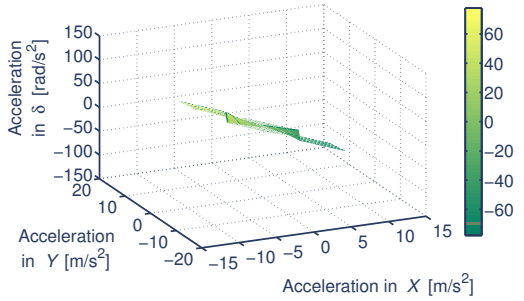

(a) 3D plots at $\eta = 15$ deg.

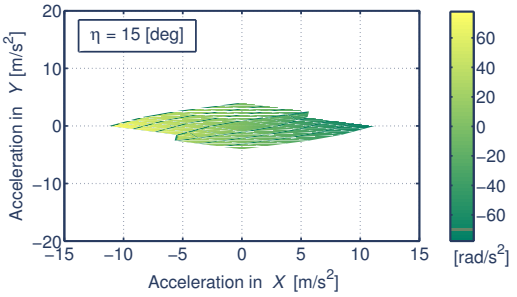

(b) 2D plots at $\eta = 15$ deg.

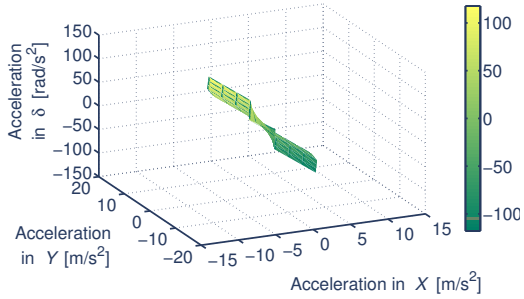

(c) 3D plots at $\eta = 45$ deg.

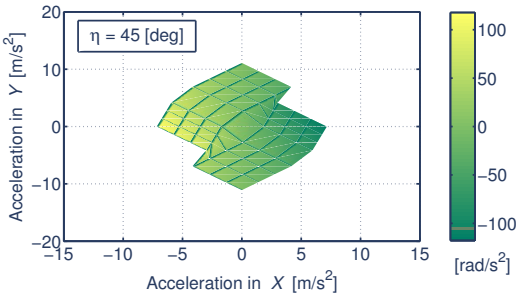

(d) 2D plots at $\eta = 45$ deg.

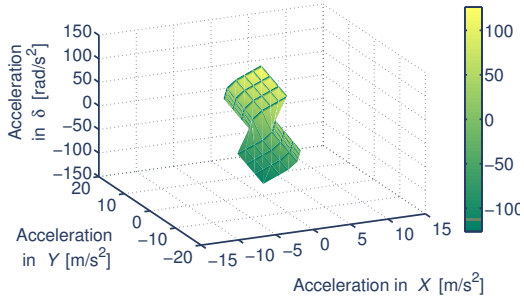

(e) 3D plots at $\eta = 75$ deg.

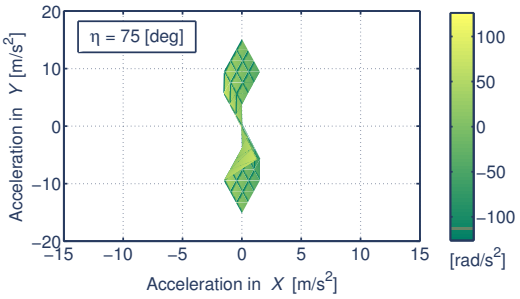

(f) 2D plots at $\eta = 75$ deg.

Figure 3.10 : Simulated distribution of accelerations without frictional resistances: various η.

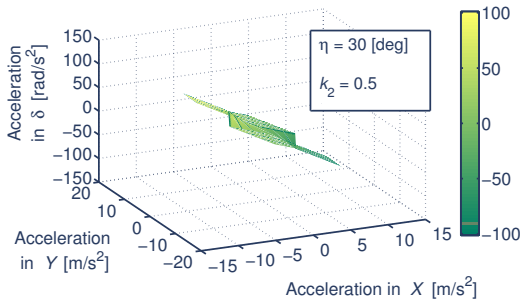

(a) 3D data at $k_2 = 0.5$.

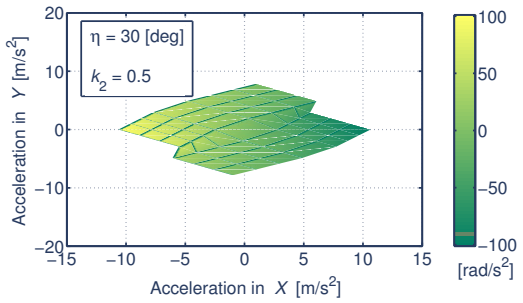

(b) 2D data at $k_2 = 0.5$.

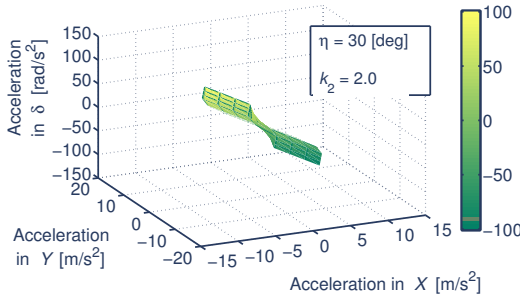

(c) 3D data at $k_2 = 2$.

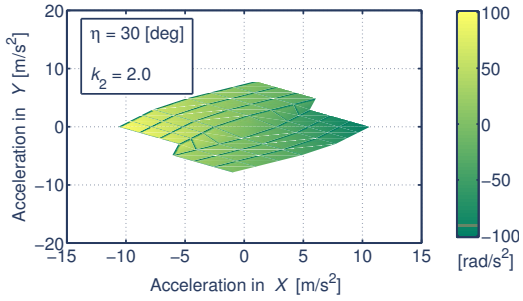

(d) 2D data at $k_2 = 2$.

Figure 3.11 : Simulated distribution of accelerations without frictional resistances: $\eta = 30$ deg and various k_2.

3.4.3 Terramechanics Model

In the terramechanic discipline, there have been mainly three approaches to discuss traveling performances of land vehicles. The first approach is an analytical approach based on numerical analyses such as FEM (Finite Element Method) [101] or DEM (Discrete Element Method) [103]. The DEM analysis can simulate discrete behavior of soil particles but it generally requires much computational cost, and thus the number of simulated elements is quite limited. So, these days a combined analysis of FEM and DEM has been implemented by Nakashima *et al.* [91]. On the other hand, both FEM and DEM need a process of trial and error in order to determine their model parameters. Although these analytic approaches are of benefit in preliminary surveys, it cannot be expanded to locomotion control of the rovers. The second one is an empirical approach based on empirical equations and/or the cone index [98]. In general, the empirical approach has been consistent with practical applications and its formulae enable to predict vehicle's mobility performances. Meanwhile, the formulae have been developed as empirical equations and they are thus influenced by specific characteristics of vehicles and terrains. The third one is a

semi-empirical approach [66, 73, 75, 82, 83]. Although this approach includes several empirical parameters, it can reflect soil characteristics (soil compaction and shear) based on soil mechanics. This dissertation discusses the soil-screw interaction model based on the semi-empirical models as the terramechanics model.

Screw Geometric and Kinematic Definitions

The motion states of the Screw Drive Rover are preliminarily defined. Absolute coordinates $\Sigma_O\{X,Y,Z\}$ is set as illustrated in Figure 3.12. The modeling assumes a family of soil-screw moving together as one body. Further to this, the screw model technically depends on its winding direction but subsequent definitions and formulas can be essentially regarded as common expressions.f Therefore, unified expressions are described for each screw unit unless stated otherwise.

First, the screw pitch p was already defined in the Chapter 4 by using the slope angle η. In addition to these, the screw flight's surface area dA at micro region $d\theta$ can be applied based on Eq. (2.6). It is assumed that the locomotion is basically governed by forces on dA. Furthermore, this research employs slip in x axis, s_x, which is defined in Eq. (2.8) as follows [43]. s_x can be expressed as follows.

$$s_x = \begin{cases} \dfrac{pf - v_x}{pf} & \text{if } |pf| \geq |v_x| \quad : 0 \leq s_x \leq 1 \\ \dfrac{pf - v_x}{v_x} & \text{otherwise} \qquad\quad : -1 \leq s_x \leq 0 \end{cases} \tag{3.7}$$

where f is the screw rotation speed and $f = \omega/2\pi$ (ω is the screw angular velocity).

In addition, a direction of locomotion is introduced. Given a velocity vector v_O in Σ_S, the angle between v_O and the x axis is defined as slip angle α [76]. Here α is expressed as follows.

$$\alpha = \arctan\left(\frac{v_y}{v_x}\right) \tag{3.8}$$

where v_x and v_y is the x and the y component of the velocity v_O in Σ_S, respectively. Likewise, v_x and v_y can be also written by

$$v_x = pf(1-s_x), \quad v_y = pf(1-s_x)\tan\alpha. \tag{3.9}$$

Mathematical Formulations of Contact Stresses

The relationship between soil normal stress and locomotion gear's sinkage is one of the significant subjects in terramechanics. Note that the traditional terramechanics equations discussed

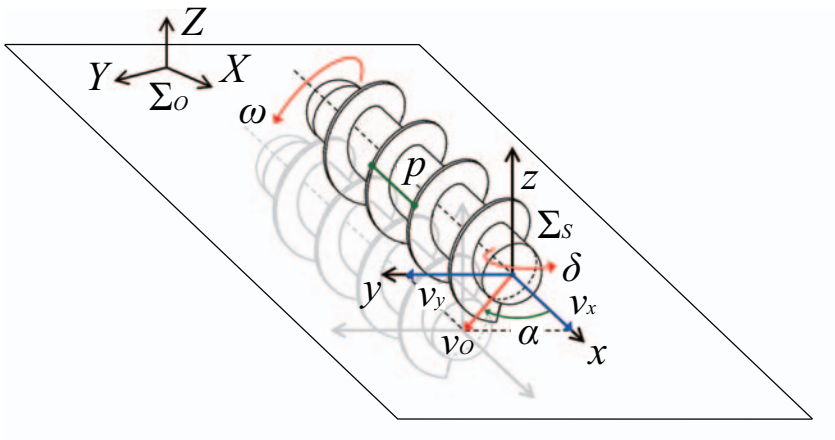

Figure 3.12 : Kinematics model of the screw unit.

below are semi-empirical models based on reacted soil behavior. The normal stress distribution of soil beneath a rolling circular object, such as a rigid wheel or the screw unit, is defined by [66, 70, 82]

$$\sigma(\theta_s) = \begin{cases} \sigma_m \left(\cos\theta_s - \cos\theta_{sf}\right)^n & \text{if} \quad \theta_{sm} \le \theta_s \le \theta_{sf} \\ \sigma_m \left\{\cos\left[\theta_{sf} - \dfrac{\theta_s - \theta'_{sr}}{\theta_{sm} - \theta'_{sr}}\left(\theta_{sf} - \theta_{sm}\right)\right] - \cos\theta_{sf}\right\}^n & \text{otherwise} \end{cases} \tag{3.10}$$

and also,

$$\sigma_m = \left(\frac{k_c}{L} + k_\phi\right) R_E^n \tag{3.11}$$

where θ_s is the screw winding angle along soil shearing ($\theta'_{sr} \le \theta_s \le \theta_{sf}$), θ'_{sr} (≤ 0) is the effective exit angle, θ_{sf} (≥ 0) is the entry angle, θ_{sm} is the specific wheel angle at which the maximized normal stress occurs, L is the screw's longitudinal length, n is sinkage exponent, and k_c and k_ϕ are pressure-sinkage moduli regarding soil cohesion and soil internal friction angle, respectively. Let R_E be the elliptic distance as illustrated in Figure 3.13, and will be defined later on. In addition, relational angle expressions can be given by the following equations [71, 82].

$$\theta_{sf} = \arccos\left(1 - \frac{h}{R_0}\right) \tag{3.12}$$

$$\theta_{sm} = \left(c_1 + c_2 s_x\right)\theta_{sf} \tag{3.13}$$

where c_1 and c_2 are coefficients depending on the soil-screw interaction.

The conventional studies in terramechanics are basically premised on $|\theta_{sr}| \le |\theta_{sf}|$ for the expression of σ beneath a rigid wheel. In the case of the screw unit, however, $|\theta_{sf}| \le |\theta_{sr}|$ has been observed through the traveling tests. This implies the reaction force from discharging soil

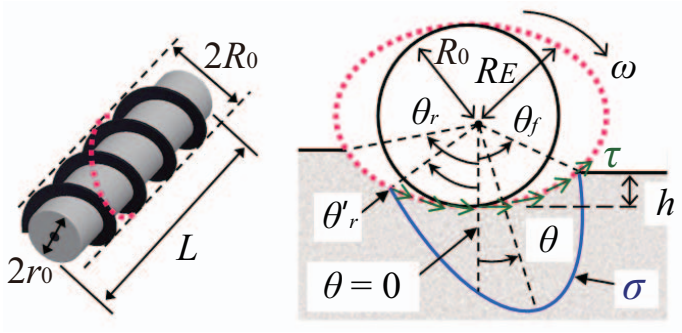

Figure 3.13 : Soil-screw interaction model.

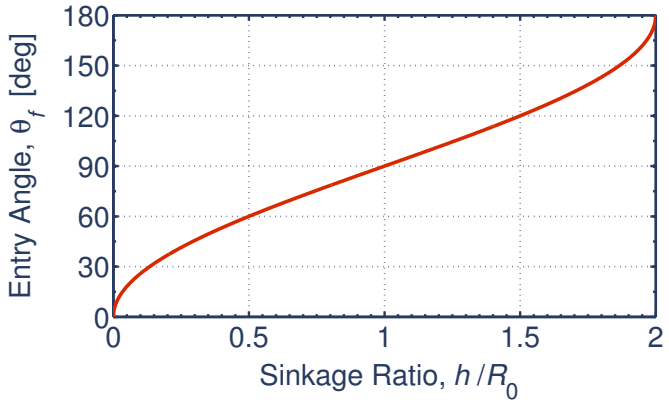

Figure 3.14 : Relationship between θ_{sf} and h/R_0.

is too small, and therefore, the stress distribution satisfying $|\theta_{sf}| \leq |\theta_{sr}|$ is obtained. Therefore, $|\theta_{sf}| \leq |\theta_{sr}|$ is assumed by means of a transformation of θ_{sr} to θ'_{sr}. θ'_{sr} achieving $|\theta'_{sr}| \leq |\theta_{sf}|$ is given as follows.

$$\theta'_{sr} = -c_3 \theta_{sf} \tag{3.14}$$

where c_3 (≤ 1) is a positive angle coefficient.

The screw unit provides an elliptic cross section for discussing the normal and the shear stresses with angle θ_s as illustrated in Figure 3.13. In wheels, while the soil is sheared in elliptic trajectory when a wheeled vehicle steers, the common formula of the normal stress is applicable [76]. Hence, this research also employs the unified normal stress distribution Eq. (3.10).

The shear stress τ of soft soil is formulated as follows [67, 68].

$$\tau(\theta_s) = \tau_{\max} \left[1 - \exp\left(-j/K\right)\right] \tag{3.15}$$

$$\text{where} \quad \tau_{\max}(\theta_s) = C + \sigma \tan\phi \tag{3.16}$$

here $\tau_{\max}$ is soil shear strength, ϕ is soil internal friction angle, C is soil cohesion stress, j is soil displacement and K is a soil shear deformation modulus.

Shear Displacement of Soil

Unlike the traditional approaches, this dissertation takes into account three-dimensional soil transportation. In general, the soil between the screw flight is regarded as one body with the screw flight. From this point of view, it can be assumed that the soil shear stress occurs along the outermost radius of the screw flight. Consequently, the expression of the screw's helical trajectory is needed to model the soil thrust. The screw motion trajectory in Σ_O, $\mathcal{T}(X,\, Y,\, Z)$, is first provided by the following expression.

$$\mathcal{T} = \begin{bmatrix} R_0 \cos\theta_s \sin\delta + v_X t + X_0 \\ R_0 \cos\theta_s \cos\delta + v_Y t + Y_0 \\ R_0 \sin\theta_s + Z_0 \end{bmatrix}^T \tag{3.17}$$

where,

$$\begin{cases} v_X = v_x \cos\delta + v_y \sin\delta \\ v_Y = -v_x \sin\delta + v_y \cos\delta \end{cases} \tag{3.18}$$

Then, the trajectory of the soil shearing is defined by the angle γ_E $(= \pi/2 - \eta)$ as illustrated in Figure 3.15. This trajectory $\mathcal{P}_E\,(X_E,\, Y_E,\, Z_E)$ basically traces an ellipse. In the screw fixed elliptic coordinates $\Sigma_E\{X_E, Y_E, Z_E\}$, $\mathcal{P}_E$ can be derived as follows.

$$\mathcal{P}_E = \begin{bmatrix} \dfrac{R_0}{\cos\gamma_E}\cos\beta_E \\ R_0 \sin\beta_E \\ 0 \end{bmatrix}^T = \begin{bmatrix} \dfrac{-R_0}{\cos\gamma_E}\sin\theta_s \\ R_0 \cos\theta_s \\ 0 \end{bmatrix}^T \tag{3.19}$$

where β_E is equal to $\theta_s + 3\pi/2$.

The tangential equation at a certain point $(x_a, -y_a)$ on $\mathcal{P}_E$ is also represented as follows.

$$\frac{x_a}{r^2 \sec^2\gamma_E} \cdot X_E + \frac{y_a}{r^2} \cdot Y_E = 1 \tag{3.20}$$

where x_a and y_a are positive values, and the sinkage is assumed to be less than R_0. Substituting Eq. (3.19) into (3.20), the above equation can be eventually simplified as follows.

$$y_a = -\frac{\cos\gamma_E}{\tan\beta_E} \cdot x_a + \frac{r\cos\gamma_E}{\sin\beta_E} \tag{3.21}$$

Accordingly, the inclination angle ξ of the tangent is written as follows.

$$\xi = \arctan\left(-\cos\gamma_E \cot\beta_E\right) = \arctan\left(\cos\gamma_E \tan\theta_s\right) \tag{3.22}$$

Furthermore, the ellipse radius R_E is formulated as a function of θ_s by

$$R_E\,(\theta_s) = r\,\sqrt{\cos^2\theta_s + \sin^2\theta_s \sec^2\gamma_E}. \tag{3.23}$$

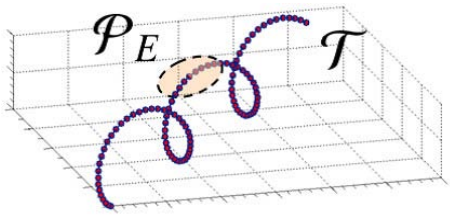

(a) Trajectories of screw flight and soil displacement.

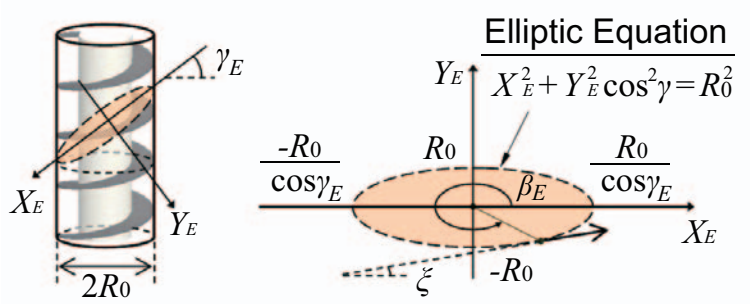

(b) Soil shearing ellipse.

Figure 3.15 : Elliptic trajectory of soil shearing.

Thus, j can be ultimately defined as follows.

$$j(\theta_s) = \oint_{\mathcal{L}} v_j \, dt \tag{3.24}$$

and also,

$$\mathcal{L} = \mathcal{T} + \mathcal{P}_O \tag{3.25}$$

$$\mathcal{P}_O = \begin{bmatrix} -R_0 \sin\theta_s \sin(\delta + \gamma_E) \\ -R_0 \sin\theta_s \cos(\delta + \gamma_E) \\ -R_0 \sec\gamma_E \cos\theta_s \end{bmatrix}^T \tag{3.26}$$

where $\mathcal{L}$ is the trajectory of the displaced soil in Σ_O and v_j is the relative soil displacement velocity along $\mathcal{L}$. Moreover, $\mathcal{P}_O$ gives a transformation from $\mathcal{P}_E$, transforming their coordinates $\Sigma_E \rightarrow \Sigma_O$. In light of Eq. (3.9), the time derivative of $\mathcal{L}$ is given as follows.

$$\begin{aligned} \frac{d}{dt}\mathcal{L} &= \frac{d}{dt}(\mathcal{T} + \mathcal{P}_O) \\ &= \begin{bmatrix} \dfrac{(1-s_x)\,p}{2\pi} - R_0 \cos\theta_s \sin\gamma_E \\ \dfrac{(1-s_x)\,p}{2\pi}\tan\alpha - R_0(\sin\theta_s + \cos\theta_s \cos\gamma_E) \\ R_0 \cos\theta_s + \dfrac{R_0}{\cos\gamma_E}\sin\theta_s \end{bmatrix}^T \cdot \omega \\ &= \begin{bmatrix} \mathcal{L}_{v_{jx}} & \mathcal{L}_{v_{jy}} & \mathcal{L}_{v_{jz}} \end{bmatrix} \cdot \omega \end{aligned} \tag{3.27}$$

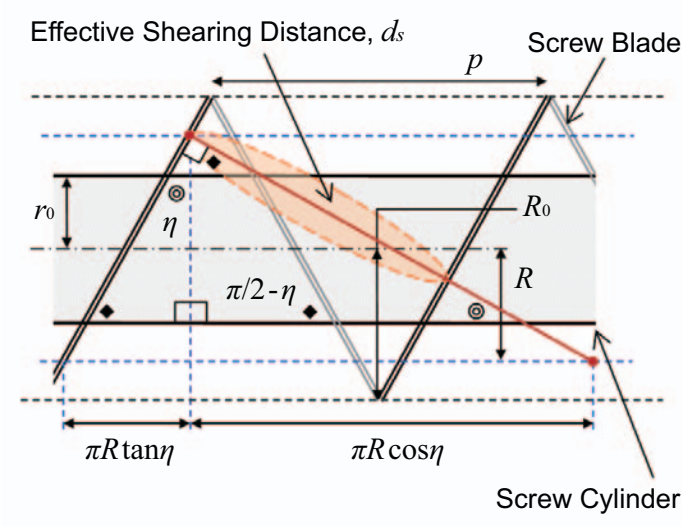

(a) Illustration of effective shearing distance.

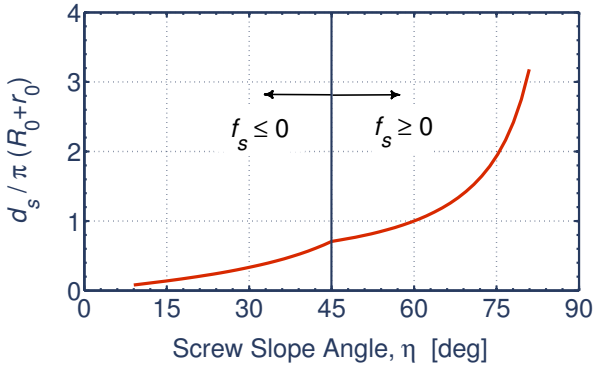

(b) Parametric analysis of d_s depending on η.

Figure 3.16 : Effective distance of soil shearing.

where δ and $\dot{\delta}$ are assumed to be zero.

Therefore, Eq. (3.24) can be finally expressed by

$$j(\theta_s) = \oint_{\mathcal{L}} v_j \cdot dt = \int_{\theta_s}^{\theta_{sf}} \sqrt{\mathcal{L}^2_{v_{jx}} + \mathcal{L}^2_{v_{jy}} + \mathcal{L}^2_{v_{jz}}} \cdot d\theta_s. \tag{3.28}$$

Stationary State of Dynamic Sinkage

Yamakawa *et al.* [92] has investigated the dynamic sinkage of a wheel, and concluded that the sinkage reaches a stationary state under constant slip. Referring to the literatures [79,97,99], the slip-sinkage characteristics analogous to this remark have been also reported with experimental results. On the basis of these literatures, it is estimated that the stationary sinkage is proportional

to the slip. The proportionality factor depends on both the wheel and the soil. Hence, this dissertation assumes the simplified relationship as follows.

$$h = h_0 + c_4 s_x \tag{3.29}$$

where h_0 is static sinkage with no-slip ($s_x = 0$), c_4 is a positive coefficient. This enables as to simulate the relativity of the slip and the sinkage.

Effective Factor of Soil Shearing Distance

The effective distance of the soil shearing, d_s, is geometrically constrained by η and p as illustrated in Figure 3.16(a). To evaluate the distance, the effective factor f_s is given as follows.

$$f_s = \frac{p}{r_0} - \frac{\pi (R_0 + r_0)(\tan\eta + \cot\eta)}{2r_0} \tag{3.30}$$

Thus, d_s is maximized with the positive f_s. Contrary to this, when f_s is negative, d_s is confined to the inter-screw area. The positive f_s obviously appears at $45\,\text{deg} \leq \eta \leq 90\,\text{deg}$. Consequently, d_s can be introduced as follows.

$$d_s = \begin{cases} \dfrac{\pi (R_0 + r_0)\tan\eta}{2\sin\eta} & \text{if} \quad f_s \geq 0 \\ \dfrac{\pi (R_0 + r_0)\tan\eta}{2\cos\eta} & \text{otherwise} \end{cases} \tag{3.31}$$

Figure 3.16(b) depicts the characteristics of d_s pertaining to η. In accordance with this, d_s is strongly governed by η.

Motion Resistance

Forehead motion resistance on the anterior portion of the screw units is a significant factor for the locomotion model. As illustrated in Figure 3.17, the resistance B_X militates against the anterior portion and is called the bulldozing resistance [100]. Assuming the ideal bulldozing line acting on the hemispherical surface [83] as shown in Figure 3.17, B_X is introduced as follows [100].

$$B_X = \frac{1}{2}\gamma_E h_B^2 \frac{\cot X_C - \tan\beta}{\cot(X_C + \phi) - \tan\beta} + c h_B \left[\frac{\tan(X_C + \phi) + \cot X_C}{1 - \tan\beta\tan(X_C + \phi)}\right] \tag{3.32}$$

where,

$$\begin{cases} h_B &= h - (R_0 - r_0) & : \text{Bulldozing Depth} \\ \beta &= \sec\left(\sqrt{\dfrac{h_B}{2r_0}}\right) & : \text{Ideal Bulldozing Angle} \\ X_C &= \dfrac{\pi - \phi}{2} & : \text{Critical Rapture Angle} \end{cases}$$

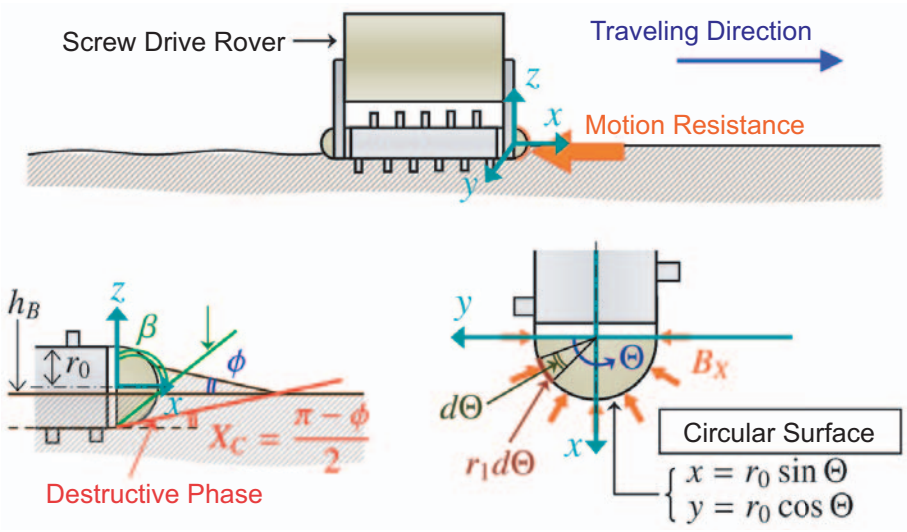

Figure 3.17 : Motion resistance by bulldozing soil.

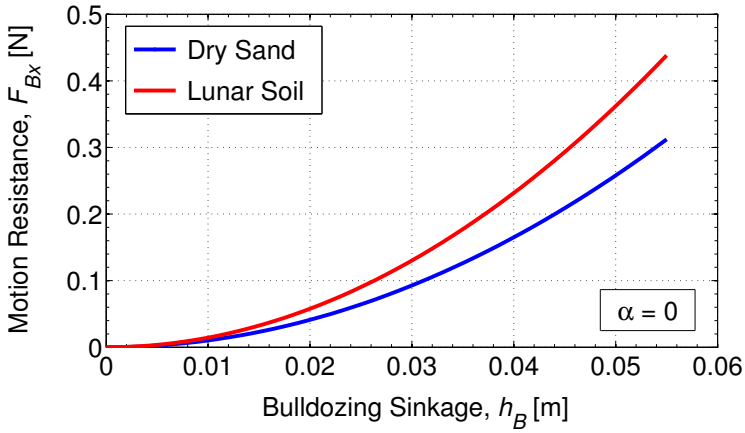

Figure 3.18 : Simulation plots of F_{Bx} and h_B.

whence x and y components of B_X, are given as the integral of B_X by

$$\begin{cases} F_{Bx} &= \int r_0 B_X \sin\Theta \cdot d\Theta \\ F_{By} &= \int r_0 B_X \cos\Theta \cdot d\Theta \end{cases} \tag{3.33}$$

where Θ is angle around the hemispherical portion (see Figure 3.17) and its integral interval is defined by the motion direction α.

Figure 3.18 depicts the relationship between F_{Bx} and h_B with dry sand [82] and the lunar soil [81].

Integrated Locomotion Model

In accordance with the developed model, this section introduces the drawbar pull or the drawbar pull as a synthetic model. The integrated drawbar pull in x direction of the Screw Drive Rover is defined as F_x and is calculated as follows.

$$F_x = \sum \mathrm{sgn}(\omega) F \cos\eta - F_{Bx} \tag{3.34}$$

$$\text{where } F = \iint (\tau\cos\xi - \sigma\sin\xi)\, dA\, d\theta_s \tag{3.35}$$

here $\sum$ denotes the summation of the dual screw units and dA corresponds to ΔA_{sc}. Let the integral region be determined based on d_s. Here because the drawbar pulls are evaluated by whole integration, Eq. (3.35) can be modified as follows.

$$F = b \cdot R_E \sin\eta \int_{\theta'_{sr}}^{\theta_{sf}} (\tau\cos\xi - \sigma\sin\xi)\, d\theta_s \tag{3.36}$$

Likewise, the drawbar pull in y direction, F_y, is computed by

$$F_y = \sum \mathrm{sgn}(\omega) F \sin\eta - F_{By} \tag{3.37}$$

where the body rotation δ is assumed to be ignored in primary analysis, giving $\delta = \dot{\delta} = 0$.

In the proposed model, τ acts as $\tau\cos\xi$ and σ as $-\sigma\sin\xi$ for drawbar pulls in x direction. On the contrary, τ acts as $\tau\cos\theta_s$ and σ as $-\sigma\sin\theta_s$ for a circular wheel. The active angle components of the stresses (*i.e.* $\cos\xi$, $-\sin\xi$, $\cos\theta_s$ and $-\sin\theta_s$) for the drawbar pull are plotted in Figure 3.19. These results indicate $\cos\xi > \cos\theta_s$ and $-\sin\xi < -\sin\theta_s$, and therefore, it is confirmed that the elliptic surface works better than the circular one under equivalent σ and τ. In particular, the elliptic surface has an advantage over the circular one with smaller η. While a steep η provides a much better traction in the forward direction, it leads to deaden the lateral mobility. Consequently, the screw unit needs to take into account a trade-off analysis for practical applications as with the wheel.

3.4.4 Simulation Analysis based on Terramechanics Model

Through the simulations, the drawbar pull F_x is calculated when Screw Driver Rover travels in a straight line. This provides $\delta = \alpha = 0$ as kinematic constraints. By reference to the experiments by Dugoff *et al.* [43], s_x is similarly set to be a variable parameter. With respect to the kinematic and geometric conditions, the nominal parameters are set as shown in Table 3.4. Likewise, according to the experimental data targeting the sampled lunar soil [81] and the previous works [84], each soil parameter is set as shown in Table 3.4. Figure 3.20 plots the simulation

results performed by the proposed model. These results show the predicted drawbar pull F_x with the slip s_x. According to these, it was confirmed F_x increases with an increase in s_x in most situations. This typical tendency was observed in the past experiments [43], and therefore, this confirms the validity of the model. Figure 3.20(a) shows the effect of the screw slope angle η on F_x. The characteristic curves of the drawbar pull and the slip undergoes a significant variation with change of η. As a result, it is concluded that smaller η works to exert the drawbar pull. Figure 3.20(b) shows the tendency that an increase of the exit angle θ'_{sr} introduces larger F_x. Although this indicates an increase of contact surface is significant, c_3 is unlikely to have a significant impact on F_x, compared to η. Moreover, Figure 3.20(c) depicts the tendency that the sinkage h exerts an effect on F_x. Better understanding of the dynamic sinkage is needed in the future work. On the whole, the ratio of the sinkage and the radius h/r becomes a key factor from Figure 3.20. An appropriate control of h/r is the most important technique for the enhancement of tractive performance of the Screw Drive Rover on the soft soil. So that the rover always generates positive drawbar pulls, the design of η also becomes another important factor.

Figure 3.21 shows a comparative analysis of the Screw Drive Rover model with a wheeled and a tracked vehicle model under a constant sinkage $h = 0.03\,\mathrm{m}$. Comparative vehicle models driven by wheels and tracks are shown in Appendix C. The wheeled and the tracked vehicles

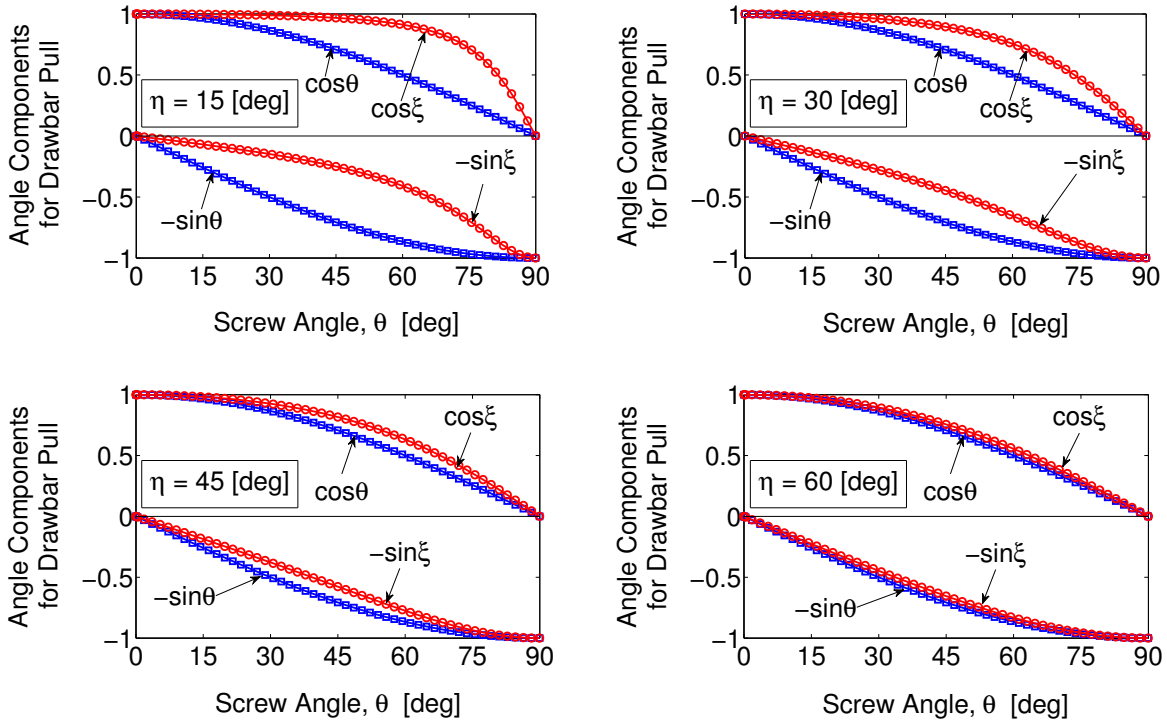

Figure 3.19 : Angle components of stresses for drawbar pull on circular and elliptic surfaces along angles.

Table 3.4 : Simulation parameters for prediction of drawbar pull.

Screw's Geometric Parameter	Symbol	Value	Unit
Screw Slope Angle	η	5, 16, 30	deg
Radius of Screw Cylinder	r_0	0.035	m
Radius of Screw Flight Edge	R_0	0.05	m
Steady Sinkage with Slip	h	0.01∼0.04	m
Steady Sinkage without Slip	h_0	0.01	m
Lunar Soil Parameter [81, 84]	**Symbol**	**Value**	**Unit**
Internal Friction Angle	ϕ	35	deg
Cohesion Stress	C	170	Pa
Pressure-Sinkage Modulus for Internal Friction Angle	k_ϕ	814.4	kN/m^{n+2}
Pressure-Sinkage Modulus for Cohesion Stress	k_c	1379	N/m^{n+1}
Deformation Modulus	K	0.018	m
Pressure-Sinkage Ratio	n	1.0	-
Coefficient for determining the Relative Position of Maximum Radial Stress	c_1	0.4	-
Coefficient for determining the Relative Position of Maximum Radial Stress	c_2	0.15	-
Angle Coefficient of θ'_{sr}	c_3	0.2, 0.5, 0.8	-
Coefficient of Slip Sinkage	c_4	0.01, 0.02, 0.03	-

were modeled so that the vehicles possess equitable contact surface areas in total. According to Figure 3.21, the Screw Drive Rover system has an advantage over the wheeled vehicle. In particular, the wheeled vehicle exerts negative drawbar pull at any slips in this result. This is just the tractive limitations (detailed in Appendix C), and then this indicated the wheeled vehicle is stuck. In contrast, although the track has the mechanical complexity (*e.g.*, many structural components and soil clogging), the tracked vehicle provided better tractive performance than the proposed rover system. Finally, it can be concluded that the proposed system can exert enough traction in the soft soil despite its structural simplicity, and the proposed system will become a possible solution for future rovers traveling over the soft terrain.

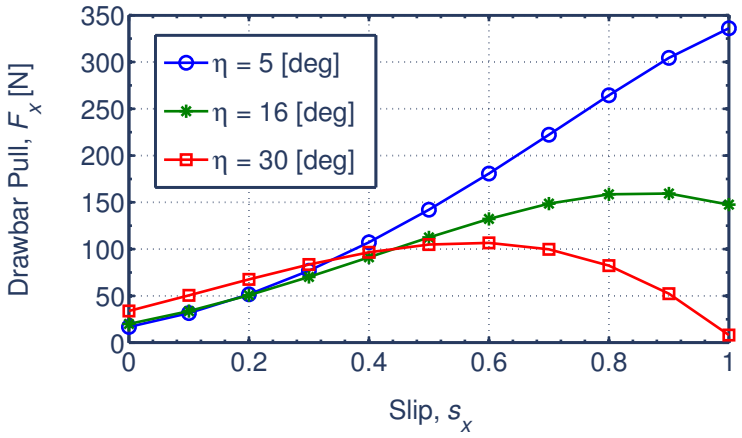

(a) With varying η, $c_3 = 0.2$ and $c_4 = 0.03$.

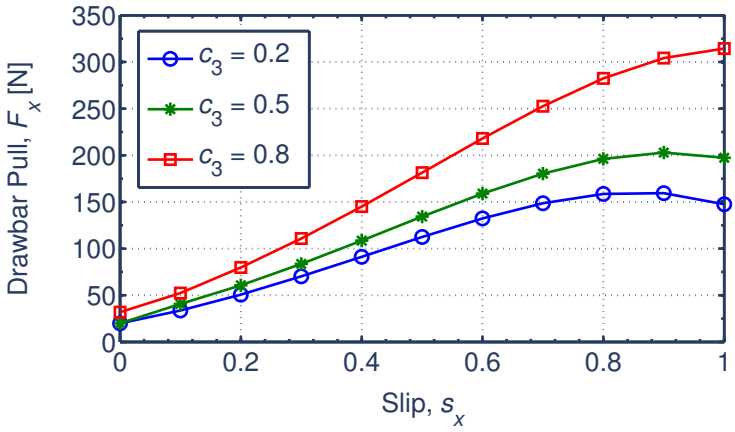

(b) With varying c_3, $c_4 = 0.03$ and $\eta = 16\,\text{deg}$.

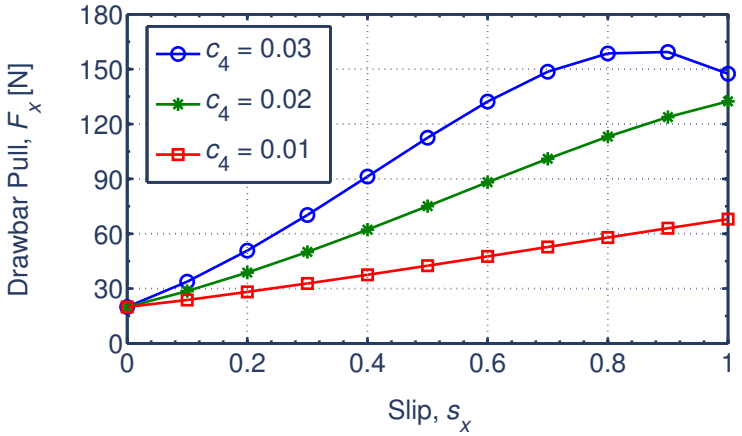

(c) With varying c_4, $c_3 = 0.2$ and $\eta = 16\,\text{deg}$.

Figure 3.20 : Simulated drawbar pull and slip of the Screw Drive Rover model.

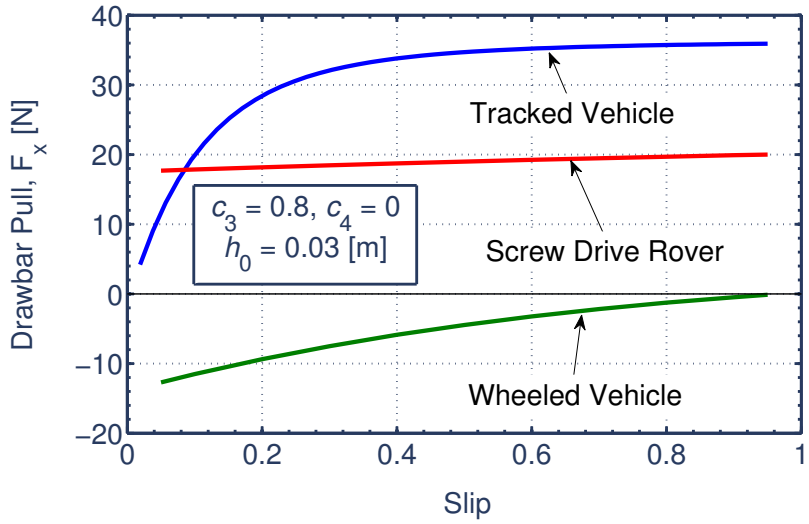

Figure 3.21 : Comparative simulation result of Screw Drive Rover model with wheeled and tracked vehicle models.

3.5 Synthetic Modeling of Soil-Screw Interaction

3.5.1 A Lesson for Synthetic Interaction Model

With considerations of the above discussions, the synthetic interaction model is introduced based on an integrative approach of the skin friction and the soil shear. While the skin friction model can simulate diverse motion trajectories, it cannot represent the characteristics between the drawbar pull and the slip. Thus the skin friction model is defined by just the friction coefficient and the screw geometry. In the meantime, the terramechanics model can represent soil shear but cannot consider the skin friction between the screw unit and the soil. Accordingly, a relative slippage of the screw unit and the soil between the screw flights is ignored in the terramechanics model. That is, the interaction model is defined as though the shape of the screw unit were a circular cylinder. As a result, the screw fights, the soil between screw flights and adjacent soil are modeled as individual motions in these models.

This dissertation attempts to develop a novel soil-screw interaction model by combining the ideas of the skin friction and the terramechanics model. Unlike conventional locomotion dynamics models, the innovative interaction model is able to independently represent the motions of the screw fights, the soil between screw flights and the adjacent soil.

3.5.2 Dynamics Modeling

Figure 3.22 illustrates the diagrams of the soil-screw interaction model. The soil between the screw flights at $\Delta\theta$ is assumed to be a continuum model and is a hexahedral solid. Here the screw thickness is assumed to be neglected. Let two-dimensional coordinates fixed on the screw flight be $\Sigma\{X_S, Y_S\}$, where X_S axis is parallel to the screw flight surface and Y_S axis is perpendicular to X_S axis as illustrated in Figure 3.22(b). As a first step, the EOMs of the soil between the screw flights are derived. The EOMs of the soil contacting with ΔA_{sc} in X_S-Y_S coordinates can be obtained as follows.

$$m_s \ddot{X}_S = D_X - \sum_{i=0}^{3} F_i \cos(\alpha_i - \eta) \tag{3.38}$$

$$m_s \ddot{Y}_S = N - D_Y - \sum_{i=0}^{3} F_i \sin(\alpha_i - \eta) \tag{3.39}$$

and also,

$$\begin{aligned} D_X &= D_1 \cos\eta - D_2 \cos\eta \quad (= D\cos\eta) \\ D_Y &= D_1 \sin\eta - D_2 \sin\eta \quad (= D\sin\eta) \end{aligned} \tag{3.40}$$

where m_s is the mass of the soil between the screw flights, N is the normal force, F_0 is the frictional force of the soil against the upper surface of the screw flight, F_1 is the frictional force of the soil against the lateral surface of the cylindrical part, F_2 is the frictional force of the soil against the lower surface of the screw flight, F_3 is the frictional force of the external adjacent soil around the soil, α_i ($i = 0, 1, 2, 3$) is the acting angle of each force F_i ($i = 0, 1, 2, 3$) as shown in Figure 3.22(b), and $\ddot{X}_S$, $\ddot{Y}_S$ are the second order differentials of X_S, Y_S by a time t, respectively. Furthermore, D_1 and D_2 are the downward and upward forces respectively, then D_X and D_Y intend X_S and Y_S component of D, and D denotes the resultant force given by $D_1 - D_2 (\geq 0)$. Therefore, the derivation of unknown N would be a key factor.

As a kinematic assumption, given the soil moves along the screw flight surface, $\ddot{Y}_S = 0$ can be introduced. Substituting $\ddot{Y}_S = 0$ into Eq. (3.39), N can be simply written as follows.

$$N = D_Y + \sum_{i=0}^{3} F_i \sin(\alpha_i - \eta) \tag{3.41}$$

In addition, the acting force matrix $\mathbf{F}$ is defined as follows.

$$\mathbf{F} = \begin{bmatrix} F_0 \\ F_1 \\ F_2 \\ F_3 \end{bmatrix}^T = \begin{bmatrix} \hat{\mu} N \\ \hat{\mu}\sigma(\theta)\, pr_0 \cdot \Delta\theta \\ \hat{\mu} K_0 \sigma(\theta) \cdot \Delta A_{sc}(\theta) \\ \tau(\theta)\, pR_0 \cdot \Delta\theta \end{bmatrix}^T \tag{3.42}$$

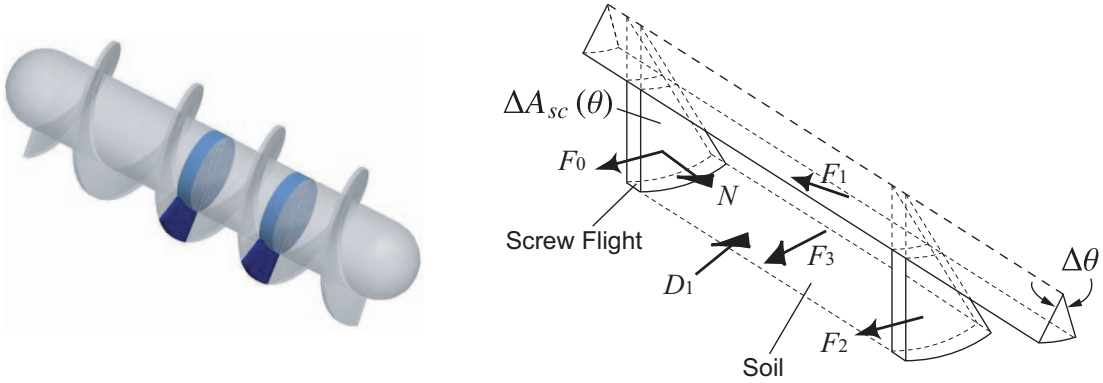

(a) Three-dimensional diagram.

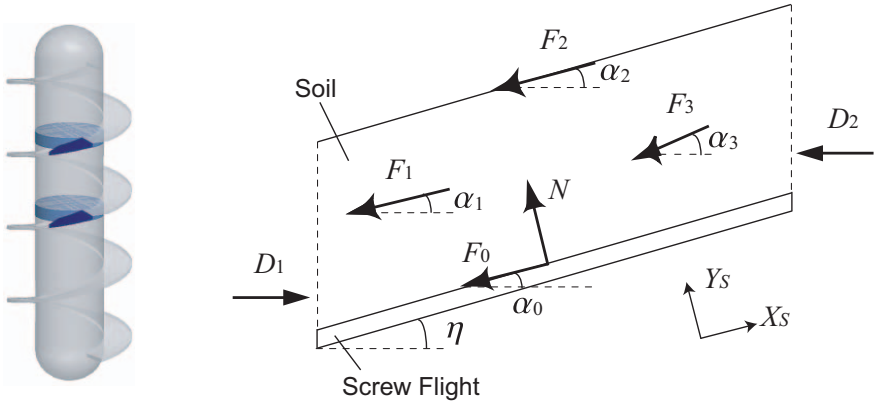

(b) Two-dimensional diagram.

Figure 3.22 : Interactive traveling model of the screw flight and the soil.

where $\sigma(\theta)$ is normal soil stress at angle θ, γ is soil bulk weight, μ is the frictional coefficient between the soil, $\hat{\mu}$ the frictional coefficient between the screw and the soil, α_c and α_s are the half apex angle of the inner cylinder and the ideal cylinder composed by the screw flight respectively (see Figure 2.1). $\sigma(\theta)$ corresponds to $\sigma(\theta_s)$ defined in Eq. (3.10). Additionally, F_3 is essentially the force of the soil shear stress.

Furthermore, α_i $(i = 0,1,2,3)$ is expressed as follows.

$$\begin{aligned} \alpha_0 &= \alpha_1 = \alpha_2 = \eta \\ \alpha_3 &= \arctan\left(\sqrt{\frac{\mathcal{L}_{v_{jx}}^2}{\mathcal{L}_{v_{jy}}^2 + \mathcal{L}_{v_{jz}}^2}}\right) \end{aligned} \tag{3.43}$$

where $\mathcal{L}_{v_{ji}}$ $(i = x,y,z)$ is the velocity component of the soil displacement in Σ_O. The mathematical derivation of $\mathcal{L}_{v_{ji}}$ is re-defined subsequently.

In accordance with the above definitions, by applying Eqs. (3.41) $\sim$ (3.43), unknown force N

can be definitely obtained by

$$N = D\sin\eta + F_3\sin(\alpha_3 - \eta). \tag{3.44}$$

As the next step, the resultant force D is introduced. In this dissertation, the soil is assumed to be transported with a constant speed. Based upon this assumption, $\ddot{X}_S$ becomes zero, and therefore, D can be given by applying Eq. (3.39) as follows.

$$D = \frac{F_0 + F_1 + F_2 + F_3\cos(\alpha_3 - \eta)}{\cos\eta} \tag{3.45}$$

The soil displacement j defined in Eq. (3.28) is applied to calculate τ. But, because the skin friction occurs and the soil moves along the screw flight surface, $\mathcal{L}_{v_{ji}}$ (where $i = x,y,z$) defined in Eq. (3.27) needs to be rewritten as follows.

$$\begin{bmatrix} \mathcal{L}_{v_{jx}} \\ \mathcal{L}_{v_{jy}} \\ \mathcal{L}_{v_{jz}} \end{bmatrix}^T = \begin{bmatrix} \dfrac{s_x p}{2\pi} \\ R_0\cos\theta_s + \dfrac{\tan\alpha}{2\pi} p\,(1 - s_x) \\ R_0\sin\theta_s \end{bmatrix}^T \cdot c_5 \tag{3.46}$$

where c_5 is a soil transportation factor, and body angle δ is also assumed to be zero.

Accordingly, the drawbar pulls in x and y directions are calculated as follows.

$$F_x = \sum \int_{\theta=0}^{\theta=2\bar{N}\pi} \left(N\cos\eta - \sum_{i=0}^{2} F_i\sin\alpha_i \right) - F_{BX} \tag{3.47}$$

$$F_y = \sum \int_{\theta=0}^{\theta=2\bar{N}\pi} \left[\sum_{i=0}^{2} (F_i\cos\alpha_i + N\sin\eta)\cos\theta - r_0 p\sigma\sin\xi \cdot d\theta \right] - F_{BY} \tag{3.48}$$

where the second term on the right-hand side of Eq. (3.48), $r_0 p\sigma\sin\xi\, d\theta$, militates against the rover's locomotion as soil compaction resistance.

Likewise, the total frictional resistance moment M_T exerted by the soil between the screw flights can be calculated as follows.

$$M_T = \int_{\theta=0}^{\theta=2\bar{N}\pi} (\Delta M_N + \Delta M_F) \tag{3.49}$$

and also,

$$\Delta M_N = NR\sin\eta \tag{3.50}$$

$$\Delta M_F = \mathbf{F}\cdot\mathbf{r} \tag{3.51}$$

$$\mathbf{r} = \begin{bmatrix} R\cos\alpha_0 & r_0\cos\alpha_1 & R\cos\alpha_2 & 0 \end{bmatrix}^T \tag{3.52}$$

where $\mathbf{r}$ is the coefficient matrix of $\mathbf{F}$ for converting into torques.

3.5.3 Simulation Analysis

Based upon the proposed synthetic model, parametric analyses are discussed by numerical simulations. Figure 3.23 depicts a simulated characteristic between the drawbar pull and the slip. The simulation conditions were assumed to be the lunar soil shown in Table 3.4. From this result, it is confirmed that the drawbar pull is proportional to the slip under constant sinkage. That is, this means a larger tractive drag provides a larger slip.

Furthermore, Figure 3.23(b) shows the comparative results of the Screw Drive Rover model and a wheeled vehicle under constant contact area. The simulation conditions were selected to simulate a wheel's tractive limitations (see Appendix B). While the wheeled vehicle does not exert positive traction with any slips, the Screw Drive Rover model can exert positive traction. According to this, the Screw Drive Rover has an advantage over the wheeled vehicle in soft soil.

3.6 Summary

This chapter presented the mathematical models of the soil-screw interaction based on the skin friction and terramechanics. These established models are critical elements for representing the actual interaction. On the basis of these ideas, the novel synthetic model was proposed. As the remarkable conclusions of the proposed model, the key remarks are simply summarized as follows:

- To develop the soil-screw interaction model, both skin friction and soil shear phenomena are combined.
- In the proposed model, the behaviors of the screw and the soil between the screw flights are defined as individual motions respectively.
- Compaction and shear characteristic of the soil is also included.
- Relationship between the screw geometry and the tractive performance can be quantitatively evaluated.

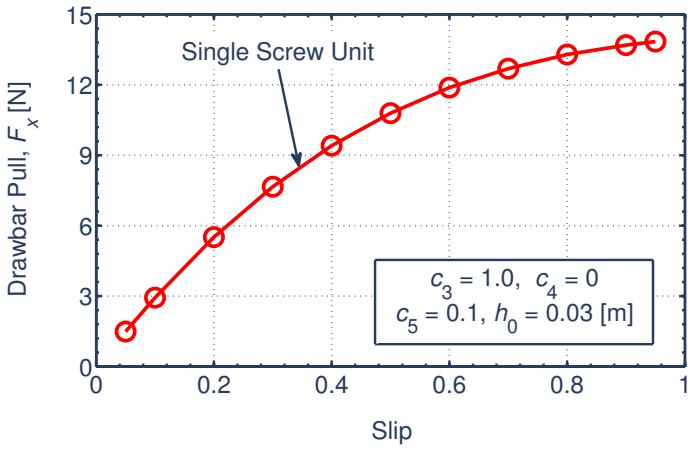

(a) Simulated characteristics of drawbar pull and slip.

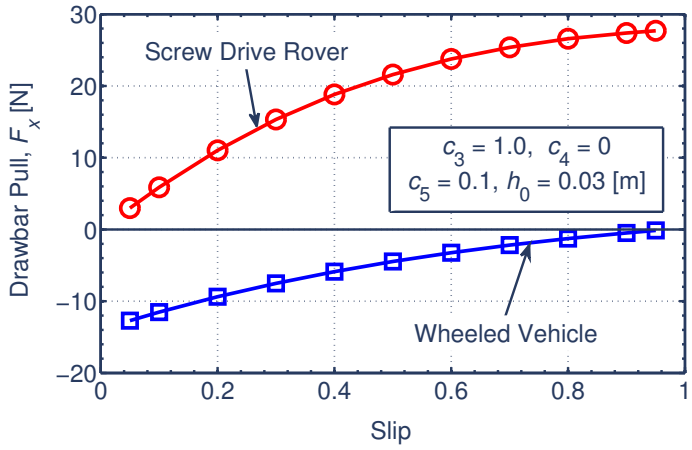

(b) Comparative simulation.

Figure 3.23 : Simulation results of drawbar pull based on synthetic model.

Chapter 4. Experimental Characteristics of Screw Surface Locomotion

4.1 Trafficability Tests of Archimedean Screw Unit

4.1.1 Laboratory Test Environment

Figure 4.1 illustrates the schematic of an experimental system. Load acting on the screw unit can be controlled by load canceler attached at the apex portion of the parallel-link. In general, propulsion behavior of the unit is achieved by only thrust produced in the screw part, and tractive drag is thus applied to the unit through a pulley. Consequently, the tractive characteristics in various slip conditions can be investigated by changes in the tractive drag. The unit rotates through the timing belt connected to a motor, and rotational speed of the unit can be controlled based upon the motor's encoder pulse. A steering motor is also embedded in order to inclined the unit to the traveling direction. In this apparatus, rotational angles and currents of the motors, traveling distance and sinkage can be measured throughout the tests. Considering uncertainty and reproducibility of the tests on sand, several tests should be conducted in each condition. Thus the resulted slip was evaluated as an average value with its error range. Schematic of the screw unit is shown in Figure 4.2.

An overview of the actual experimental apparatus is shown in Figure 4.3. The sand box ($150 \times 20 \times 15$ cm) is filled with quartz sand (no.5) and is same with the soil used in the maneuverability experiments. The sand distributes in narrow range as shown in Figure 4.4, and is thus basically weakly-compressible. Consequently, the quartz sand is regarded as a relatively-reproducible sand for any physical tests.

4.1.2 Evaluation Scheme

Key Indexes

Key evaluation indexes in the traveling tests are first described. As screw geometric parameters, the screw slope angle η and the screw pitch p in Eq. (2.4) are applied. These parameters are

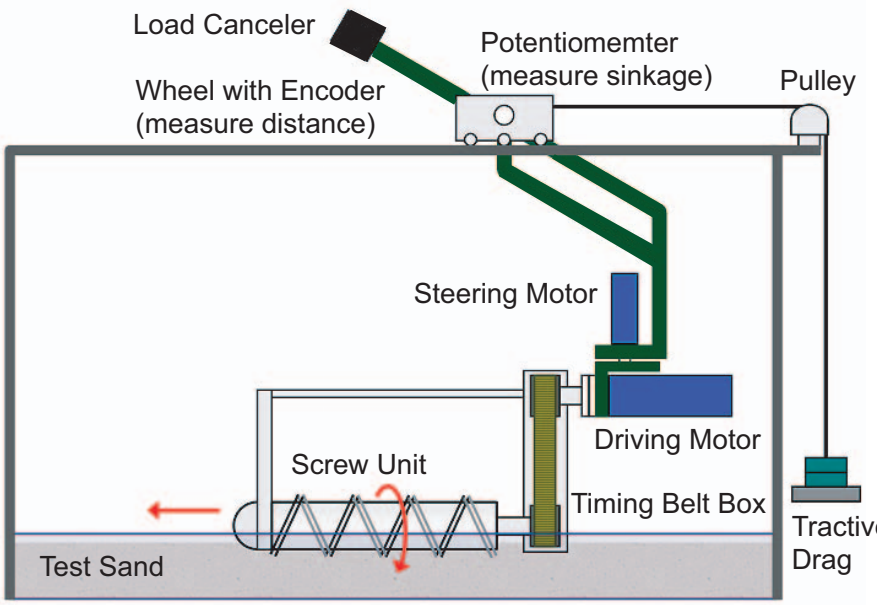

Figure 4.1 : Schematic of laboratory tests.

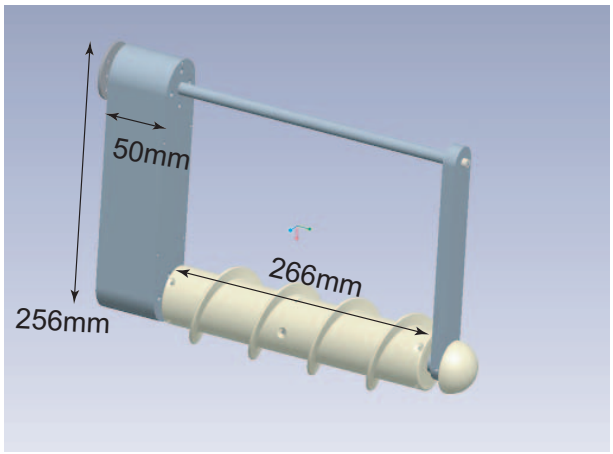

Figure 4.2 : Three-dimensional CAD model of screw unit apparatus.

designed to be constant, and η is particularly represented at half the height of the screw flight.

Generally, mobile robots or vehicles travel over soft terrain with slippage. Absolute coordinates Σ_O (X,Y,Z) is set as illustrated in Figure 4.5. Likewise, the screw fixed coordinates Σ_S (x,y,z) is set to be the right-handed coordinates with x and y axis in the longitudinal and vertical directions of the screw unit. By using screw angular velocity ω, f can be expressed as $f = \omega/2\pi$. During the tests the slip state s_x in Eq. (3.7) was commonly evaluated.

For the Screw Drive Rover system, its traveling direction changes with screw rotational conditions as described in the above section. Here an angle between x direction and the actual traveling direction is defined as slip angle α defined in Eq. (3.8). In the trafficability tests, three

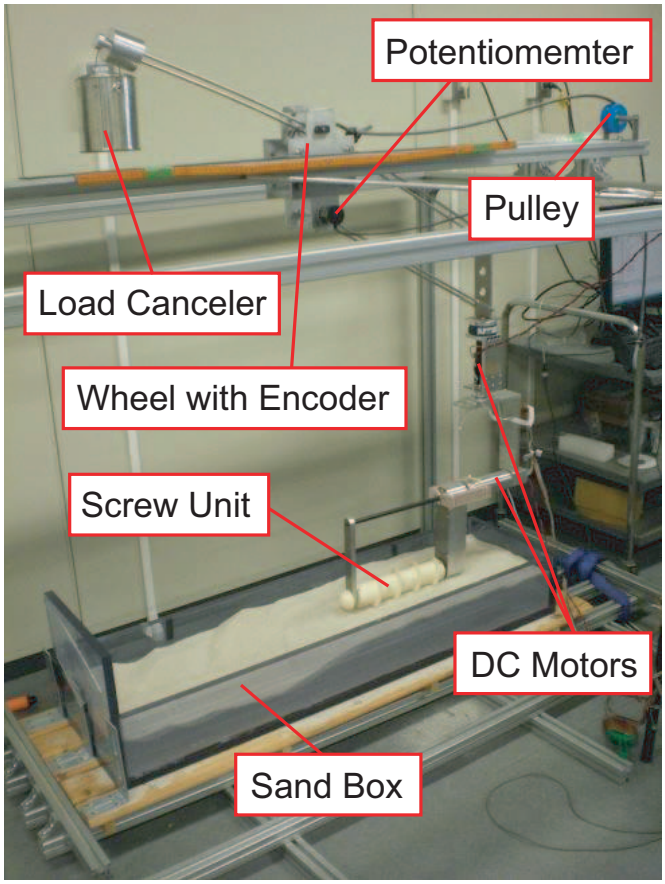

(a) Overview.

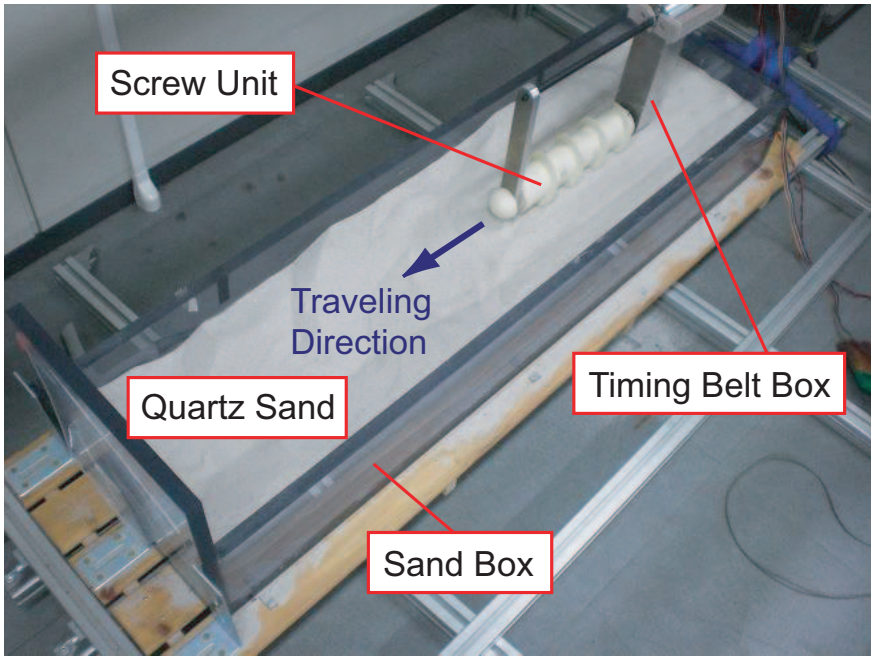

(b) Screw unit on test sand.

Figure 4.3 : Photograph of the experimental apparatus.

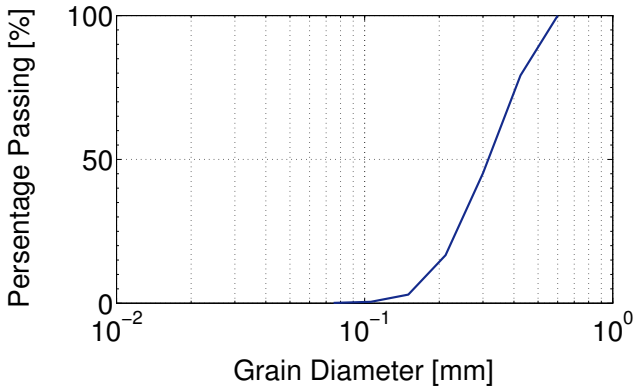

Figure 4.4 : Grain size accumulation curve of quartz sand.

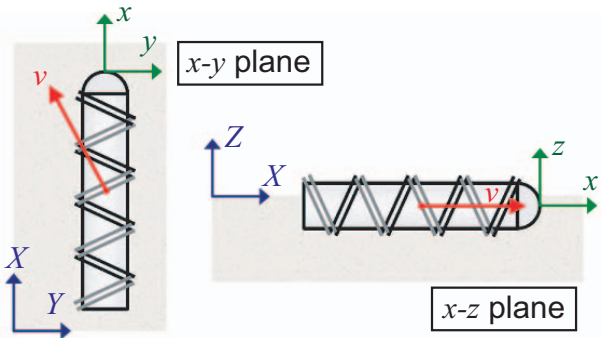

Figure 4.5 : Coordinate of the screw unit.

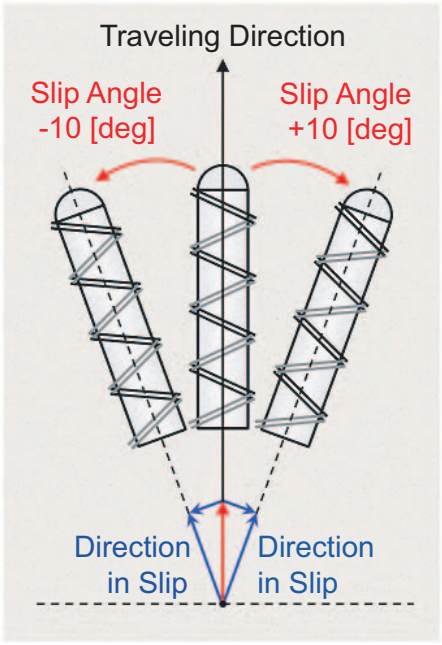

Figure 4.6 : Definition of slip angle.

types of slip angles, -10, 0 and +10 degrees, were applied. Figure 4.6 illustrates the diagram of the change of the slip angle in the tests. Consequently, when the slip angle α is set, the measured traveling distance in X direction must be be transformed to x direction as follows.

$$L_x = L_X \cos\alpha \tag{4.1}$$

where L_x and L_X is the traveling distance in the x and the X direction, respectively. Practically, $\cos(\pm\pi/18)$ is approximately 0.985, and the relative error between L_x and L_X becomes 1.52 percent.

Input

As for experimental inputs to the screw units, a constant screw rotational speed was given in the tests. By controlling the speed, when the traveling speed is constant, the slip s_x indicates also a constant value. Thus the drawbar pull under this constant s_x was experimentally evaluated. As a result, the laboratory tests provided the fundamental characteristics between the drawbar pull and the slip. Here the nominal input of the screw rotational speed was set to be 60 degrees per second, which one revolution every 6 seconds.

Initial Condition

To generate enough thrust for traveling, the screw unit requires larger contact area than a wheel. That is, the screw unit needs more sinkage for its locomotion. Throughout the tests, constant sinkage state was set as a common initial condition. The initial condition was 50 millimeters as illustrated in Figure 4.7. In this tests, the change of the sinkage was negligibly small by comparison with the initial sinkage. Accordingly, the sinkage state was regarded as the constant value, 50 millimeters.

4.1.3 Results and Discussion

Experimental Methodology and Analysis Procedure

Figure 4.8 plots a data example obtained by the test apparatus. Each sensor value was measured and retrieved every 0.1 seconds. The analysis procedure is shown as follows:

1. Set of experimental conditions
2. Set of initial conditions
3. Implementation (driving the screw unit)
4. Calculation of a steady slip

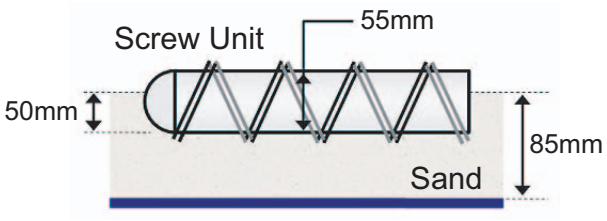

Figure 4.7 : Initial test condition.

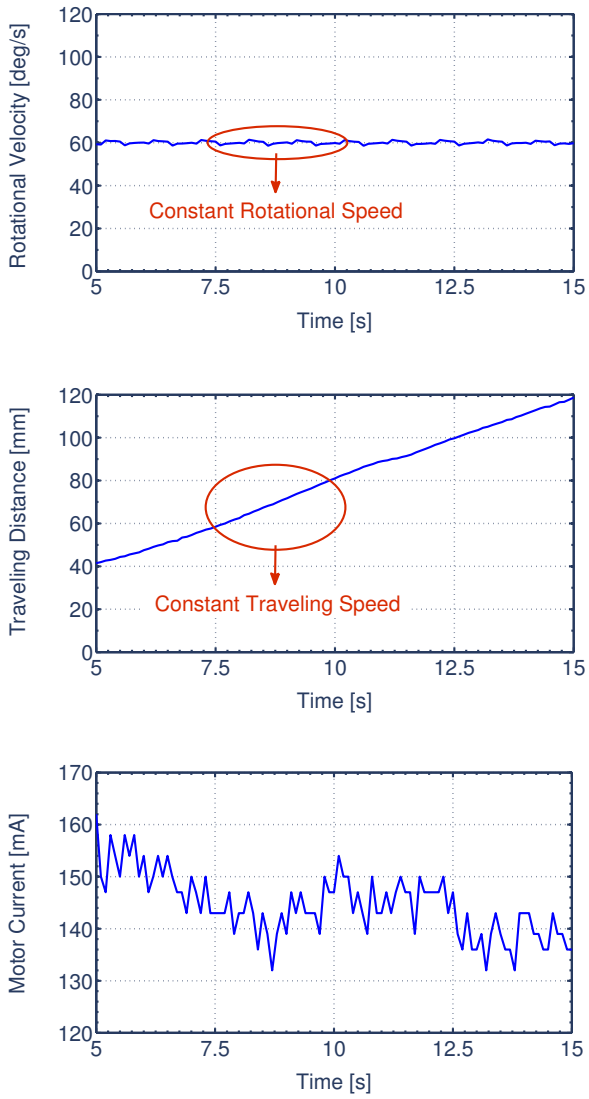

Figure 4.8 : Data example measured by sensors (load is 1.5 kilograms without tractive drag).

As shown in Figure 4.8, the screw rotational velocity and the traveling velocity can be considered as a constant value. Consequently, the evaluation of steady slip states was able to be evaluated. In this research, the relationship between the screw's drawbar pull and the steady slip state was analyzed through the experiments. However, it is important to note that the evaluated drawbar pull includes bulldozing resistance acting on the hemispherical portion in front of the screw flights.

Effect of Load

Experimental characteristics between the drawbar pull and the slip with a change of the screw loads (1.5, 2.0 and 2.5 kilograms) are shown in Figure 4.9. Approximated curves in Figure 4.9

were determined by least squares approximation. Figure 4.9(d) depicts the approximated curves for comparison. In these results, the screw rotational velocity was 60 degrees per second and the slip angle was zero. From this result, it was confirmed that the drawbar pull increases with an increase of the slip, regardless of the screw load. Such tendency actually indicated that the slip increases with an increase of the tractive drag. The resulted tendencies agreed with the past results by Dugoff *et al.* [43]. Also, the tendencies were qualitatively consistent with tractive characteristics of a conventional wheel.

It was indicated that the slip condition became 0.2 in the state without positive drawbar pull. Similar result was already measured in the laboratory tests by the Screw Drive Rover prototype. Thus the resulted $s_x = 0.2$ seems to be an unique value of the prototyped screw unit with respect to its self-propelled state. It is very interesting result that such value was confirmed by both the single and the dual unit tests. Moreover, as total tendencies, the slip state becomes to yield same drawbar pull larger with an increase of the screw load. Considering the error ranges are not narrow, however, the change of the terrain environment affects dominantly on its performance.

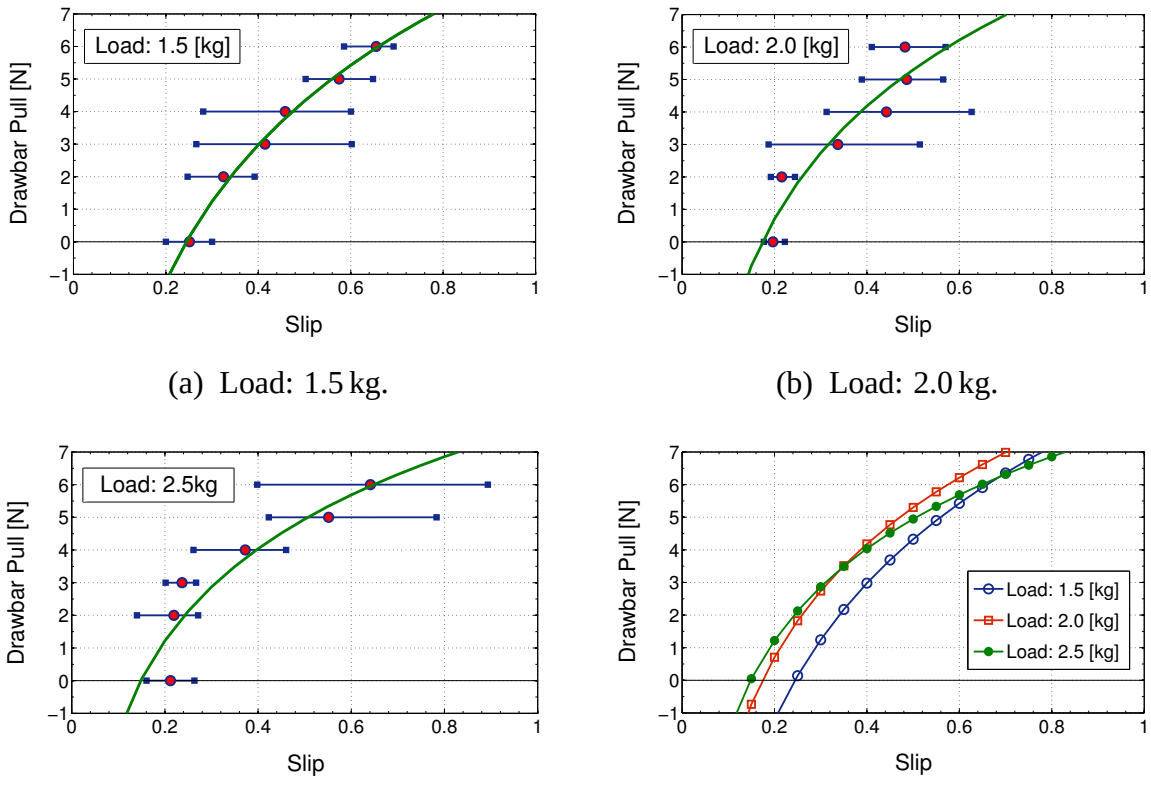

(a) Load: 1.5 kg. (b) Load: 2.0 kg.

(c) Load: 2.5 kg. (d) Approximate lines.

Figure 4.9 : Experimental drawbar pull: Effect of load: 45 deg/s (rotational velocity: 45 deg/s, slip angle: 0 deg).

Effect of Rotational Velocity

Figure 4.10 shows experimental characteristics between the drawbar pull and the slip with a change of the screw rotational velocity (30 and 45 degrees per second). In these tests, the screw load was 2.5 kilograms and the slip angle was zero. Figure 4.10(c) also plots the approximated curves for comparison. From these results, there was no great distinction between the rotational velocities. Moreover, by analyzing the traveling distance, it was confirmed that the traveling velocity was proportional to the rotational velocity. This tendency is same with the Screw Drive Rover prototype (as seen from Figure 4.17). Accordingly, the slip states did not depend on the absolute value of the rotational velocity.

Effect of Slip Angle

Figure 4.11 depicts experimental characteristics between the drawbar pull and the slip with a change of the slip angle ($+10$ and -10 degrees). In these results, the screw load was 2.5 kilograms and the screw rotational velocity was 60 degrees per second. For comparative analysis,

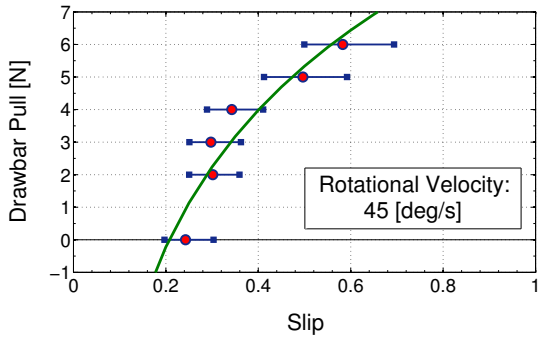

(a) Rotational velocity: 45 deg/s.

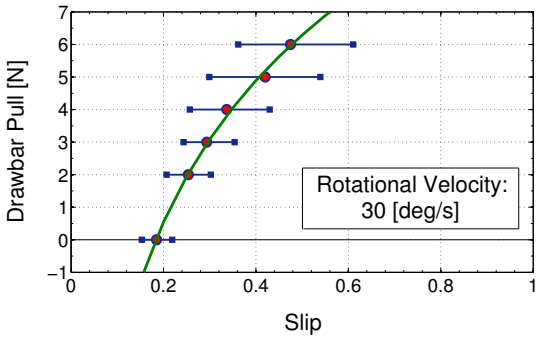

(b) Rotational velocity: 30 deg/s.

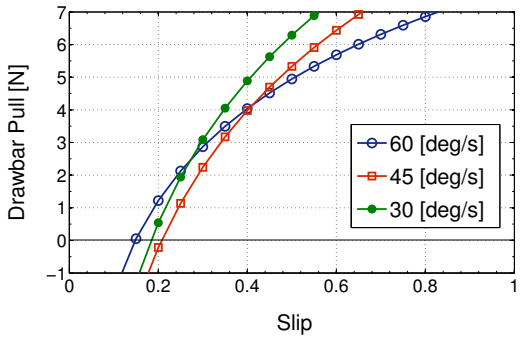

(c) Approximate lines.

Figure 4.10 : Experimental drawbar pull: Effect of rotational velocity (load: 2.5 kg, slip angle: 0 deg).

the approximated curves are shown in Figure 4.11. According to these graphs, it was confirmed that $+10$ degrees of the slip angle can exert better drawbar pull under the steady slips by comparison with 0 and -10 degrees of the slip angle. In contrast, -10 degrees of the slip angle indicated disadvantageous characteristics of the slip and the drawbar pull. In other words, the practical propulsive force of which the screw unit exerts acts in the direction the slip angle becomes positive. Figure 4.12(b) shows normalized drawbar pulls (drawbar pulls over DP at $\alpha = 0$) and their average values were 1.50 ($\alpha = +10$ deg) and 0.64 ($\alpha = -10$ deg). Given a counterclockwise angle component of pure drawbar pull under $\alpha = 0$, $+10$, -10 deg is defined as α_0, α_{+10} and α_{-10}, the normalized drawbar pulls were represented as $\cos(\alpha_{+10})/\cos(\alpha_0 + 10)$ and $\cos(\alpha_{-10} + 20)/\cos(\alpha_0 + 10)$. Detailed definitions of the angles can be found in the presentation slides. According to their results shown in Figures 4.12(c) and 4.12(d), a key relation $\alpha_{+10} > \alpha_0 > \alpha_{-10}$ was estimated.

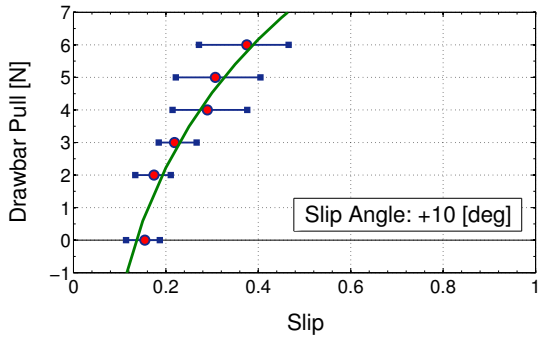

(a) Slip angle: +10 deg.

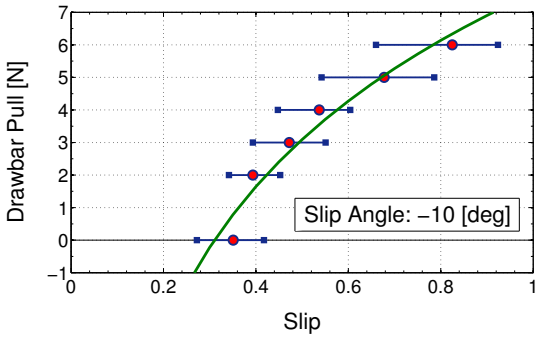

(b) Slip angle: -10 deg.

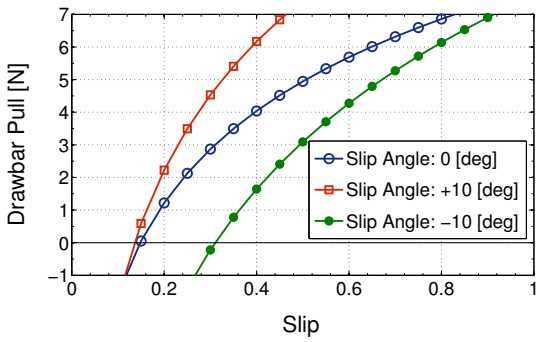

(c) Approximate lines.

Figure 4.11 : Experimental drawbar pull: Effect of slip angle (load: 2.5 kg, rotational velocity: 60 deg/s).

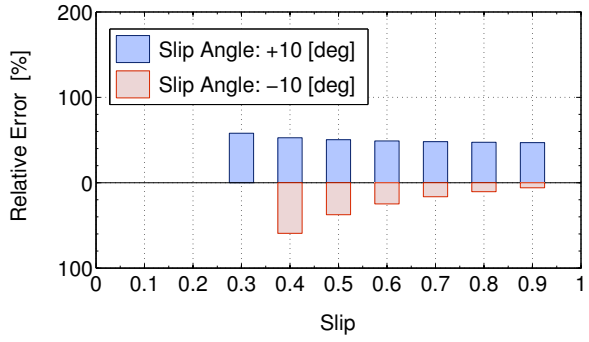

(a) Relative error of drawbar pull.

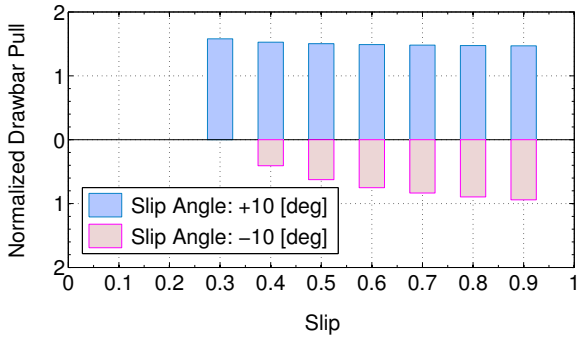

(b) Normalized drawbar pull.

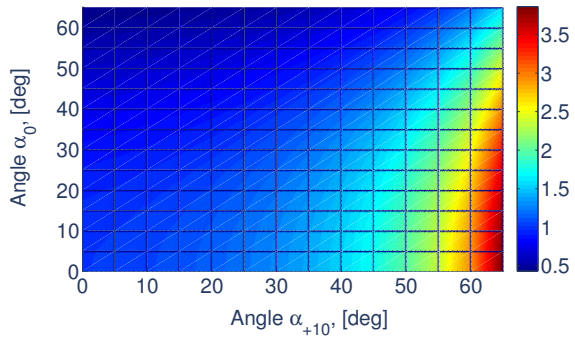

(c) Ratio of $\cos(\alpha_{+10})/\cos(\alpha_0+10)$.

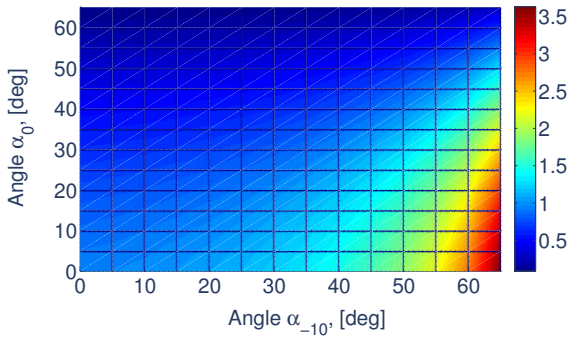

(d) Ratio of $\cos(\alpha_{-10}+20)/\cos(\alpha_0+10)$.

Figure 4.12 : Experimental analysis on drawbar pull with slip: Effect of slip angle.

4.2 Comparative Analysis of Experimental and Theoretical Trafficability

Compared with experimental results, evaluation analyses of the locomotion model proposed in Chapter 3 are discussed. Figures 4.13 and 4.14 show the comparative results. The simulation conditions are shown in Table 4.1. The simulation plots can meet the experimental results, the simulation results are especially in conformity with experimental ones at relatively large slips. Accordingly, these indicated the validity of the model. Furthermore, Figure 4.15 depicts the experimental results and the simulation plots with respect to the effects of the slip angle. The experimental tendencies can be approximately simulated by the proposed model.

From a quantitative standpoint, however, they are slightly different each other. To predict the precise drawbar pull, determination of c_5 will be important, and this suggests that c_5 must be defined as a variable value. Based upon the analyses, c_5 should set to be a larger value at larger slip states.

Table 4.1 : Simulation parameters for prediction of experimental drawbar pull.

Quartz Sand [82, 106]	Symbol	Value	Unit
Internal Friction Angle	ϕ	33	deg
Cohesion Stress	C	0	Pa
Pressure-Sinkage Modulus for Internal Friction Angle	k_ϕ	1523.4	kN/m^{n+2}
Pressure-Sinkage Modulus for Cohesion Stress	k_c	900	N/m^{n+1}
Deformation Modulus	K	0.025	m
Pressure-Sinkage Ratio	n	1.1	-
Coefficient for determining the Relative Position of Maximum Radial Stress	c_1	0.4	-
Coefficient for determining the Relative Position of Maximum Radial Stress	c_2	0.15	-
Angle Coefficient of θ'_{sr}	c_3	1.0	-
Coefficient of Slip Sinkage	c_4	0	-
Transportation Coefficient	c_5	0.016	-

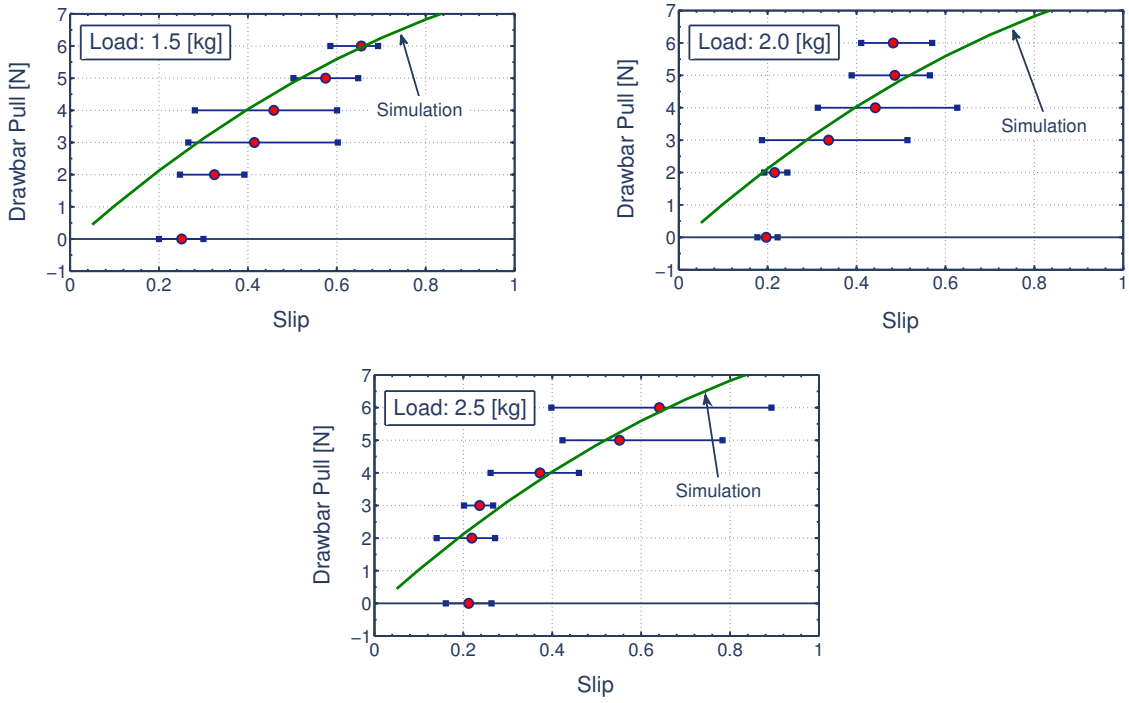

Figure 4.13 : Experimental results and simulations of drawbar pull: Effect of load.

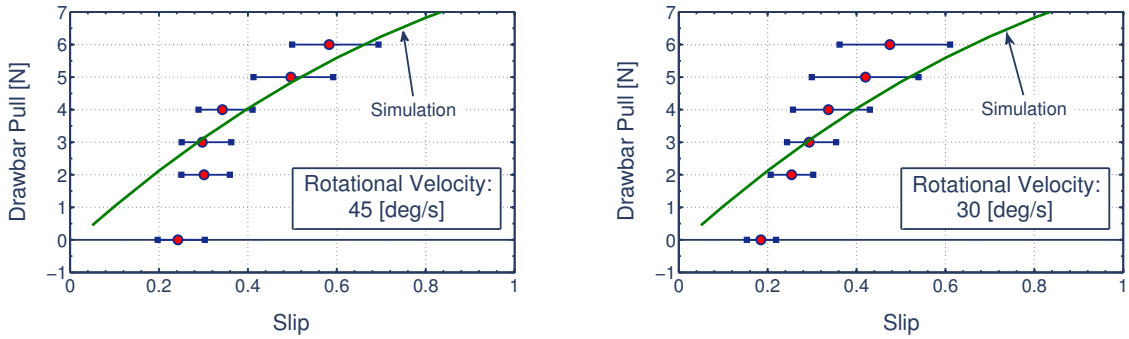

Figure 4.14 : Experimental results and simulations of drawbar pull: Effect of rotational velocity.

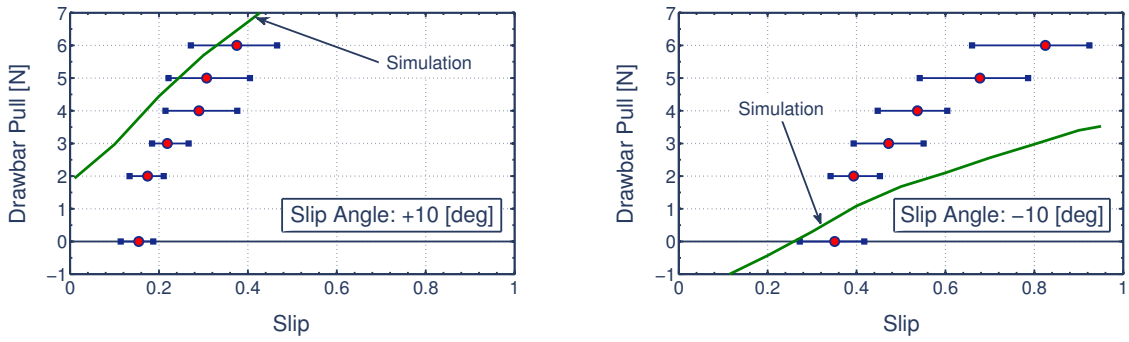

Figure 4.15 : Experimental results and simulations of drawbar pull: Effect of slip angle.

4.3 Empirical Maneuverability of Screw Drive Rover System on Sand

4.3.1 Experimental Setup

The laboratory tests were conducted by using the prototyped Screw Drive Rover to discuss the maneuverability. In the experiments, the test terrain is covered with quartz sand (no.5) and overview of the terrain is shown in Figure 4.16. The grain size distribution of the sand is shown in Figure 4.4. The planer size of the terrain is 3.5×6.5 meters. As driving conditions of the prototype, the angular velocities of the screw units are set to be constant, and the hinge legs are fixed. By varying the input angular velocities, various maneuvering trajectories can be performed. Here seven kinds of inputs (0, ± lower speed, ± middle speed and ± higher speed) are applied. Also, the rotational velocity of the right and left screw units is defined as ω_r and ω_l, respectively. During the tests, the rover's motion is recorded by an external camera, and then the trajectories are obtained by analyzing the recorded videos. Accordingly, the maneuverability can be evaluated by classifying the trajectories.

4.3.2 Fundamental Characteristics of Forward Traveling

Figure 4.17 depicts the experimental characteristics of forward traveling of the prototyped rover. In the forward traveling, the absolute values of the rotational velocities of the screw units were same but the rotational directions were different each another (*i.e.*, $\omega_r = -\omega_l$). From

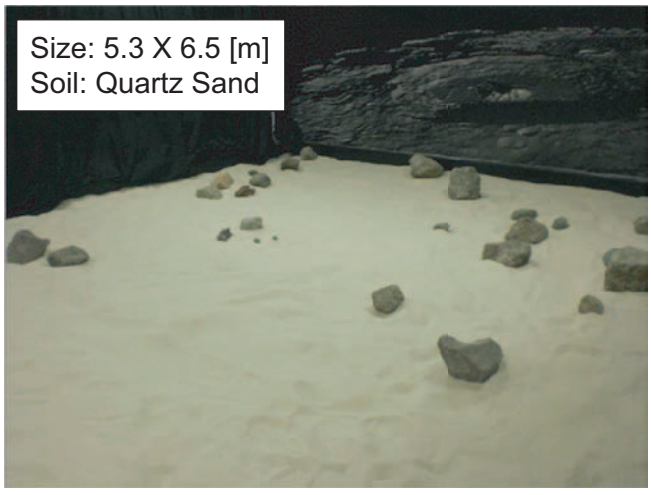

Figure 4.16 : Sandy terrain in laboratory tests.

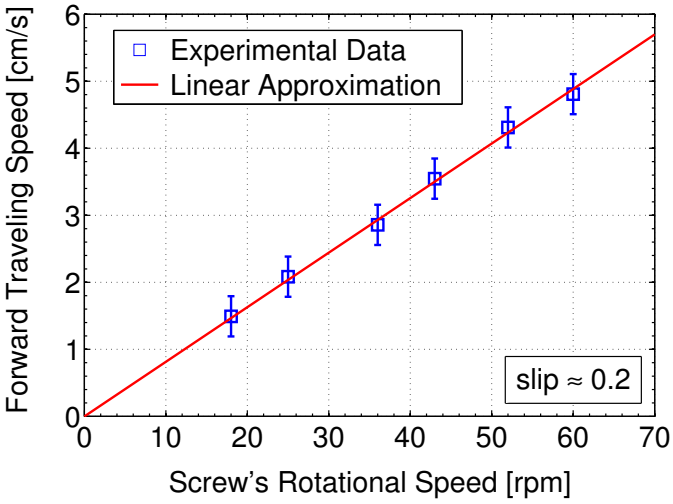

Figure 4.17 : Experimental characteristics of laboratory tests.

Figure 4.17, it was confirmed that the traveling speed was proportional to the rotational speeds. This result also indicated that achieved slip conditions are constant in the forward movement.

4.3.3 Classification of Empirical Maneuvers

Typical maneuvers by the traveling tests are shown in Figures 4.18 and 4.19. In order to evaluate the maneuvering trajectories by videos, the capture images which show the maneuvers are modified as gridded images. From these results, it is confirmed the prototyped rover is able to realize multi-directional locomotion by the two screw units without much slipping and getting stuck into the sand. These results indicate that the screw mechanism is one of the effective locomotion gears on sandy terrain. In addition, undulation of the terrain is also a significant factor for traveling conditions such as the velocity and the trajectory. Natural terrain is generally an undulating surface, and thus an uncertainty of terrain conditions should be taken into account in future research.

As an analysis on the resulted trajectories, the classification of the trajectories can be indicated. Table 4.2 shows the classification. This table is classified by the input rotational speed of the right and the left screw unit. On the basis of the resulted classification, a symmetric property can be confirmed with respect to each speed. The achieved trajectories can be essentially divided in 8 motions: forward movement, backward movement, right turning, left turning, right-front steering, right-rear steering, left-front steering, and left-rear steering. The maneuverability characteristics of the rover can be systematically understood by Table 4.2. Further to these motions, when the screw's rotational speeds are very low, there are some situations that sideways

Figure 4.18 : Various rut formations by the prototyped rover on sand.

movements are also accomplished. But such motions are minor modes, and they might depend on driving torques of the screws and terrain condition (*i.e.*, irregularity or ununiformity).

4.3.4 Maneuverability Analysis

Analysis on Model to Maneuvers

Through the laboratory tests by the Screw Drive Rover prototype, its diverse maneuvers on the sand were confirmed. As the next step, ideal force direction models are attempted to be introduced and analyzed. Here velocity v and body's rotational speed ω_b are simply given as ideal motion to represent the rover's locomotion trajectories. Furthermore, skin friction (SF) model and soil shear (SS) model are assumed to model v and ω_b as illustrated in Figure 4.21(a). The skin friction is defined as a frictional force between the screw flight surfaces and the soil. Also, the soil shear model gives a reactive force in direction normal to the screw flight surface. These models are different each another pertaining to generated force direction on the screw unit. By applying these, ideal v and ω_b can be represented for simulating the trajectories. To demonstrate the rover's trajectories based on the model, a simulator has developed by MATLAB®. A trajectory example of the simulator is shown in Figure 4.21(b).

Compatibility of the ideal models with the empirical maneuvering trajectories was analyzed. From the analyses, the both models match the empirical trajectories regarding forward and backward movements. Meanwhile, in the other conditions, the soil shear model would be statistically suitable. However, the both models simulate the real motions incompletely. From these results, it is indicated that combination of the two models becomes the next challenge to be elaborated. To precisely combine these models, single screw tests are needed for developing an enhanced soil-screw interactive mechanics model. Furthermore, with an uncertainty and an effectiveness of natural terrain, proper application of periodical state feedback to the advanced model is important to realize locomotion control on the Moon, Mars or surfaces of other celestial bodies.

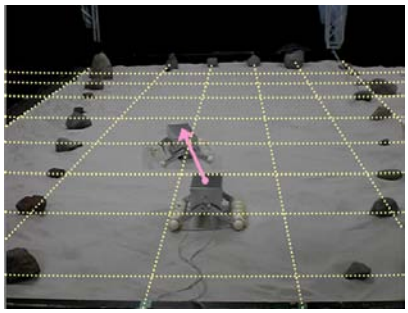

(a) Forward movement by outward screw revolution.

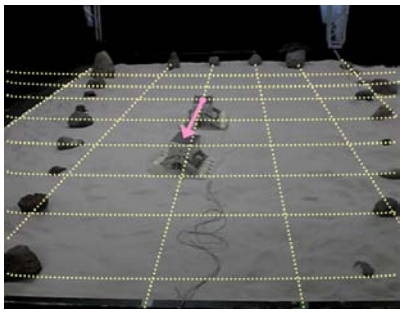

(b) Backward movement by inward screw revolution.

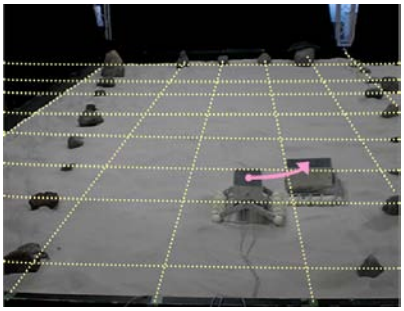

(c) Right sideways steering.

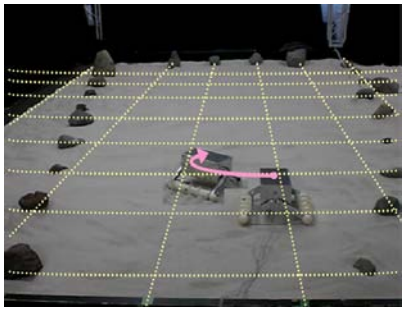

(d) Left sideways steering.

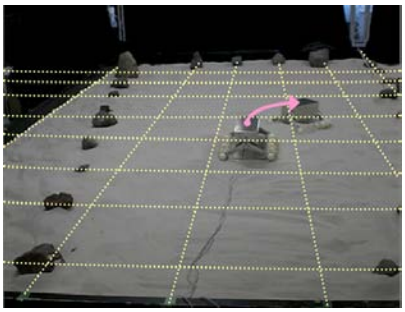

(e) Right-front steering.

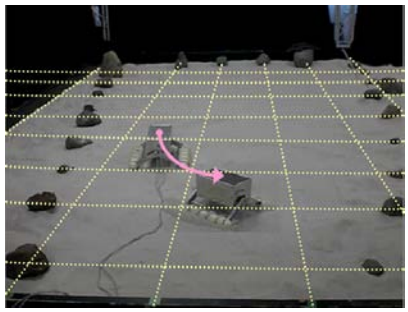

(f) Right-rear steering.

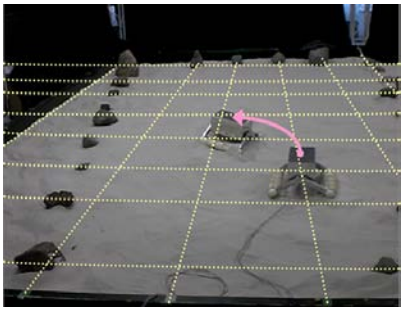

(g) Left-front steering.

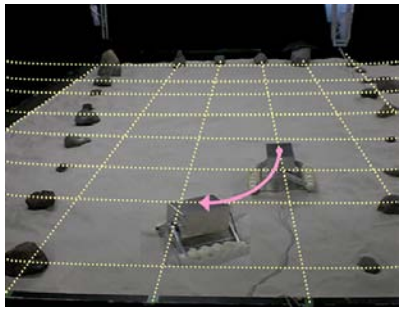

(h) Left-rear steering.

Figure 4.19 : Diverse mobility performance demonstrated by Screw Drive Rover prototype on soil surface.

Table 4.2 : Resulting classification of maneuvering trajectories.

ω_l \ ω_r	large *ccw*	small *ccw*	0	small *cw*	large *cw*
large *ccw*	↖	↖	↗	↗	↑
small *ccw*	↖	↖	↗	↑	↖
0	↙	↙	-	↖	↖
small *cw*	↙	↓	↘	↗	↗
large *cw*	↓	↘	↘	↗	↗

cw: clockwise rotation, *ccw*: counter clockwise rotation

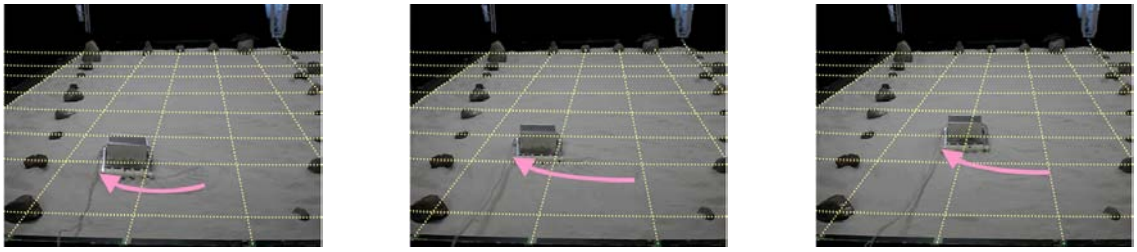

(a) ω_r: large *ccw*, ω_l: small *ccw*. (b) ω_r: large *ccw*, ω_l: large *ccw*. (c) ω_r: small *ccw*, ω_l: large *ccw*.

Figure 4.20 : Left sideways steering trajectories demonstrated by different inputs.

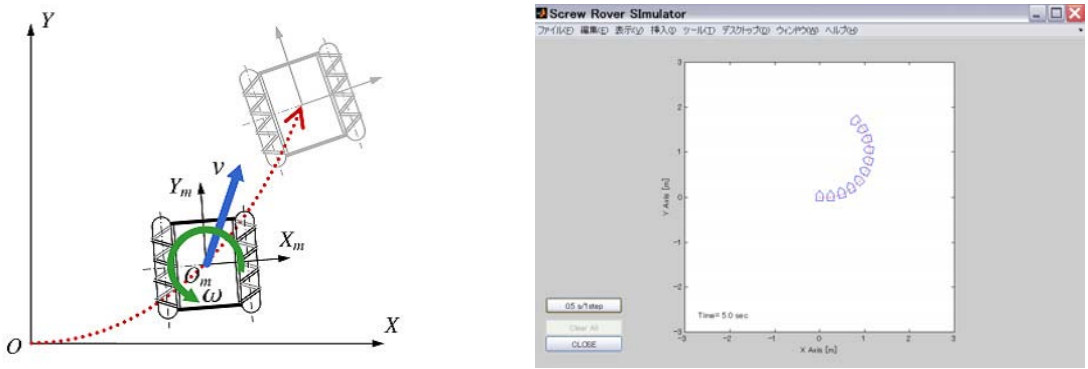

(a) Simulation model. (b) Simulation window.

Figure 4.21 : Analysis model of maneuvering trajectories.

Analysis on Maneuvers to Model

In contrast, empirical maneuvers shown in Table 4.2 suggest compliant force direction of the prototype qualitatively. By this analysis, it is clarified how forces should act on the rover to

Table 4.3 : Compatibility analysis of ideal force models resulted from empirical maneuvers.

ω_l \ ω_r	large *ccw*	small *ccw*	0	small *cw*	large *cw*
large *ccw*					
small *ccw*					
0			-		
small *cw*					
large *cw*					

achieve experimental trajectories. Table 4.3 shows rotational and translational forces, which should work. These forces were computed based on the empirical maneuvers. The resulting forces are an important guideline to mathematically model the soil-screw interaction.

4.4 Adaptability to Climbing Rocks

On actual terrains, small and large rocks are widely-scattered throughout the terrains. Large rocks should be avoided for mobile rovers, but the rovers are required to surmount small rocks. This section discusses the capability of climbing rocks by the Screw Drive Rover prototype. Basically, the prototyped rover is not appropriate to surmount the rocks by its forward movement. Climbing the rocks by its sideways movement, however, can be expected to be valid. So, the climbing capability was experimentally investigated by using the prototyped rover on the same terrain shown in Figure 4.16. Figure 4.22 shows the video images pertaining to climbing a rock by the sideways-steering movement. From this result, the prototyped rover was cable of climbing the 3-centimeter-height rock. The surmounting height is about half the screw unit's diameter and the capability indicates as well as a wheel or a track.

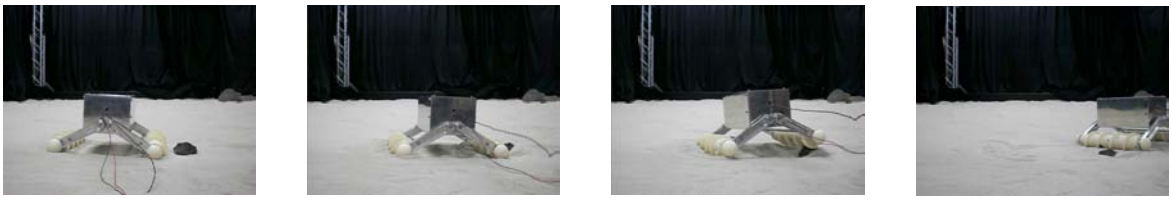

(a) Starting to move ($t = 0.0$ s). (b) Pushing a rock ($t = 2.6$ s). (c) Climbing a rock ($t = 4.1$ s). (d) Achievement ($t = 8.4$ s).

Figure 4.22 : Video images of climbing a rock by the Screw Drive Rover prototype.

4.5 Summary

This chapter presents the surface locomotion technique by the Archimedean screw units. Such locomotion method is on especially expected to exert better performance on the soft terrain because of its robustness to getting stuck. Meanwhile, academic researches on the surface locomotion by the screw units have been rarely conducted. So, at first, this dissertation attempted to accumulate engineering knowledge about the surface locomotion by the screw units. Specifically, the following two terms were experimentally studied:

Analysis on Empirical Trafficability

The fundamental trafficability of the single screw unit was investigated. To examine the trafficability, the laboratory tests were carried out as well as the maneuverability analysis. The experimental results showed the significant tendency that the drawbar pull increases with an increase of the slip, regardless of the load and the rotational velocity. Moreover, it was confirmed that the load and the rotational velocity did not affect the characteristics of the drawbar pull and the slip. On the contrary, the slip angle had much effect on the characteristics. This result leads to understanding of the propulsive force direction, and then enables synthetic discussions with the empirical maneuvers. Furthermore, comparative analyses were conducted by the experiments and the simulations. According to these, it was confirmed that the simulation plots by using the proposed model can meet the experimental results.

Analysis on Empirical Maneuverability

In this research, the Screw Drive Rover employing the dual screw units was proposed for a practical application system. As for mobility performance of the proposed system, its empirical maneuverability was elaborated through laboratory tests. From this elaboration, the maneuvering trajectories demonstrated by the system were analyzed and discussed. In addition to this, the empirical maneuvers enable to understand the propulsive force direction in each maneuver.

Chapter 5. Modeling and Analysis of Screw Subsurface Locomotion

5.1 Expectation for Lunar Subsurface Exploration

Recently, Lunar exploration has received a lot of renewed attention. A lot of scientific questions have remained unanswered concerning the Moon's origin, its evolution or chemical composition [6–8]. Unmanned robotic exploration of the lunar subsurface is getting more critical in the process of answering these questions. This will require developing more capable subsurface robotic exploration devices [174]. But, the conventional *in situ* approach of the lunar material can only provide localized measurements which cannot be extended to characterize large areas around the chosen sampling site. Implanting scientific instruments on the actual sampling site could potentially provide more information on a larger scale, which could ultimately help determining the global internal structure of the Moon, especially its core. The long term measurement on the Moon is arduous since ultra-cold temperature seriously limits power generation from photovoltaic cells at night. In the case of the Apollo lunar landing missions by NASA, a passive seismic network by 4 stations (at the Apollo 12, 14, 15 and 16 landing sites) was constructed to investigate lunar seismicity [3]. Figure 5.1 shows the Apollo 16 seismometer deployed on the Moon. By measuring lunar seismic events, The Passive Seismic Experiment (PES) produced the partial knowledge of the lunar interior structure, the distribution of the lunar seismic sources and the attenuation of the seismic waves. The seismometers were in a thermal shroud with a 20 layer multi-layer-insulation (MLI) as seen in Figure 5.1. In addition to this, the seismometers used thermal control instruments such as radioisotope heaters to survive lunar night. However, isotopes used in the radioisotope heaters have strong disadvantages (high toxicity, short half life and restricted availability), so that other methods without the radioisotope heaters are to be considered as alternatives [9]. So this dissertation focuses on a robotic system for burying a scientific instrument (such as a long-term seismometer) in the subsurface, effectively and continuously stabilizing its temperature environment by the thermal insulation of the lunar soil surrounding

Figure 5.1 : Apollo project's seismometer deployed on the Moon ©NASA.

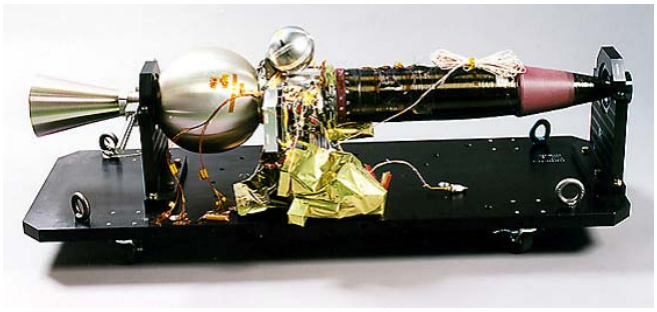

(a) Schematic of the LUNAR-A penetrator.

(b) Long-term seismometer.

Figure 5.2 : LUNAR-A penetrator system ©JAXA/ISAS.

it. The proposed mission concept is illustrated in Figure 5.4. To accomplish such mission, the instrument should be placed at least 1 meter beneath the lunar surface. Better contact with the surrounding regolith can also be achieved in this way, enabling the device to sense minor seism on the Moon.

Technologies related to subsoil extraction and analysis are notable for subsurface exploration aiming at finding traces of extinct life and living organisms. Up to the present date, there have indeed been some drilling tasks on the Moon as shown in Table 5.1. In particular, recently the Phoenix lander conducted scooping by its arm on Mars [146]. Boring or coring systems mounted on landers or rovers have been predominately considered for *in situ* analysis [140, 142, 143, 145]. While these systems are useful to sample small amount of materials, a boring rod requires a length equal to the target depth. Since an increase in frictional resistance is unavoidable during insertion, the diameter of the rod should be minimized up to the strict requirements imposed by

Table 5.1 : Past drilling missions on the Moon.

	Launch	Nation	Type	Reached Depth	Mechanism
Surveyor 3	1967	USA	unmanned	18 [cm]	scooping
Surveyor 7	1968	USA	unmanned	nondisclosure[4]	scooping
Apollo 11	1969	USA	manned	32 [cm]	core tube
Apollo 12	1969	USA	manned	37 [cm]	core tube
Luna 16	1970	USSR	unmanned	35 [cm]	boring
Apollo 14	1971	USA	manned	64 [cm]	boring
Apollo 15	1971	USA	manned	237 [cm]	core tube
Apollo 20	1972	USSR	unmanned	27 [cm]	core tube
Apollo 16	1972	USA	manned	221 [cm]	core tube
Apollo 17	1972	USA	manned	292 [cm]	core tube
Luna 24	1976	USSR	unmanned	160 [cm]	core tube

the space robots structural constraints considering the lunar gravitational environment. Excavating or digging techniques on the Moon have received a lot of attention from the perspective of ISRU (*In Situ* Resource Utilization). The bucket wheel excavator on the Moon, named BWE (Bucket Wheel Excavator) [141], has been proposed for ISRU. BWE is an useful technology for a large-scale excavation and an utilization of lunar materials. However, the limited reach of the arm driving the bucket makes it unsuitable for subsurface exploration. On the other hand, penetrators have been proposed as the most viable alternative for subsurface explorations [148–152]. JAXA/ISAS was planning on using this technology in the LUNAR-A project [148,150] as shown in Figure 5.2. However, the mission was canceled due to various reasons. Despite the benefits of these approaches, the maximum boring depth of such penetrators remains limited to a maximum of two meters as described in Appendix D, due to the system crash-worthiness or durability against a huge penetrating impact.

In consideration with these previous approaches, a new compact lightweight system is needed for conducting subsurface exploration by burying an instrument such as a long-term seismometer (with a size of at least 5 centimeters in both diameter and length as shown in Figure 5.2(b)). In an attempt to address the need for this kind of exploration device, this dissertation proposes a new subsurface investigation system incorporating an innovative technique for subsurface access and self-propulsion, called a subsurface explorer system. Table 5.2 shows comparison of

[4]The arm length of the Surveyor 7 was just 1.5 meters.

Table 5.2 : Comparison of drilling techniques in lunar and planetary explorations.

	Supporting Base	Opportunities	Reachable Depth
Bucket Wheel	need	retryable	depth-less
Penetrator	not need[5]	once	at best 2 meters
Boring	need	retryable	deep ($\leq$ drill length)
Subsurface Explorer	not need	potentially[6]	deep

subsurface drilling techniques in lunar and planetary explorations. On the basis of the comparison, the proposed idea may be the key in burying the long-period seismometer successfully. Further, the subsurface drilling technology is expected to apply not only space missions but also challenging tasks on the Earth, such as works in rescue site or construction field.

5.2 Related Works and Challenge of Subsurface Explorer

Until now, there have been several proposals of a lunar or planetary subsurface explorer in some countries [153–155, 157, 158, 160–171, 174, 175, 178–180]. The PLUTO (PLanetary Undersurface TOol) Mole by Richter *et al.* [155, 161, 165] is an unique tool aiming at sampling Martian subsoil. It is 2 centimeters in diameter, 28 centimeters in length and less than 1 kilogram in mass, and can advance by way of an internal sliding hammering mass. Two meters intrusion into a mechanical equivalent of the Martian soil was reported after conducting indoor experiments. The MMUM (Moon/Mars Underground Mole) developed by Stoker *et al.* [170] adopts the same propulsive mechanism as the PLUTO Mole. The dimensions of the device are 4 centimeters in diameter, 60 centimeters in length and less than 2 kilogram in mass. The maximum reaching depth is set to be 2 meters below the surface. However, the experimental data indicated that MMUM can actually penetrate into dry sand up to a depth of about 60 centimeters [170]. The relatively shallow depth that can be bored down shows the limitations of the hammering propulsion by compressing fore-soil layer. Moreover, its small diameter makes it an impractical approach for burying instruments into compacted lunar soil. On the other hand, the mole-type drilling robot of Watanabe *et al.* [163] is one of the few complete system which possesses a 10 centimeters in diameter. However, it could not execute a normal drive due to some mechanical issues. Kudo *et al.* [154] have studied a robotic system for subsur-

[5] Penetrators do not need ground bases, but they need a releasing mechanism from mother satellites.

[6] If subsurface explorers can come back to surfaces, they possess opportunities to burrow into other areas.

face exploration, and discussed soil removal by a vibratory horn. Following this work, an advanced drilling robot, named MOGURA2001, has been developed by Yoshida *et al.* [160, 162]. MOGURA2001 can discharge subsoil to the surface by using a bucket conveyor, and is able to reach a depth of about 30 centimeters into a lunar regolith simulant. However, mechanical interference with soil particle is difficult to avoid during operation. Moreover, the same boring issues regarding the target depth to be reached was encountered with this robot, its only penetrating force coming from its own weight. Other proposals to date such as the IDDS (Inchworm Deep Drilling System) [164, 169] and the SSDS/RPDS (Smart Space Drilling System/Robotic Planetary Drilling System) [167, 168] have been presented, focusing mainly on their working concept or their structural framework, but their feasibility of accessing the subsurface has not been proved yet. In addition to these ideas, there are some concepts and partial experiments [153, 154, 158, 166] Recently, a new regolith drilling robot based on a screw flight has been recently proposed by Yasuda *et al.* [171, 173, 175, 180]. The first prototype of this system utilizes the reaction torque of a DC motor and is able to reach an intrusion depth of 26.5 centimeters targeting fly ash [171]. Then, second and third prototypes could achieve drilling into the fly ash to about 50 and 60 centimeters in depth, respectively [175, 180]. Its minimum diameter is, however, limited to 4$\sim$5 centimeters and its penetration state is an insertion without removing fore-soils. Accordingly, these system require larger driving torques due to their screw-in characteristics. Moreover, an earthworm-typed drilling robot has been also proposed [178, 179]. This robot consists of an earth-auger and a peristaltic crawling structure like an earthworm, and it reached a depth of about 20 centimeters in fine red soils. Likewise, there has also been Cryobot [159] that penetrates into icy crust of Europa, the sixth moon of the planet Jupiter. The Cryobot has capability to melt the icy crust, and then can access the interior. Its targeting environment is quite different from the lunar one. Characteristics of the past proposals are classified as shown in Table 5.3. According to these considerations, several issues remain to be elucidated. The conventional shape of the representative devices is shown in Table 5.4.

In other applications, there have been robotic systems inspired by plants' roots [172, 176]. Likewise, biomimetic inspiration robots (*e.g.* the bivalve [177] and the moke crab [181]) have been studied as well. These applications realize interesting mechanisms but they penetrate based on soil compaction. Therefore, they would possess potential issues similar with ones of the penetrators, such as size-limitation or power performance. As a result, it is unsuitable to apply these to the subsurface explorer for burying the instrument.

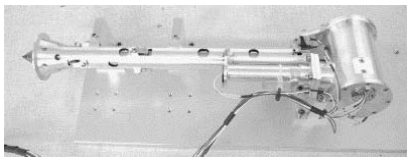

(a) PLUTO Mole [161].

(b) IDDS [164].

(c) MMUM [170].

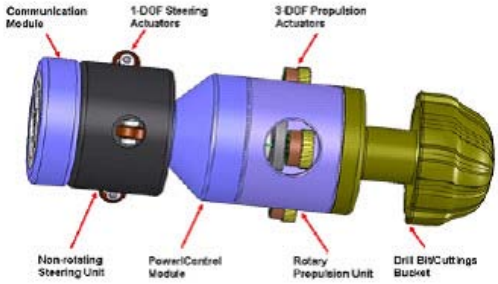

(d) SSDS/RPDS [167].

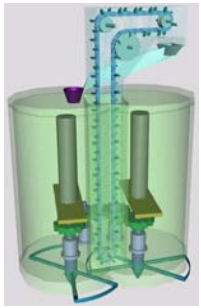

(e) MOGURA2001 [160].

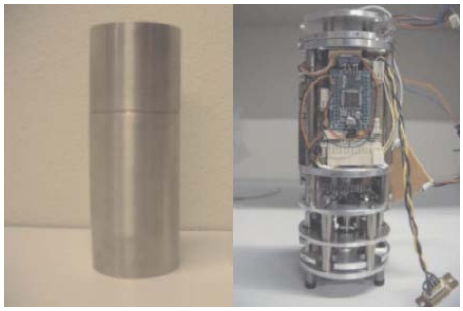

(f) Mole-type Robot [163].

(g) Regolith Drilling Robot [180].

(h) Earthworm-type Robot [179].

Figure 5.3 : Conventional subsurface explorers.

Table 5.3 : Mechanism classification of the conventional subsurface explorers.

	1) Make a Space (*transport*)	2) Advance Forward
PLUTO Mole [155, 161, 165]	soil compression (-)	internal hammering mass
MMUM [170]	soil compression (-)	internal hammering mass
Mole-type Robot [163]	blade intake (*torsional vibration*)	pushing discharge
MOGURA2001 [160, 162]	blade intake (*bucket conveyor*)	only weight
IDDS [164, 169]	coaxial drill bit (*screw transport*)	inchworm-like with shows
Regolith Drilling [171, 175, 180]	screw drill (*screw transport*)	screw propulsion
Earthworm-type [178, 179]	screw drill (*screw transport*)	earthworm-like with screw
SSDS/RPDS [167, 168]	diamond bit (*carriage*)	side wheels

Table 5.4 : Practical achievements of the conventional subsurface explorers.

	Max.(Min.) Dia.[7]	Length	Reached Depth	Targets
PLUTO Mole [155, 161, 165]	2(2) [cm]	25 [cm]	200 [cm]	MSMS[8]
MMUM [170]	4(4) [cm]	60 [cm]	60∼70 [cm]	dry sand
Mole-type Robot [163]	10(10) [cm]	27∼32 [cm]	no data	-
MOGURA2001 [160, 162]	27(16) [cm]	30 [cm]	∼31.5 [cm]	FJS-1[9]
IDDS [164, 169]	15(15) [cm]	100∼200 [cm]	no data	-
Regolith Drilling [180]	8(6) [cm]	36.5 [cm]	∼60 [cm]	fly ash
Earthworm-type [178, 179]	13(6.5) [cm]	80 [cm]	∼20 [cm]	red soil
SSDS/RPDS [167, 168]	16(15) [cm]	50 [cm]	no data	-

5.3 Robotic Subsurface Explorer

5.3.1 Robotic Locomotion in Soil

Mobile robots have been used in various fields, such as for entertainment, assistance, exploration, maintenance or inspection. While there have been some studies on biomimetic underground robots (*e.g.*, the earthworm [127] or the inchworm [120]), the studies on their robotic locomotion have been usually restricted to a movement on flat and rigid surfaces or under water. In general, the subsurface environment is constituted of constrained three-dimensional deformable soils. Furthermore, the unsteady soils behavior makes the environment even more complicated.

[7] Maximum and Minimum Diameters are defined as borehole diameters of the subsurface explorers.
[8] MSMS is a clipped word of Martian Soil Mechanical Simulant [155].
[9] FJS-1 is one of the Japanese lunar soil simulants, which is produced by Shimizu Corporation [107].

Despite this added complexity, robotic subsurface explorers have some unique merits for future lunar mission:

- Reachable depth is not mechanically limited by the robot length.
- Large bases on the surface is not required for penetration.
- System can be compact size, lightweight and low power.
- Expansion to multiple applications in space developments can be expected; *e.g.*, burying scientific instruments, *in situ* analysis, artificial seisms or construction tasks.

5.3.2 Synopsis of Robotic Subsurface Explorer System

In particular, lunar robotic applications needs to accommodate harsh conditions such as ultra-high vacuum, low gravity, wide temperature variation, and requires being able to operate on or within the fine regolith layer. The schematic of the proposed mission sequences are illustrated in Figure 5.4. The following assumptions are set forth regarding the lunar robotic subsurface exploration system:

- A Micro Rover shall carry the subsurface explorer to the target area.
- The Subsurface Explorer shall be tethered to the Micro Rover for power supply.
- The Subsurface Explorer shall be about 0.1 meters in diameter since the long-term seismometer's diameter shall be about 0.05 meters.
- Target depth shall be set to a few meters beneath the lunar surface.
- Target soil-layer is assumed to be lunar regolith, which is high frictional and high cohesive soil, and has large relative density under shallow zone [1–3].
- The lunar gravitational field is assumed to be almost constant for the robot system [4].

5.3.3 Subsurface Locomotion Principle

Systematic Synopsis

Realization of a locomotion mechanism in the subsurface environment is a challenging task, and is quite difficult to model mathematically. In light of the few studies concerning subsurface

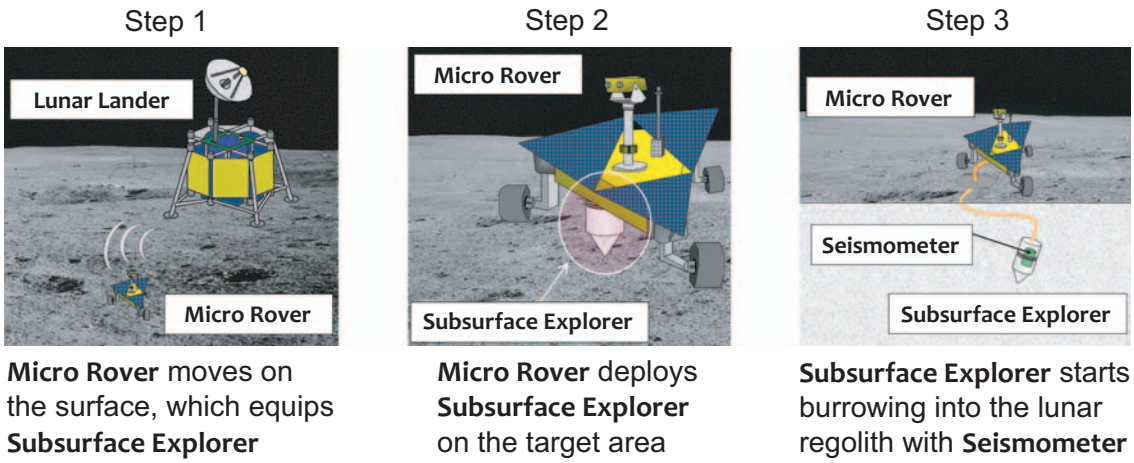

Figure 5.4 : Schematic of robotic subsurface exploration mission on the Moon.

locomotion, it must be concluded that such mechanism is still poorly understood. Hence, the following strategies for the subsurface locomotion scheme has been defined based upon the description by Watanabe *et al.* [163]. These strategies also cover the methods for mechanically accomplishing the two principal phases:

1. Make a Space

- Compression of fore-regolith
- Backward removal and transportation of fore-regolith
  - Internal transportation with intaking and discharging fore-regolith
  - External transportation without intaking fore-regolith

2. Advance Forward

- Generation of propulsive forces actively
  - Utilization of contact with surrounding regolith
  - Utilization of excavated regolith
  - Self advancement without utilizing regolith
- Without generation of propulsive forces (only using the system's own weight)

Prediction of Static Propulsive Resistance

Based upon Rankine's soil pressure theory, frictional resistance acting a cylinder into soil is predicted. For the subsurface locomotion, there are actually lateral skin friction and excavating

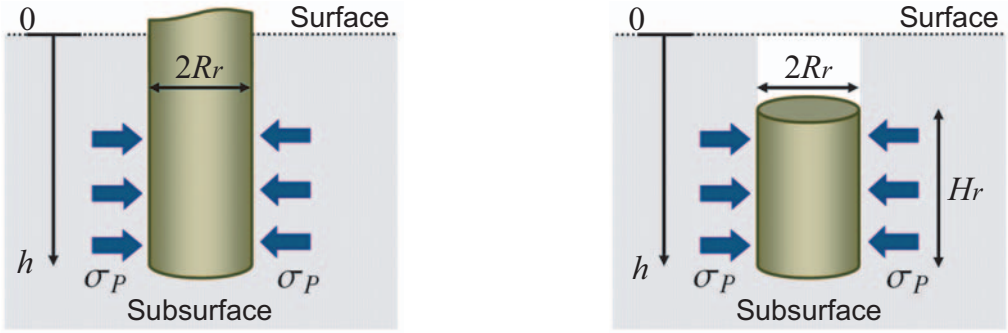

(a) Boring drill model. (b) Subsurface explorer model.

Figure 5.5 : Models of lateral soil frictional.

resistance as propulsive resistances. However, the skin friction works universalistic resistance against the cylinder's lateral surface throughout the locomotion as illustrated in Figure 5.5(b). Rankine's passive soil pressure σ_P at a corresponding depth z is expressed as follows [109].

$$\sigma_P(z) = (p_0 + \rho g z) K_P + 2C\sqrt{K_P} \tag{5.1}$$

where p_0 is an external pressure, ρ is soil bulk density, g is a gravitational acceleration, C is cohesion stress, and K_P is Rankine's passive soil pressure coefficient. Moreover, as the cylinder shape, the cylinder has H_r in length and R_r in radius. Here cohesionless soil ($C = 0$) and $p_0 = 0$ are simply assumed. Given apex depth h and a frictional coefficient μ between the soil and the cylinder, the skin friction F_r is finally derived as follows.

$$\begin{aligned} F_r &= \pi R_r \mu \int \sigma_P \cdot dz \\ &= 2\pi R_r \mu K_P \int_{h-H_r}^{h} \rho g z \cdot dz \\ &= \begin{cases} \pi R_r \mu K_P \rho g h^2 & \text{if } \ 0 \le h \le H_r \\ \pi R_r \mu K_P \rho g (2hH_r - H_r^2) & \text{otherwise } \ (h > H_r) \end{cases} \end{aligned} \tag{5.2}$$

According to Eq. (5.2), a relation between h and F_r can be calculated. Figure 5.6 shows the simulation results, where in the boring system its effective drill length H_r is the same with the reached depth ($H_r = h$). Likewise, the subsurface explorer system has its effective length H_r that is constant ($H_r \le h$). In these simulations, the propulsive force F_r was evaluated as the required mass since system weight works as a nominal propulsive force. Table 5.5 shows the simulation parameters. From Figure 5.6, the subsurface explorer performs much better than the boring system in light of limited propulsive forces. To reach 1 meter below the surface, however, even

the subsurface explorer needs larger propulsive force to for its advancement. Hence, according to Figure 5.6(b), it is concluded that the subsurface explorer must make a space and actively generate a propulsive force except its weight. Also, these simulation results do not depend on gravitational environments since the gravity effect is ultimately compensated in calculating F_r.

Table 5.5 : Parameters to estimate depth limit.

	R_r [m]	H_r [m]	g [m/s^2]	ρ [kg/m^3]
Boring Drill	0.05	h	9.81	1600
Subsurface Explorer	0.05	0.3	9.81	1600

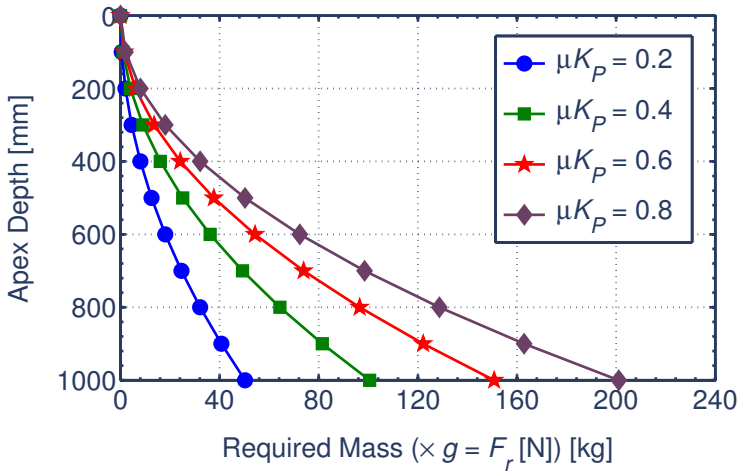

(a) Case of boring drill.

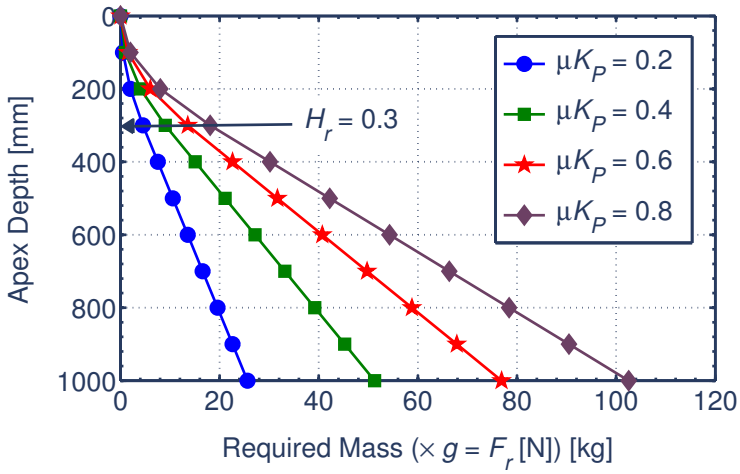

(b) Case of subsurface explorer.

Figure 5.6 : Propulsive depth limit estimation.

Estimate of Compression Limit

In the established strategy, the soil compression was indicated as one possible technique to make a space. But the soil compression is an impractical technique due to the high compacted lunar regolith layer [3]. This research evaluates the possibility of using the soil compression method to analyze this inference.

At first, void ratio e of terrain is defined as follows [3, 109].

$$e = \frac{V_v}{V_s} \tag{5.3}$$

where V_v and V_s is the volume of void and soil, respectively.

Next, the compression index C_C is defined as follows [3].

$$C_C = -\frac{\Delta e}{\Delta \log_{10} \sigma} \tag{5.4}$$

where σ is compression pressure, and Δe and $\Delta \log_{10} \sigma$ is the difference of e and $\log_{10} \sigma$ between before and after additional compression, respectively. In fact, C_C of the sampled lunar regolith was measured in the past Apollo projects [3]. Assuming the initial void ratio e_0 and the initial pressure σ_i, a relationship between σ and e can be introduced by applied pressure σ_a by

$$e = -C_C \log_{10} \left(\frac{\sigma}{\sigma_i} \right) + e_0, \tag{5.5}$$

$$\sigma = \sigma_i + \sigma_a. \tag{5.6}$$

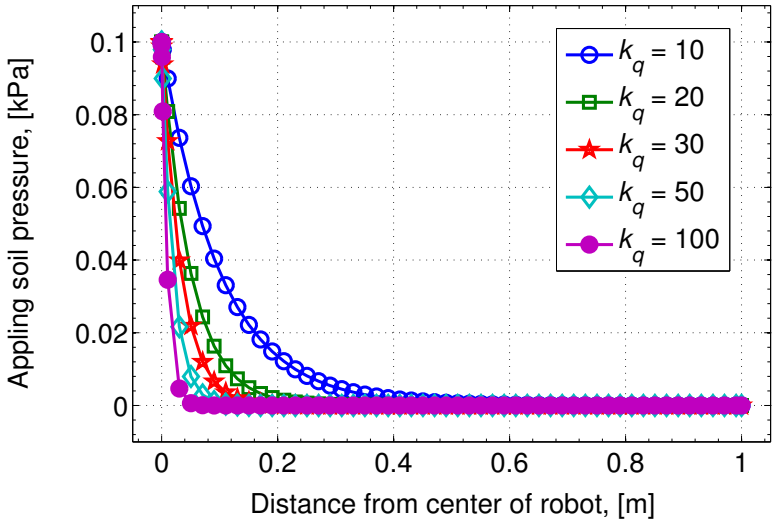

Figure 5.7 : Simulation result of soil pressure propagation range.

Next, stress propagation of the subsurface soil is computed. Applying the compression stress σ_a, the soil stress σ_b at propagation distance D_b is defined as follows.

$$\sigma_b = \sigma_i + \sigma_a \cdot \exp\left(-k_q D_b\right) \tag{5.7}$$

where k_q is a coefficient of stress decline percentage.

Thus, given compression pressure σ per unit area, a generated distance D_{C_C} can be calculated as follows.

$$D_{C_C} = \int_0^{D_{cr}} \left(\frac{e_0}{e_0+1} - \frac{e}{e+1}\right) \cdot dD_b \tag{5.8}$$

where D_{cr} is calculation range, and it is considered the subsurface soil is homogeneously distributed in a horizontal direction. Given the compression stress acts on a central axis of the subsurface explorer, the stress propagation can be given as shown in Figure 5.7. As for the parameter in Figure 5.7, σ_i and D_{cr} were set to be 100 Pa and 1 meter, respectively. Practically, the stress propagation would not widely exert influence due to high friction and cohesion and irregular shape of the lunar regolith [3].

Figure 5.8 depicts numerical simulation results of the soil compaction technique. In the simulations, three types of the compression indexes were used: C_C were 0.050 (weakly-compressible), 0.075 (middle) and 0.10 (highly-compressible). As the fixed parameters, $e_0 = 1.2$ (loose soil), $D_{cr} = 1\,\mathrm{m}$ (calculation range) and $\sigma_i = 1\,\mathrm{kPa}$ were selected. Assuming the lunar regolith layer, C_C indicates about 0.10 in its shallow area but C_C becomes about 0.050 in a deeper area than tens of centimeters [3]. In accordance with Figure 5.8, the subsurface explorer needs to exert a few hundreds of kilo Pascals of compression pressure to make enough space. Therefore, it is concluded that the soil compression is an impractical technique. To achieve this strategy, that is, a technique for the removal of fore-soil backward is necessary.

Key Concept for Subsurface Drilling

Considering that compressing the regolith is not a practical technique for making a space due to the lunar regolith layer being already compacted [3] and that advancing within the lunar soil using only the robot's own weight is also impractical as indicated in the subsequent section. Also, in this research an applicability of the soil compaction was discussed above. Thus the subsurface explorer should remove fore-regolith and actively generate its own propulsive force. Numerous methods can be conceived to achieve this strategy. Figure 5.9 illustrates the representative embodiments.

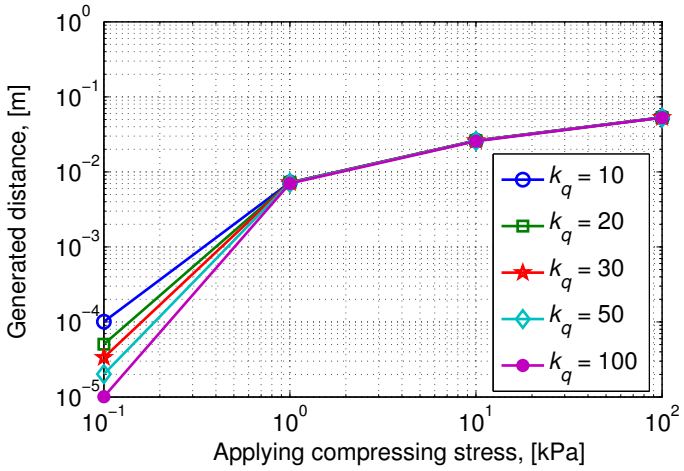

(a) $C_C = 0.050$ (weakly-compressible).

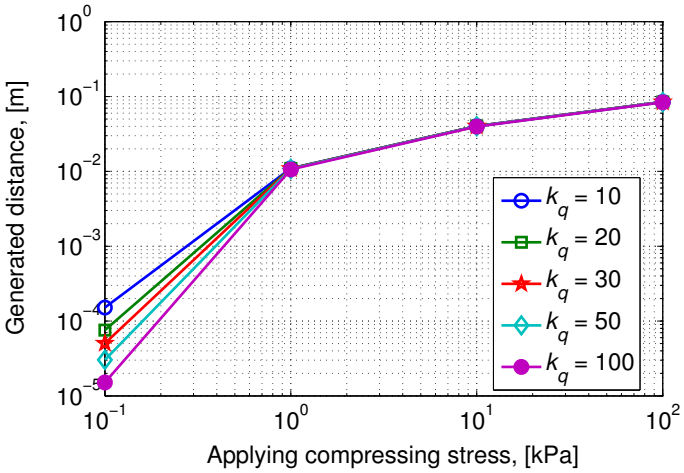

(b) $C_C = 0.075$ (middle-compressible).

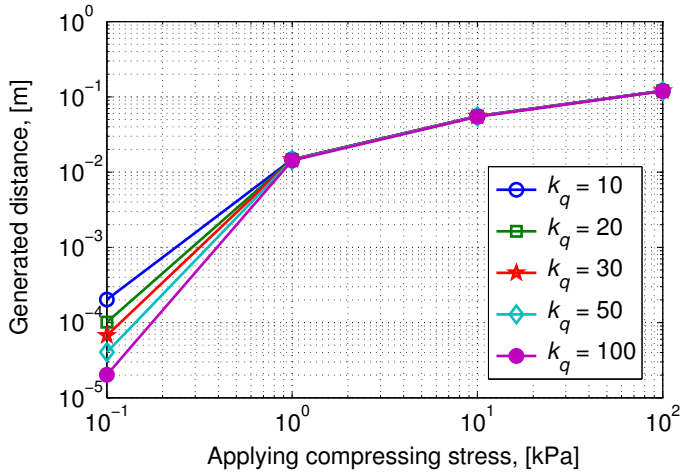

(c) $C_C = 0.10$ (highly-compressible).

Figure 5.8 : Estimated results of compressing soil to make a space.

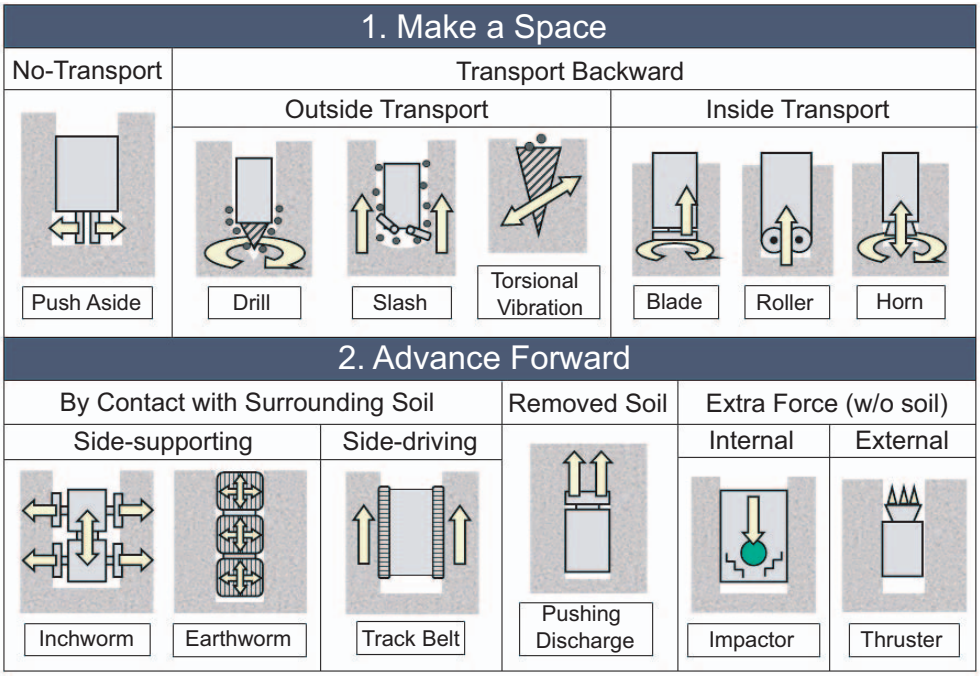

Figure 5.9 : Robotic mechanisms for the subsurface locomotion strategies.

5.4 Fundamental Drilling Performance of SSD Unit

According to the previous section, the key techniques for the robotic subsurface explorer are removing fore-soil and reliably exerting a propulsive force within soil. To cope with fine soils while avoiding clogging of mechanical components, a simple drilling mechanism is preferable. Hence, this dissertation basically considers conical and cylindrical screw drills.

The geometry, the prototype and the drilling principle of the basic conical screw unit, named SSD (Single Screw Drilling), are shown in Figure 5.10. The developed SSD prototype corresponds to the fundamental screw model of a double rotating screw mechanism, and has thus been used effectively in the experimental analyses of a novel mechanism presented in the subsequent sections. The SSD prototype has one DC geared motor (SCR-16-2512 and IG-16V-1/560; CITIZEN SAYAMA Co., Ltd.) with an encoder (MR-16-P/R128; CITIZEN SAYAMA Co., Ltd.). The motor for driving the screw is attached by spur gears with reduction ratio 1/1, respectively. The SSD prototype also consists of a body part and a single screw drilling part. The screw part also has an inner cone and a helical screw flight which winds around the cone. Further, the total screw length is L, the maximum cone diameter is D_c and the maximum screw diameter is D_s. In the SSD prototype system, L is 0.05 m, D_c is 0.03 m, D_s is 0.05 m and the screw slope angle is designed to be 10 deg. Additionally, an external pushing down force was not given to the SSD in the experiments. Such conical screw can be mathematically expressed as a function

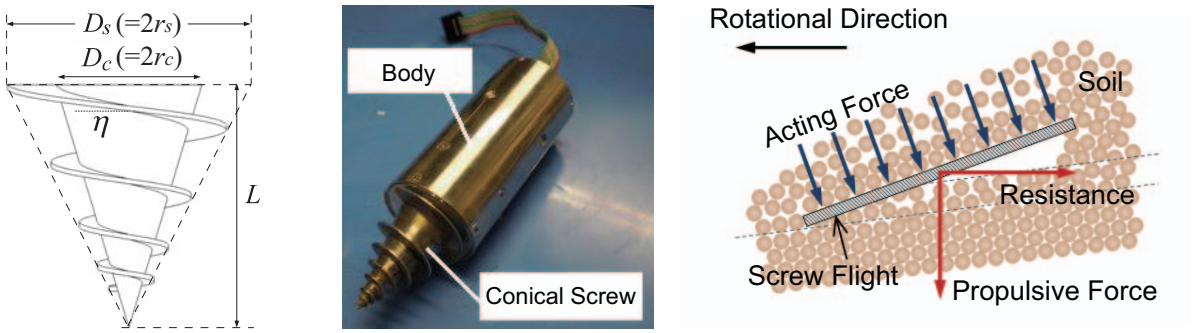

(a) Geometric model. (b) Prototype. (c) Dynamic principle.

Figure 5.10 : Single conical screw unit: SSD.

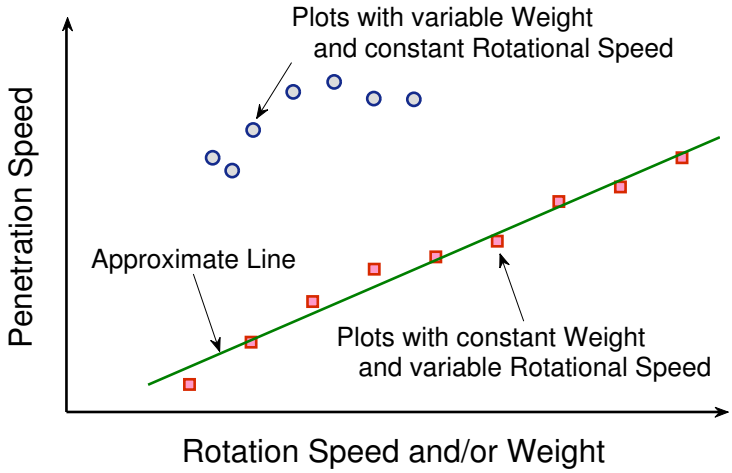

Figure 5.11 : Basic drilling characteristics of SSD.

of a logarithmic spiral with variable pitch. Figure 5.10(c) illustrates the simplified two dimensional dynamic principle acting on the screw flight. According to this schematic, even though the system weight affects the screw penetration, the propulsive force with soil transportation by the screw rotation is confirmed to be a key factor. The propulsive force can be axially generated by the effects of the normal force and the contact friction of the soil on the screw flight. In fact, amphibious vehicles driven by this propulsive force obtained through the rotating screw have been developed (*e.g.*, [34]).

For the simple screw model SSD, the analysis of its fundamental drilling performance with various conditions indicates some significant factors for understanding a screw drilling mechanism. Figure 5.11 depicts the experimental results of the SSD prototype with a quartz sand box. In the experiments, the reaction of the driving motor against the body is canceled by hand in order to examine the drilling performance with respect to the SSD geometry. As measurement

values, the rotational speed of the driving motor was obtained by encoder, and the average penetration speed was analyzing the recorded movies by a stationary camera during experiments. According to these results, the average penetration speed is proportional to its rotational speed but is not affected by its weight. This remark also denotes the penetration speed becomes a same value with the same rotational speed under especially a shallow area, even though much power is needed when the system has much weight. In these experiments, the SSD drove in a shallow area, and there thus is a zone which increases the penetration speed with weight gain. The rotation speed, however, would become more dominant for the penetration speed in deeper area. The important point here is not a quantitative change with its scale but rather its tendency. Consequently, the penetration states can be mainly governed by the rotational speed and the weight factor has to be consistently taken into account in the evaluation of the SSD drilling performance. That is because that the screw rotation provides the removal of fore-soil and the propulsive force at the same moment as illustrated in Figure 5.10(c). On the other hand, the screw penetration can be basically achieved when the sum of the system weight and the internal and external propulsive forces becomes larger than the resistance of the soils. In other words, a certain penetration limit exists based on that dynamics. Therefore, the tendencies in Figure 5.11 are valid when the screw can penetrate into the soils, and this dissertation deals with this situation.

5.5 Mathematical Modeling of Screw Drilling

5.5.1 Dynamics Modeling

Theoretical analyses are absolutely essential for ensuring the reliability of a robot driven in natural environment with uncertainties. The soil-screw interaction model is introduced here by combining the geometric model stated previously. Figure 5.12 shows the schematic of the interaction model, and it depicts a logarithmic helix but assuming $\alpha_c = 0$ it also can apply to a cylindrical helix. In this dissertation, the screw drills are assumed to drill into subsurface downward in a vertical direction. Moreover, the soil on the screw flight is also assumed to be a continuum model and thereby the each interacting force is defined. As coordinates fixed on the screw flight, X_S axis parallel to the screw flight surface of **P** and Y_S axis perpendicular to the X_S axis are set as shown in Figure 5.12(b). At first, the EOMs of the soil on ΔA_{sc} in X_S-Y_S

coordinates can be obtained as follows.

$$m_s\ddot{X}_S = D_X - W\sin\eta - \sum_{i=0}^{3} F_i\cos(\alpha_i - \eta) \tag{5.9}$$

$$m_s\ddot{Y}_S = N - D_Y - W\cos\eta - \sum_{i=0}^{3} F_i\sin(\alpha_i - \eta) \tag{5.10}$$

and also,

$$\begin{aligned} D_X &= D_1\cos\eta - D_2\cos\eta\,(= D\cos\eta) \\ D_Y &= D_1\sin\eta - D_2\sin\eta\,(= D\sin\eta) \end{aligned} \tag{5.11}$$

where m_s is mass of the soil on ΔA_{sc}, N is normal force, F_0 is frictional force of the soil against the upper surface of the screw flight, F_1 is frictional force of the soil against the lateral surfaces of the cone or the cylinder part, F_2 is frictional force of the soil against the lower surface of the screw flight, F_3 is frictional force of the external adjacent soil around the soil, α_i is acting angle of each force F_i ($i = 0,1,2,3$), W is weight of the soil, and $\ddot{X}_S$, $\ddot{Y}_S$ are the second order differentials of X_S, Y_S by a time t, respectively. Furthermore, D_1 and D_2 are downward and upward forces from the adjacent soils respectively, then D_X and D_Y intend X_S and Y_S component of D, and D denotes the resultant force given by $D_1 - D_2\,(\geq 0)$. Therefore, the derivation of unknown N and D would be key factors for calculating the total frictional resistance of the screw drills.

Next, the motion trajectory of the screw flights is discussed for introducing N. At angle θ, the trajectory per one revolution of the screws is expressed as a screw penetrating angle ζ as illustrated in Figure 5.13.

$$\zeta = \arctan\left(\frac{2\pi r_{sc} f}{v_z}\right) \tag{5.12}$$

where v_z is the screw's penetrating speed downward in a vertical direction, and the trajectory matrix $\mathbf{Q}$ of $\mathbf{P}$ in X_S-Y_S coordinates can be described as follows.

$$\mathbf{Q} = \begin{bmatrix} Q_X \\ Q_Y \end{bmatrix} = \begin{bmatrix} -v_z\sin\eta - 2\pi r_{sc} f\cos\eta \\ -v_z\cos\eta + 2\pi r_{sc} f\sin\eta \end{bmatrix} \cdot t \tag{5.13}$$

As a kinematic constraint of the soil behavior, the soil is assumed to be transported along the upper surface of the screw flight and the constraint $Y_S = Q_Y$ introduces $\ddot{Y}_S = \ddot{Q}_Y \to 0$ under a steady drilling state. Hence, N can be written as follows.

$$N = D_Y + W\cos\eta + \sum_{i=0}^{3} F_i\sin(\alpha_i - \eta) \tag{5.14}$$

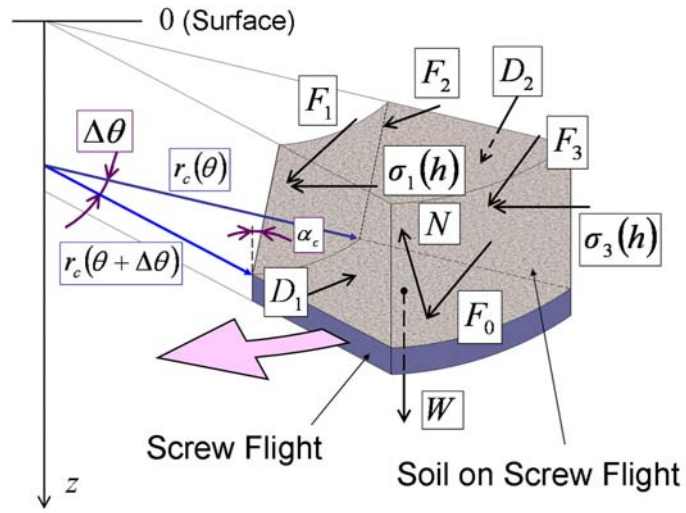

(a) Three-dimensional diagram.

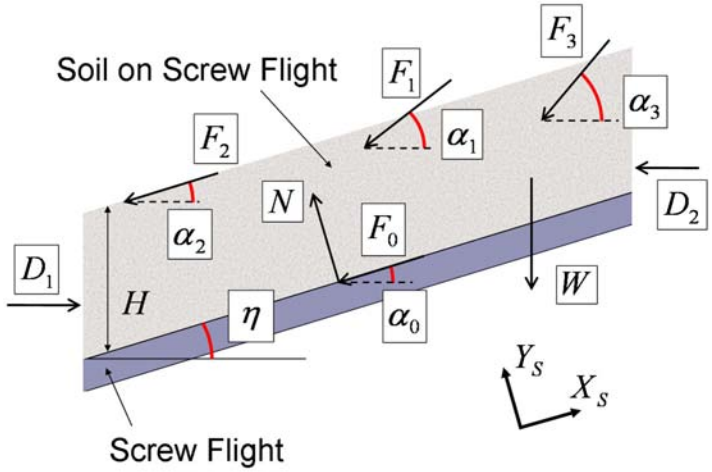

(b) Two-dimensional diagram.

Figure 5.12 : Interactive drilling model of the screw flight and the soil.

In addition, the acting force matrix **F** and the weight W are defined as the following equations.

$$\mathbf{F} = \begin{bmatrix} F_0 \\ F_1 \\ F_2 \\ F_3 \end{bmatrix}^T = \begin{bmatrix} \hat{\mu} N \\ \hat{\mu}\,\sigma_1(z)\,H r_c \sec\alpha_c \cdot \Delta\theta \\ \hat{\mu}\,\dfrac{\sigma_2(z)}{K_0} \cdot \Delta A_{sc}(\theta - 2\pi) \\ (\mu\sigma_3(z) + C)\,H r_s \sec\alpha_s \cdot \Delta\theta \end{bmatrix}^T \tag{5.15}$$

$$W = \gamma H \Delta A_{sc}(\theta) \tag{5.16}$$

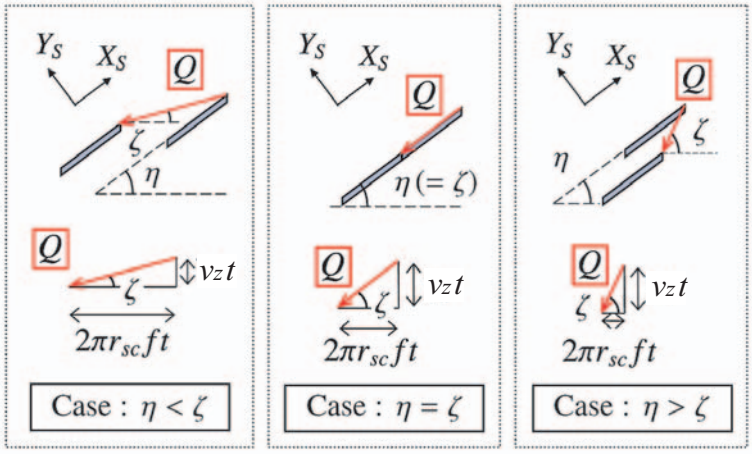

Figure 5.13 : Motion trajectories of screw flight in 2D elevation.

where $\sigma_1(z)$ is a lateral soil stress against the inner cone/cylinder sleeve surface at a depth z, $\sigma_2(z)$ is a soil stress on **P** at a depth z, $\sigma_3(z)$ is lateral soil stress on the edge of a screw flight at a depth z, γ is a soil bulk weight, μ is a frictional coefficient between soils, $\hat{\mu}$ a frictional coefficient between the screws and the soil, H is height of the soil, α_c and α_s are the half apex angle of the inner cone/cylinder and the ideal cone/cylinder composed by the screw flight respectively (see Figure 2.1). Here F_3 is essentially given by soil shear stress. Unlike the surface locomotion, the subsurface drilling assumes that the sheared soil on the screw flights satisfies the Mohr-Coulomb failure criterion due to its strict constraint occluded by the surrounding soils. Therefore, F_3 does not need to involve the shear displacement as represented in Eq. (3.15).

Furthermore, α_i $(i = 0,1,2,3)$ of the logarithmic helix is expressed as follows.

$$\begin{aligned} \alpha_0 &= \alpha_2 = \eta \\ \alpha_1 &= \arctan\left(\frac{L}{r_0}\cdot\frac{-a}{\sqrt{a^2+1}}\right) \\ \alpha_3 &= \arctan\left(\frac{V/f}{2\pi R_0\cos\bar{\alpha_3}}+\tan\bar{\alpha_3}\right) \quad \text{where } \bar{\alpha_3} = \arctan\left(\frac{L}{R_0}\cdot\frac{-a}{\sqrt{a^2+1}}\right) \end{aligned} \tag{5.17}$$

In accordance with the above definitions, unknown N can be definitely obtained by applying Eqs. (5.14) $\sim$ (5.17) as follows.

$$N = D\sin\eta + W\cos\eta + F_1\sin(\alpha_1-\eta) + F_3\sin(\alpha_3-\eta) \tag{5.18}$$

Also, the height H is defined as follows.

$$2\pi \geq \hat{\theta} \geq 0 \Longrightarrow H = \begin{cases} h-l & : 0 \leq \theta \leq 2\pi \\ p & : 2\pi \leq \theta \leq \theta_{end} \end{cases} \tag{5.19}$$

$$2\pi < \hat{\theta} \Longrightarrow H = \begin{cases} h-l & : 0 \leq \theta \leq 2\pi \\ k_H \dfrac{v_z}{f} & : 2\pi \leq \theta \leq \hat{\theta} \\ p & : \hat{\theta} \leq \theta \leq \theta_{end} \end{cases} \tag{5.20}$$

where h is apex depth, $\hat{\theta}$ is angle at $p(\hat{\theta}) = v_z/f$ (however actual $\hat{\theta}$ of the logarithmic helix is derived by Eq. (2.5) as two values, p is assumed to be specific value in the range of $2\pi \leq \theta \leq \theta_{end}$, and H is assumed to be equal to $h-l$ in the range of $0 \leq \theta \leq 2\pi$), k_H is an expansion coefficient of H by a soil flow and its effective range is set to be $1 \leq k_H \leq pf/v_z$. When the penetration speed v_z is constant and drilled borehole is assumed to be self-standing, k_H can simply become 1.

As the next step, the resultant force D is introduced. In this dissertation, based on the dynamic discharging behavior of soils, the sum of the rotating moment by D is defined as the total change of potential energy by uplifting the whole soils on a screw flight from $\theta = 0$ to $\theta = \theta_{end}$. Accordingly, the following relation is here given.

$$\int_{\theta=0}^{\theta=\theta_{end}} Dr_{sc} \cdot d\theta = \frac{1}{2\pi} \int_{\theta=0}^{\theta=\theta_{end}} WH \tan\eta \tag{5.21}$$

As a result, the total frictional resistance moment M_T, acting from the soil on the screw flights, can be calculated as follows.

$$M_T = \int_{\theta=0}^{\theta=\theta_{end}} (\Delta M_N + \Delta M_F) \tag{5.22}$$

and also,

$$\Delta M_N = N r_{sc} \sin\eta \tag{5.23}$$

$$\Delta M_F = \mathbf{F} \cdot \mathbf{r} \tag{5.24}$$

$$\mathbf{r} = \begin{bmatrix} r_{sc}\cos\alpha_0 & r_c\cos\alpha_1 & \exp(2a\pi)\, r_{sc}\cos\alpha_2 & 0 \end{bmatrix}^T \tag{5.25}$$

$$z = h - l - \frac{H}{2} \tag{5.26}$$

where $\mathbf{r}$ is coefficient matrix of $\mathbf{F}$ for converting into torques and z is corresponding depth for each soil stress defined in Eq. (5.15).

5.5.2 Cavity Expansion Theory

In the light of soil mechanics, soil pressure is basically composed of the weight and the cohesion of soils [102, 109]. Previously, the soil resistances were defined as the friction by the interactive contact forces. However, the effect of compressing soil by the screw penetration is actually needed to be included in $\sigma_1(z)$, $\sigma_2(z)$ and $\sigma_3(z)$ for practical estimation. So this research attempts to apply a cavity expansion theory [105, 108] to the soil-screw interaction model.

Generally, the cavity expansion theory has been applied in order to evaluate the bearing capacity of a pile penetrating into the ground. This theory is one of the few elastic-plastic problems which can be solved analytically. Here the soil model is represented as a Mohr-Coulomb's elasto-plastic solid as shown in Figure 5.14, and a cylindrical cavity expansion is assumed. The problem is defined that the diameter of the soil cavity is firstly r_z, and then the diameter is expanded to R_z by applying external forces. Further, the distance of an elasto-plastic boundary from the center position, R_e, is set to be expanded with the displacement of the soil in an elastic zone, dU_e. Also, a distance from the center position is defined as r, and ψ is set to be a angle direction normal to r. Each stress component along r and ψ, σ_r and σ_ψ, is principal stress due to the symmetrical property of the cavity. Therefore, the relation between σ_r and σ_ψ in the elastic zone can be defined as the following failure criteria equation of soils.

$$\sigma_r - \sigma_\psi = (\sigma_r + \sigma_\psi)\sin\phi + 2C\cos\phi \tag{5.27}$$

where ϕ is internal friction angle and C is cohesion.

For the plastic and the elastic zones of the subsurface soil, the following equilibrium equations of the cylindrical stresses can be given by

· Plastic Zone:

$$\frac{\partial\sigma_r}{\partial r} + \frac{\sigma_r - \sigma_\psi}{r} = 0 \tag{5.28}$$

· Elastic Zone:

$$\sigma_r = C_1 + \frac{C_2}{r^2}\,, \quad \sigma_\psi = C_1 - \frac{C_2}{r^2} \tag{5.29}$$

where C_1 and C_2 are integration constants.

Given a boundary condition, the soil stress at $r = \infty$ is assumed to be a static soil pressure of an isotropic elastic medium, $\sigma_r = \sigma_\psi = K_0\gamma z$ (where K_0 is a coefficient of lateral soil pressure and γ is a soil bulk weight density). Therefore, $C_1 = K_0\gamma z$ can be determined. At the elastic-plastic boundary (*i.e.* $r = R_e$), $C_2 = R_e^2\,(K_0\gamma z\sin\phi + C\cos\phi)$ can be derived from Eqs. (5.27) and (5.29).

Accordingly, the soil stresses at the elastic zone can be rewritten as follows.

$$\sigma_r = K_0\gamma z + (K_0\gamma z + C\cot\phi\ )\sin\phi\left(\frac{R_e}{r}\right)^2 \tag{5.30}$$

$$\sigma_\psi = K_0\gamma z - (K_0\gamma z + C\cot\phi\ )\sin\phi\left(\frac{R_e}{r}\right)^2 \tag{5.31}$$

At the plastic zone, let the boundary condition be $\sigma_r = d\sigma + K_0\gamma Z$ at $r = R_p$. Equaling Eq. (5.27) to (5.28) at the elasto-plastic boundary, σ_r at $r = R_e$ can be represented by

$$\sigma_{R_e} = (d\sigma + K_0\gamma z + C\cot\phi)\left(\frac{R_p}{R_e}\right)^{\frac{2\sin\phi}{1+\sin\phi}} - C\cot\phi \tag{5.32}$$

where $d\sigma$ denotes the increase of the expanded soil stress.

Likewise, the stress σ_r at $r = R_e$ in Eq. (5.30) can be regarded as the same value with Eq. (5.32). Thus the increasing stress $d\sigma$ can be derived as follows.

$$d\sigma = (K_0\gamma z + C\cot\phi)(1+\sin\phi)\left(\frac{R_e}{R_p}\right)^{\frac{2\sin\phi}{1+\sin\phi}} - C\cot\phi - K_0\gamma z \tag{5.33}$$

Consequently, the ratio of R_p and R_e is needed for analyzing Eq. (5.33). To derive the ratio, a discussion of a soil's expanded volumetric balance can be effective. However, this research practically focuses on a cylindrical cavity. Therefore, the cavity is assumed to be an axisymmetric model, and here a cross section balance of soil is discussed as the volumetric balance. The total fluctuation of the cross section, U, can be defined as the sum of the fluctuation of the cross section in the plastic zone, U_p, and in the elastic zone, U_e, and U_p and U_e are assumed to change

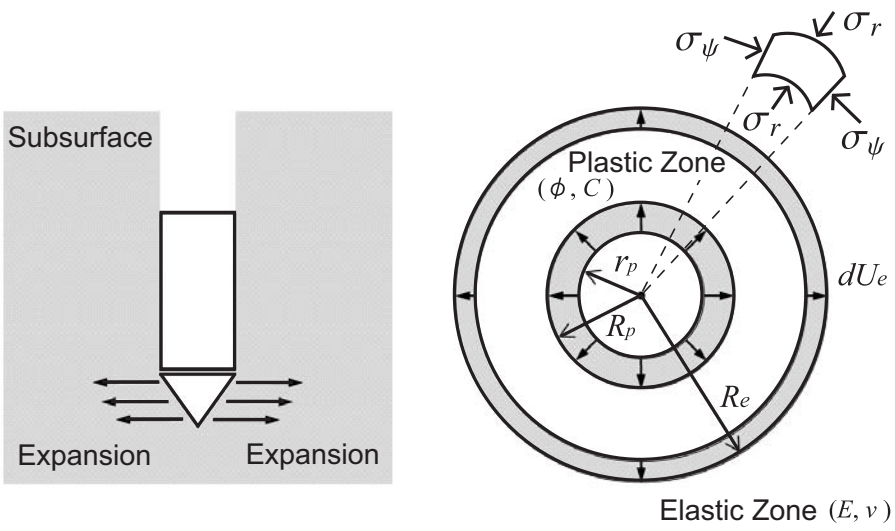

Figure 5.14 : Elasto-plastic soil model for applying a cylindrical cavity expansion.

independently. By reference to Figure 5.14, the balance can be expressed by

$$U = U_p + U_e \tag{5.34}$$

ans also,

$$U = R_p^2 - r_p^2 \tag{5.35}$$

$$U_p = \left(R_e^2 - R_p^2\right)\Delta \tag{5.36}$$

$$U_e = R_e^2 - (R_e - dU_e)^2 \tag{5.37}$$

$$dU_e = \frac{1+\nu}{E}\left(K_0\gamma z + C\cot\phi\right)\sin\phi R_e = C_3 R_e \tag{5.38}$$

where Δ is an average change ratio of expanding cross section in the plastic zone, ν is Poisson's ratio, E is Young's modulus. Displacement dU_e is provided by integrating the above Eq. (5.30), and here the volumetric force of soil is assumed to be neglected. Accordingly, the following equations can be derived by analyzing the volumetric balance.

$$r_p = R_p\left(\frac{r_c}{r_c+q}\right) = R_p\xi \tag{5.39}$$

$$q = \frac{v_z}{f}\tan\alpha_c \tag{5.40}$$

From the above definitions, ξ satisfies $\xi \leq 1$.

$$\frac{R_e}{R_p} = \left(\frac{1+\Delta-\xi^2}{1+\Delta-(C_3-1)^2}\right)^{\frac{1}{2}} \tag{5.41}$$

Here Eq. (5.41) must satisfy the following conditional equation derived by the inequality constraint $R_e > R_p$, which intends the existence of a plastic zone.

$$0 \leq \xi(\theta) < |C_3 - 1| \leq 1 \tag{5.42}$$

Based on the remarks as described above, $\sigma_1(z)$ including the cavity expansion effect can be estimated as follows.

$$\begin{aligned}\sigma_1(z) &= d\sigma + K_0\gamma z \\ &= \left(K_0\gamma z + C\cot\phi\right)\left(1+\sin\phi\right)\left[\frac{1+\Delta-\xi^2}{1+\Delta-(C_3-1)^2}\right]^{\frac{\sin\phi}{1+\sin\phi}} - C\cot\phi\end{aligned} \tag{5.43}$$

Furthermore, both $\sigma_2(z)$ at $r = r_{sc}(\theta + 2\pi)$ and $\sigma_3(z)$ at $r = r_s$ can be computed by stresses in a plastic zone as the following equation.

$$\begin{bmatrix} \sigma_2(z) \\ \sigma_3(z) \end{bmatrix} = (d\sigma + K_0\gamma z + C\cot\phi) \begin{bmatrix} \left(\frac{r_0}{R}\right)^{\frac{2\sin\phi}{1+\sin\phi}} \\ \left(\frac{r_0}{R_0}\right)^{\frac{2\sin\phi}{1+\sin\phi}} \end{bmatrix} - C\cot\phi \tag{5.44}$$

5.5.3 Parametric Analysis

To discuss characteristics of the model, parametric analyses were conducted by numerical simulations. As simulated soil environment, quartz sand was assumed. The nominal property of the Lunarant was: $\phi = 33\,\mathrm{deg}$, $C = 0\,\mathrm{Pa}$, $\rho = 1523\,\mathrm{kg/m^3}$ ($\gamma = \rho g$), $K_0 = 0.5$, $\Delta = 0.03$, $\nu = 0.4$, $E = 1.0 \times 10^6\,\mathrm{Pa}$ and $\hat{\mu} = 0.5$. The nominal parameters were basically determined based on the reference data of quartz sand [106]. Further, screw geometric and kinematic parameters were determined based on the SSD: $L = 0.05\,\mathrm{m}$, $r_0 = 0.015\,\mathrm{m}$, $R_0 = 0.025\,\mathrm{m}$, $\eta = 10\,\mathrm{deg}$, $\theta_{end} = 15\pi\,\mathrm{rad}$, $v_z = 0.002\,\mathrm{m/s}$, $f = 0.2\,\mathrm{rev/s}$, $k_H = 1$ and $h = 0.5\,\mathrm{m}$.

Figure 5.15 plots the simulation results. From Figure 5.15(a), a tendency of which M_T increases as the square of h was confirmed. On the other hand, Figure 5.15(b) indicated that M_T decreases with an increase of η. Increasing η, however, yields depression of the propulsive force. Thus proper design of the screw, meeting mission requirements, will become a significant factor. Additionally, Figures 5.15(c) and 5.15(d) depict the effects of the soil parameters on M_T. According to these graphs, C and Δ greatly influence M_T, while ϕ and $(1+\nu)/E$ have a relatively small effect on M_T. In particular, Δ is the most influential parameter but is a difficult parameter to be identified. Therefore, in actual unmanned missions, it will be a valuable technique to ensure the screw's performance under estimated parameter range.

5.6 Experimental Evaluation

5.6.1 Experimental Methodology

The drilling experiment of the SSD has been conducted to compare with simulation result. The experimental overview is shown in Figure 5.16 The target soil is quartz sand (no.5), fly ash and the Lunarant. The Lunarant is is one of lunar soil simulant and consists of fine particles and is produced by WEL RESEARCH Co., Ltd. [110]. The property of the test soils are shown in Figure 5.17 and Table 5.6. The starting situation is that the screw is completely buried and the

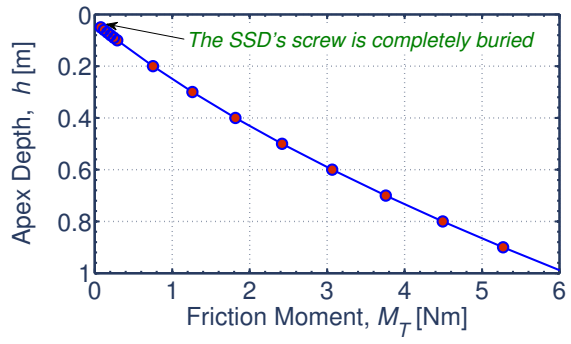

(a) Relation between M_T and h.

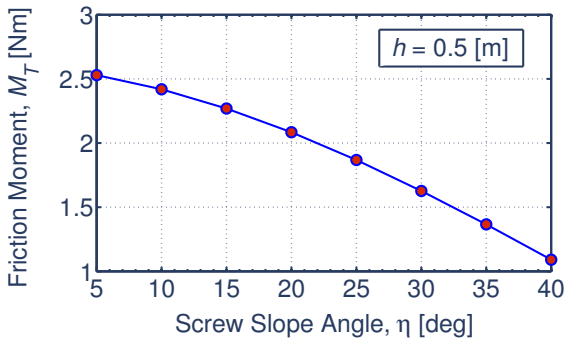

(b) Relation between M_T and η.

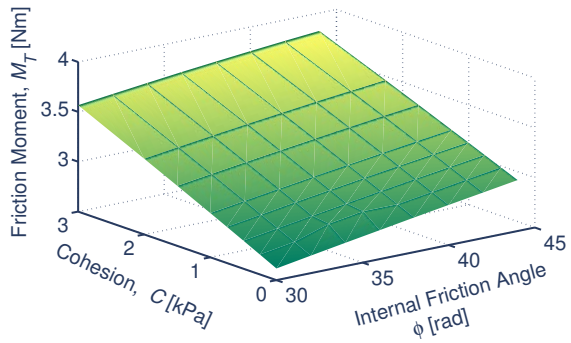

(c) Relation between M_T, ϕ and C.

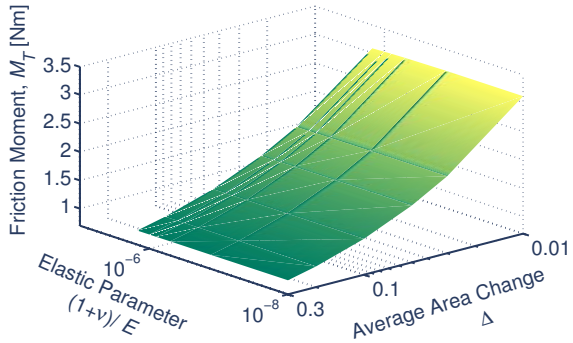

(d) Relation between M_T, $(1+\nu)/E$ and Δ.

Figure 5.15 : Simulation results of parametric analysis.

body stands out on the soil surface, and the external propulsive force comes from just its weight. Constant voltage was supplied to the motor during the experiments. Through the experiments, the rotation speed and the current of the DC motor are acquired by a current sensor (DCT-10; Multi Measuring Instruments Co., Ltd.) by DS1103 PPC Controller Board produced by dSPACE GmbH. The obtained screw rotational speed was almost constant, and therefore, the rotational speed did not need to be controlled in this system. Moreover, to measure the penetration speed, the driving motion during the experiments are taken as movies by a camera.

Furthermore, the typical physical conditions of targeting soil are assumed to be constant. In general, soil parameters are changeful and therefore it is too difficult to compute them correctly with respect to each depth. Meanwhile, it is only necessary to prove its reliable performance in unknown environments for the development of a reliable subsurface explorer because the important factor is the estimation of the most difficult situation such as the maximum frictional resistance in a goal depth. Thus, this dissertation assumes constant parameters of the targeting soils, as shown in Table 5.6, in numerical simulations based on the nominal data.

Figure 5.16 : Experimental overview.

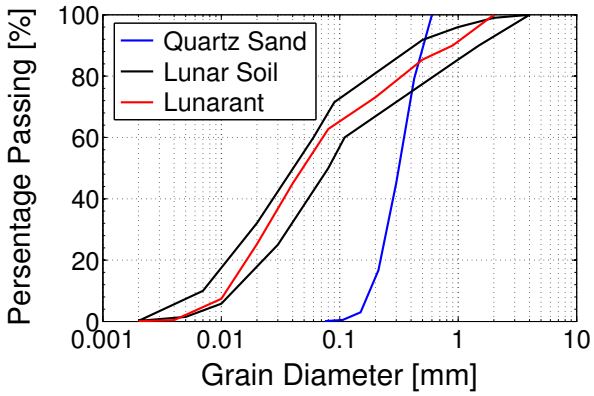

Figure 5.17 : Grain size accumulation curves of test soils.

5.6.2 Results and Discussions

Figure 5.18 shows the experimental result and the simulation plots. The simulation results indicated the similar tendencies with the experimental data, and then the validation of the proposed interaction model was confirmed. Consequently, by using the proposed model, the unknown resistances can be calculated and the geometric optimization can be also discussed.

Of particular note of the analysis targeting the Lunarant that the simulation plots did not match the experimental at shallow depth. This would be attributed to the wider particle size distribution of the Lunarant. That is because the wide distribution produces a soil bulk density difference between shallow and deeper zones. Therefore, the unknown parameter Δ should be set to be a larger value under a low density zone in accordance with Figure 5.18(c). On the other hand, fly ash has also a wide particle size distribution. Despite the wide distribution, the simulation plot met the experimental result targeting fly ash as shown in Figure 5.18(b). This is caused by a

Table 5.6 : Physical properties of test soils [104, 106, 110, 111].

Soil Parameter	Symbol	Unit	Value		
			Quartz Sand	Fly Ash	Lunarant
Internal Friction Angle	ϕ	deg	33	32	41
Cohesion Stress	C	Pa	0	0	0
Average Soil Bulk Density	ρ	kg/m^3	1523	1232	1512
Soil Pressure Coefficient	K_0	-	0.5	0.5	0.5
Average Volume Change	Δ	-	0.03	0.03	0.03
Poisson Ratio	ν	-	0.4	0.4	0.4
Young's Modulus	E	Pa	1.0×10^7	1.0×10^7	1.0×10^7
Friction Coefficient	$\hat{\mu}$	-	0.5	0.6	0.6

density difference as well. Unlike the Lunarant, fly ash was loosely-compacted in the experiments. As a result, effects of depth in fly ash and the Lunarant differed each other. The density variations of unknown terrains is an important factor to quantitatively calculate and predict the frictional moment.

Furthermore, the maximum penetrating depth was just 85 millimeters due to the effect of its body part in the experiment using the SSD prototype. Thus the soil discharging mechanism after a robot is required for developing the whole system of the subsurface robotic explorer in an unknown environment.

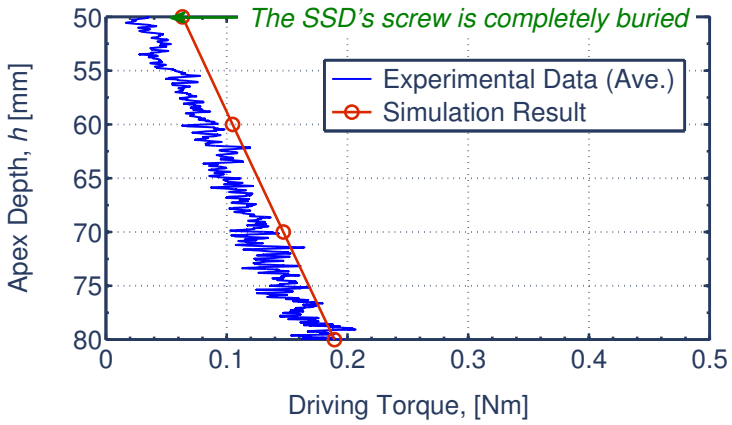

(a) Quartz sand.

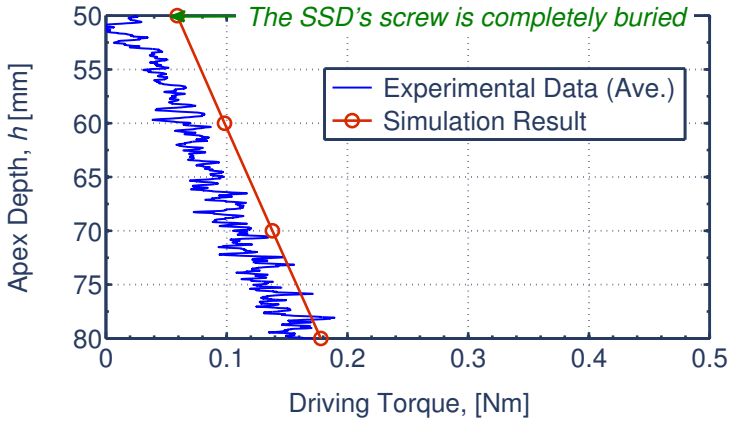

(b) Fly ash.

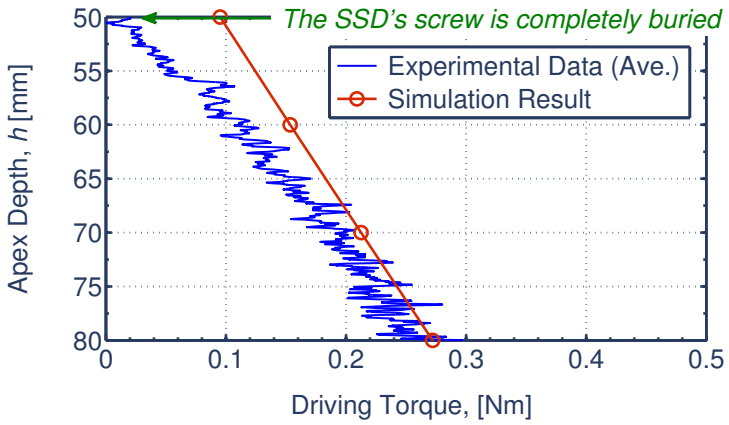

(c) Lunarant.

Figure 5.18 : Comparison of simulation result with experimental data.

5.7 Summary

Firstly, this chapter presented the requirements and the locomotion strategy for a subsurface robotic explorer on the Moon. Then a novel soil-screw interaction model for the subsurface locomotion was proposed. The characteristics of the developed model were evaluated by parametric analyses. These analyses indicated the influence of various parameters on the frictional moment. As a result, key parameters could be determined for the subsurface locomotion. The main contributions of this chapter is the derivation of the screw's dynamics model based upon soil mechanics with the cavity expansion theory. Such detailed model is unprecedented and provides crucial ideas adaptable to general screw mechanism. Also, the theoretical approach enables to optimize the geometric design of the screw. This will be a significant guideline for space applications, targeting unknown environment.

Chapter 6. Proposal of Effective Screw Drilling Mechanism

Available power resources and machines are strictly limited for space missions. Therefore, an effective screw drilling mechanism is required for lunar and planetary subsurface explorations in order to reduce the power consumption. Based upon the previous discussions, the validation of the screw drilling mechanism has been widely known. However, an attempt to development of a more efficient screw drilling mechanism has been rarely studied. In this chapter, mechanical improvement of the screw drill is newly discussed in order to achieve efficient self-drilling. The validity of the new mechanism is also evaluated by experimental analyses. Furthermore, the self-propelled subsurface explorer employing the effective screw drilling mechanism, which can burrow into the soil by itself, is proposed. Feasibility of the proposed subsurface explorer is analyzed by experimental and theoretical discussions. Likewise, the adequacy of the mathematical models developed in the Chapter 2 is examined by comparing the experimental data.

6.1 Proposal of Non-Reaction Screw Mechanism: CSD

The body reaction of a single spinning drill is a serious issue for normal operation. The reaction disturbs the rotation of the drill, and consequently, reduces drilling efficiency. Thus, this research has proposed a novel screw drill unit using a reaction-less structure. The concept of a double rotation mechanisms already exists on Earth as typified by a separated doughnut-auger method [25]. This method utilizes two rotating parts, an inner-screw and an outer-casing of a bearing pile which are driven independently by motors. However, the mechanisms for reaction reduction and the factors determined by past empirical rules have not been extensively studied as yet. Driving by two motors is able to achieve the redundant of the reaction against the body in principle. Additionally, to decompress the regolith is significant and effective for removing the lunar compacted regolith. Based upon these considerations, a novel no-reaction screw mechanism coupled with a soil agitation mechanism has been developed. Here various drilling mechanisms using the double rotation can be generally expected. On the basis of that considera-

tions, CSD (Contra-rotor Screw Drill) mechanism has been proposed as shown in Figure 6.1, has a drilling unit which has the contra-rotation axis coincident with the rotation axis for the novel drilling mechanism. Concepts of such double rotation mechanism have been considered in a boring machine [156] or a robotic endoscope [59, 60]. However, practical study on the drilling robot in ground has not been discussed. So this work is expected to contribute to the contra-rotor screw mechanism for drilling the soil.

The proposed CSD mechanism can be compact in size and is expected to achieve a higher drilling performance. Figure 6.1 shows the schematic model, the prototype and the prospective screw functions of the CSD. The CSD prototype has two DC geared motor (SCR-16-2512 and IG-16V-1/560; CITIZEN SAYAMA Co., Ltd.) with an encoder (MR-16-P/R128; CITIZEN SAYAMA Co., Ltd.). The motor for driving the front and the rear screw is attached by spur gears with reduction ratio 8/15 and 2/1, respectively. Referring to Figure 6.1(b), the prototype consists of a body, a front screw and a rear screw. The two screws can be driven independently by separate DC motors, allowing us to analyze the behavior of the screw under various driving conditions. The non-reaction mode can also be achieved using two motors. The length of the front and the rear screw are both set to be $L/2$. The front screw's maximum diameter is $D/2$ and the rear screw's is D. Here η is defined as the equivalent screw inclination angle of the front and rear screw along the central position on the screw flight surfaces, and the ratio between the moments of inertia of the front and the rear screw are determined approximately as $1/17.8$ after the geometric analysis of the prototype. In the subsequent subsections, some evaluation parameters for the experiments are described.

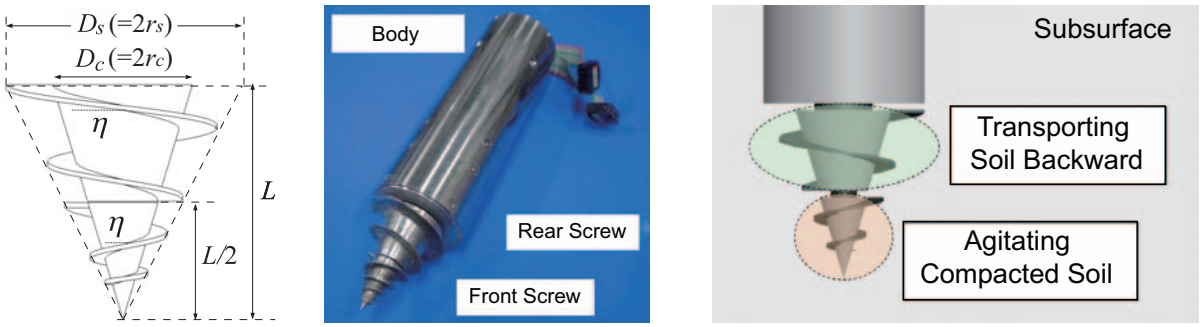

(a) Geometric model. (b) Prototype. (c) Prospective functions of the screws.

Figure 6.1 : Contra-rotor screw unit: CSD.

6.2 Evaluation Indexes for Experimental Analysis

6.2.1 Drilling Performance

The propulsive force caused by screw rotation force should be discussed first but it is hard to model mathematically. Therefore, this research first applies a parameter index representing a general rotational drilling performance based on kinematic drilling motion. The *Specific Energy*, *SE*, is a principal index of drilling performance based on the kinematic drilling states. Its concept was proposed by Teale [17] for assessing rock drillability. In this research, the penetrating property of the prototypes is evaluated first using this index. As the first step, the required input energy per minute for drilling or removing fore-soils, E_{SE} [MJ/min], can be written by

$$E_{SE} = W_{SE} \times \pi D_{SE} \times f \times 10^{-9} \tag{6.1}$$

$$W_{SE} = m_r \times g + F_{ex} \tag{6.2}$$

where D_{SE} [mm] is a diameter of drilling borehole, f [rpm] is a screw rotational speed, W_{SE} [N] is a weight for advancing, m_r [kg] is a total mass of an entire drilling system, g [m/s^2] is a gravitational acceleration and F_{ex} [N] is external forces unrelated to the interaction between the screw and soil such as an insertion force from a rover on surface. Here the interactive penetrating force is negligible since the required energy E_{SE} can be evaluated as an external input to the system.

By using a penetration speed PR [m/hr], a volume of soils removed per minute, V_{SE} [m^3/min], can be calculated as shown below [20].

$$V_{SE} = \pi \times \left(\frac{D_{SE} \times 10^{-3}}{2}\right)^2 \times \frac{PR}{60} \tag{6.3}$$

Thus SE [MJ/m^3] can be obtained by dividing E_{SE} by V_{SE} as follows.

$$SE = \frac{E_{SE}}{V_{SE}} = \frac{0.24 \cdot f}{D_{SE} \cdot PR} \cdot (m_r g + F_{ex}) \tag{6.4}$$

From Eq. (6.4), an increase in the SE denotes its drilling performance becomes lower. In the subsequent experimental analyses, F_{ex} is set to be zero and thus W_{SE} becomes $m_r g$.

Further, this research secondly introduces the mechanical specific energy, called *MSE*, into the experimental analyses regarding the additional comparison of the CSD with the SSD. *MSE* indicates the drilling efficiency of system [27, 33]. In this dissertation, *MSE* enables the CSD and the SSD to be evaluated with their rotary torques and based on the advanced *MSE* [26] expanded from the Teale's definition [17], the *MSE* [MJ/m^3] used for our experiments can be eventually defined as follows.

$$MSE = \eta_M \left[\frac{W_{SE}}{\pi (D_{SE}/2)^2} + \frac{120 f T_{MSE}}{(D_{SE}/2)^2 PR}\right] \tag{6.5}$$

where η_M is a mechanical efficiency defined as the ratio of an output power over an input power, and T_{MSE} [Nm] is a driving torque. For the developed prototypes, η_M can be given a common value because the same gearing mechanism is adopted for the CSD's screws and the SSD's screw. Therefore, *MSE* can be actually evaluated by a function of MSE/η_M. In fundamental experiments, *MSE* based on the energy efficiency can be quantified by driving torques in addition to the measuring values needed for computing *SE*.

6.2.2 Equivalent Angular Velocity and Rotational Ratio

For applying Eq. (6.4) to the CSD unit, an equivalent angular velocity of the CSD is needed. By equating the rotating energies of the drilling parts, an equivalent angular velocity ω_s [rad/s] is defined. Here, when the body's rotational angular velocity can be assumed to be zero, and then the total rotational energy can be given as shown below.

$$\frac{1}{2}I_1\omega_1^2 + \frac{1}{2}I_2\omega_2^2 = \frac{1}{2}I\omega_s^2 \tag{6.6}$$

where I_1 [kgm^2] is the moment of inertia of the front screw, I_2 [kgm^2] is the moment of inertia of the rear screw, ω_1 [rad/s] is the angular velocity of the front screw and ω_2 [rad/s] is the angular velocity of the rear screw, and I is the equivalent moment of inertia of the CSD's overall screw and is assumed to be equal to $I_1 + I_2$. Hence, ω_s can be derived as the following equation.

$$\omega_s = \sqrt{\frac{I_1\omega_1^2 + I_2\omega_2^2}{I_1 + I_2}} \tag{6.7}$$

Through the experiments, ω_s is converted to f_s ($= 30\omega_s/\pi$ [rpm]) in order to utilize the above evaluation indexes, and also ω_1 and ω_2 can be converted to f_1 [rpm] and f_2 [rpm] respectively.

Additionally, the rotational ratio is defined as the following expression which provides the ratio of the angular velocities or the rotational speeds.

$$K_\omega = \frac{\omega_1}{\omega_2} = \frac{f_1}{f_2} \tag{6.8}$$

6.3 Experimental Analyses

6.3.1 Overview

Several experiments with the SSD and the CSD were carried out. Figure 6.2 shows an experimental overview. In the experiments, the target soil was initially set to be quartz sand and was

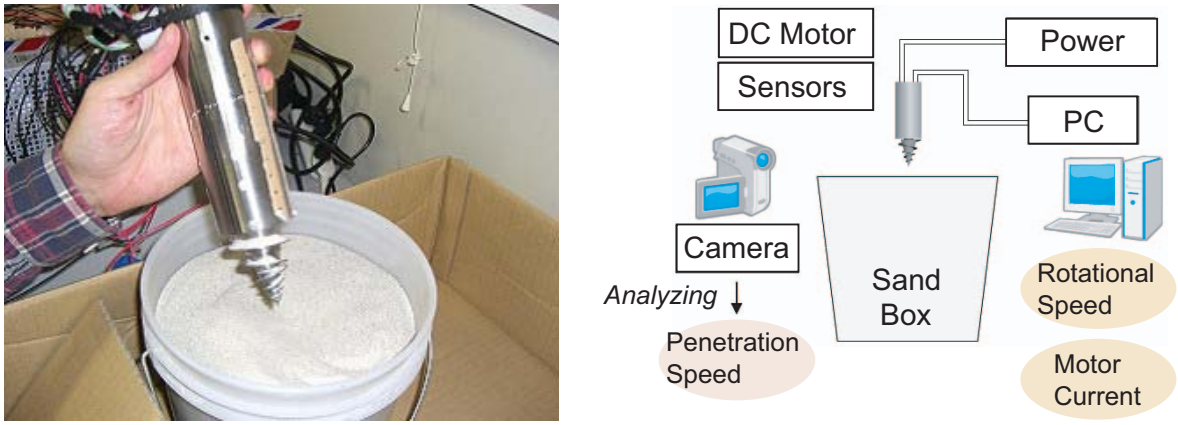

(a) Overview. (b) System configuration.

Figure 6.2 : Experimental environment.

Table 6.1 : Specifications of the screw prototypes.

	L [m]	D_s [m]	D_c [m]	Mass [g]	η [deg]	Screw's Winding Form
SSD	0.05	0.05	0.03	356∼604	10.0	dextral (single)
CSD	0.05	0.05	0.03	604	10.0	dextral (rear) & sinistral (front)

then replaced by a kind of lunar regolith simulant, Lunarant, was used. The grain size distribution and the physical property of the Lunarant matches that of the lunar regolith obtained in the past glorious missions [3]. The experimental conditions of the target soils, quartz sand and the Lunarant, are shown in Figure 5.17 and Table 5.6. Next, Table 6.1 describes the specifications of the prototypes. The prototypes were powered through a tether connected to a stabilized power source. Here the front screw and the rear screw of the CSD can be independently controlled by two DC motors inside the body. The starting position was set so that the screw part was completely buried in the soil in the box, the body standing out on the surface. W came only from the weight $m_r g$. Two driving states were tested during the experiments conducted with the CSD in quartz sand. The first one corresponded to a free moving body and the other was a fixed body where the reaction was canceled by hand in order to evaluate the drilling performance according to the prototype geometry. Throughout the experiment the rotational speed were acquired by encoders to the PC. The entire driving period of the experiments was also measured by monitoring the data series input into the DS1103 PPC Controller Board. A constant input voltage was independently supplied to the all driving motors. The experiment was filmed and the video was used to compute the average penetration speed of both the SSD and the CSD.

6.3.2 Verification of Penetration with Non-Reaction

When the SSD was driven, only the body rotated while the screw remained in place due to the frictional resistance of the soil against the screw. Consequently, downward motion was not achieved. In contrast, a reduction of the body rotation was verified experimentally for the CSD with two motors. Its ideal non-reaction condition was measured to be approximately $K_\omega = 62.5$. This ideal condition can be changed by modifying the geometric design of the screws. Figure 6.3 shows the experimental views of different reaction modes. Furthermore, a slight wobbling motion of the body was observed even near the non-reaction condition. This phenomenon could be caused by the connecting cords, off-balance masses and/or the skew symmetry of the screws. Nevertheless, the wobbling effect may still be considered negligible, especially when a robot reaches deeper areas beneath the surface.

6.3.3 Performance Evaluation Based on Kinetic Driving States

Figures 6.4, 6.5 and 6.6 show the experimental results of the CSD targeting quartz sand and the Lunarant. Referring to Figures 6.4(a) and 6.5(a), at the non-reaction range, the *PR* and *SE* under the body is free indicates same values with them under the body is fixed, respectively. In particular, at around $K_\omega = 1 \sim 5$, the CSD can perform better than the SSD as shown in Figure 6.5(a). And also, Figure 6.6(a) indicates *PR* of the CSD depends much on the rear

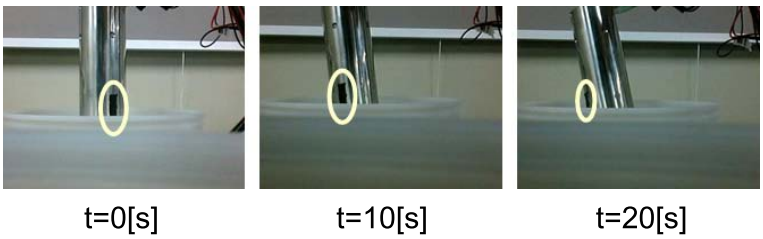

(a) Stronger reaction mode: $K_\omega \simeq 18.8$.

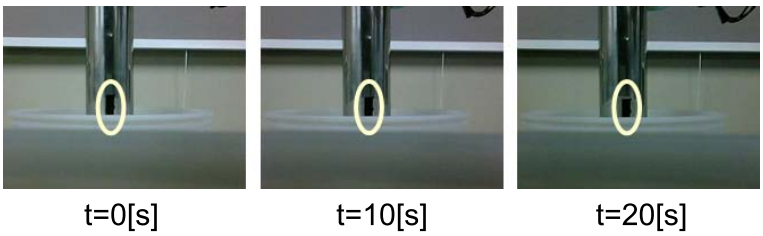

(b) Non-reaction mode: $K_\omega \simeq 62.5$.

Figure 6.3 : Experimental view of the reaction modes targeting quartz sand.

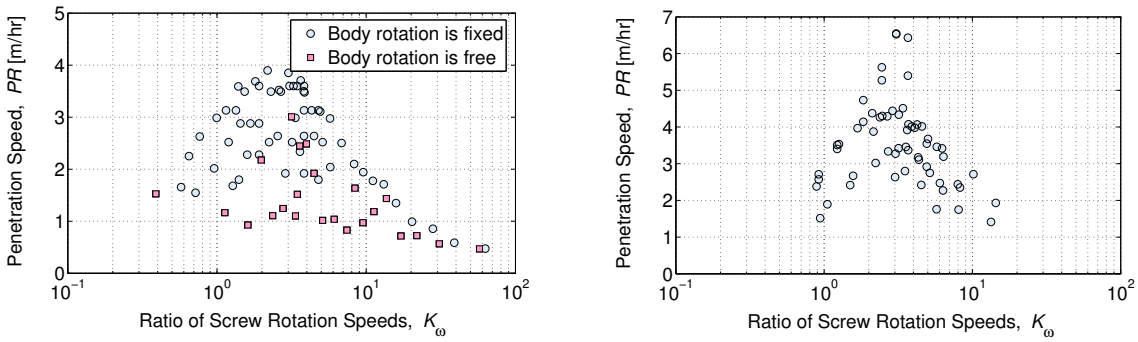

(a) Targeting quartz sand. (b) Targeting Lunarant under the body is fixed.

Figure 6.4 : Experimental results of CSD: Relation between PR and K_ω.

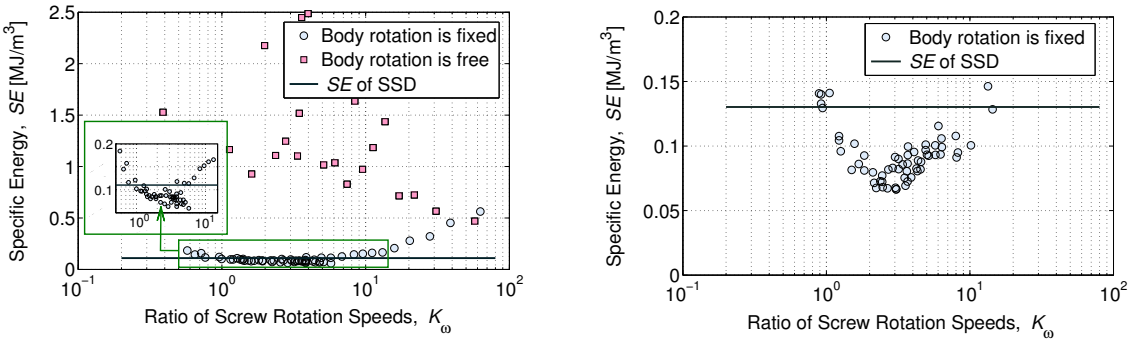

(a) Targeting quartz sand. (b) Targeting Lunarant under the body is fixed.

Figure 6.5 : Experimental results of CSD: Relation between SE and K_ω.

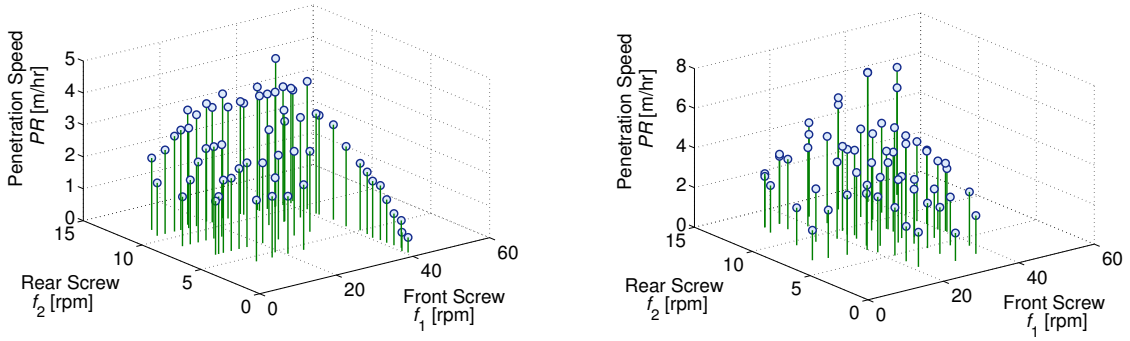

(a) Targeting quartz sand. (b) Targeting Lunarant under the body is fixed.

Figure 6.6 : Experimental results of CSD: Relation between PR, f_1 and f_2.

rotational speed f_2. On the other hand, the boundary which PR dwindles rapidly is verified with decrease of the front speed f_1. This remark implies that there is a certain condition regarding K_ω for achieving the appropriate drilling. Its tendency can be expressed in Figures 6.5(a) and 6.6(a). The appropriate condition can be estimated as $K_\omega = 2$ in the experiments of the CSD

targeting quartz sand.

The experimental results using the Lunarant are shown in Figures 6.4(b), 6.5(b) and 6.6(b). According to Figure 6.5(b), the CSD can indicate a appropriate performance at around $K_\omega = 1 \sim 10$ better than the SSD, and the highest *SE* is almost same with it using quartz sand but the maximum *PR* becomes obviously larger. This result is caused by the higher frictional and compressive proprieties of the Lunarant, and it can thus be estimated that larger amounts of soils affect its penetration. By analyzing these data, it is resulted that the appropriate K_ω appears in the similar range of it targeting quartz sand, however, Figure 6.6(b) indicates that the appropriate K_ω actually varies around $K_\omega = 3$ in the input conditions.

6.3.4 Performance Evaluation Based on Dynamic Inputs

The next consideration to be discussed is the intercomparison of each driving torque calculated by the motor current. Here the experimental results with the Lunarant are detailed. The characteristic of the SSD's driving torques is plotted in Figure 6.7. The obtained data shows the driving torques depends on the rotational speed and the penetration depth as typical tendencies. Next, Figure 6.8 shows the driving torques of the CSD in various rotational speeds. From these results, the driving torque of the front screw becomes much smaller than that of the rear. Additionally, the driving torques of the CSD would increase with enlarging the rotational speeds and the depth as well as them of the SSD. The comparison of the SSD and CSD under the same weight, rotation speed and depth of 65 millimeters is depicted in Figure 6.9. The driving torque of the CSD is nearly twice that of the SSD.

Figure 6.10 depicts the *MSE* of the CSD at the same depth, which is 65 millimeters below the surface. Here $\eta_M = 0.5$ is set constantly as the common mechanical efficiency of the CSD and the SSD since their structural configurations are same. In accordance with Figure 6.10, the appropriate condition of the CSD prototype can be confirmed at around $K_\omega = 3$. This remark indicates a similar tendency with the analyses by the *SE* and supports the appropriate condition deduced by the comparison of each *SE*. By calculating the experimental result of the SSD, the *MSE* of the SSD which has the equivalent weight under $\eta_M = 0.5$ can be also obtained. The SSD's value is 0.496MJ/m^3 and is determinately worse than that of the CSD's values in Figure 6.10. Therefore, the experimental analyses evaluated by the *MSE* and the *SE* can conclude that the appropriate driving condition of the CSD is estimated to exist around $K_\omega = 3$ for penetrating into the Lunarant layer.

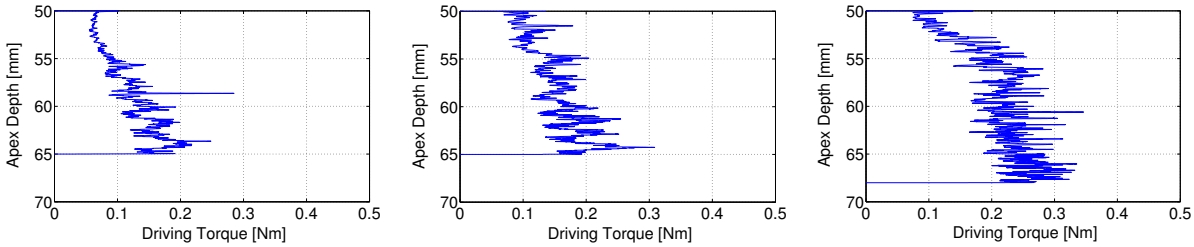

(a) $f = 9.2\,\text{rpm}$. (b) $f = 11.5\,\text{rpm}$. (c) $f = 13.8\,\text{rpm}$.

Figure 6.7 : SSD's driving torques with the various screw's rotational speed.

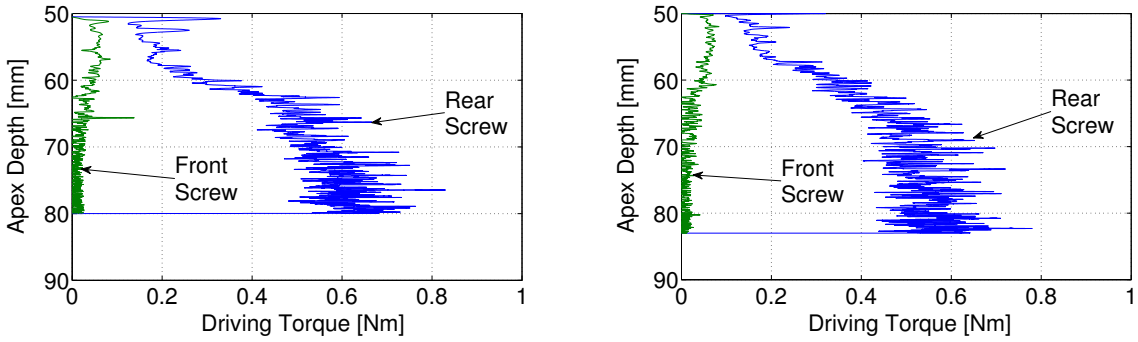

(a) $f_1 = 46.7\,\text{rpm}$ ($K_\omega = 3.67$). (b) $f_1 = 38.9\,\text{rpm}$ ($K_\omega = 3.06$).

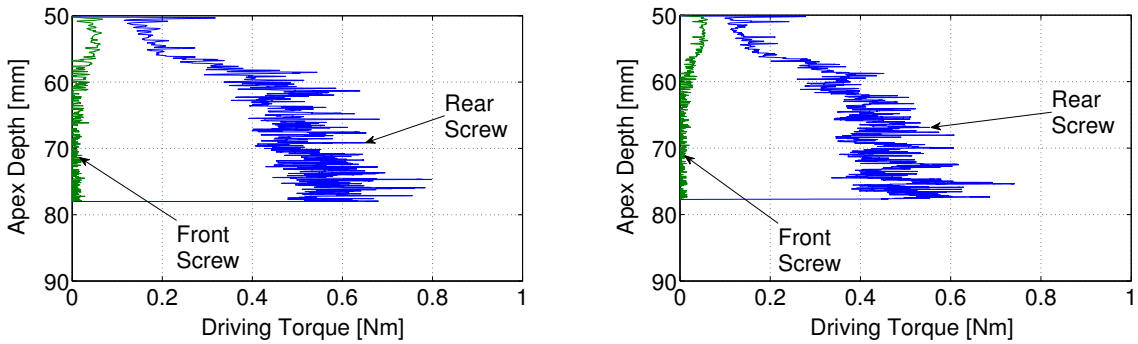

(c) $f_1 = 31.1\,\text{rpm}$ ($K_\omega = 2.45$). (d) $f_1 = 23.4\,\text{rpm}$ ($K_\omega = 1.84$).

Figure 6.8 : CSD's driving torques with the various f_1 under $f_2 = 12.7\,\text{rpm}$.

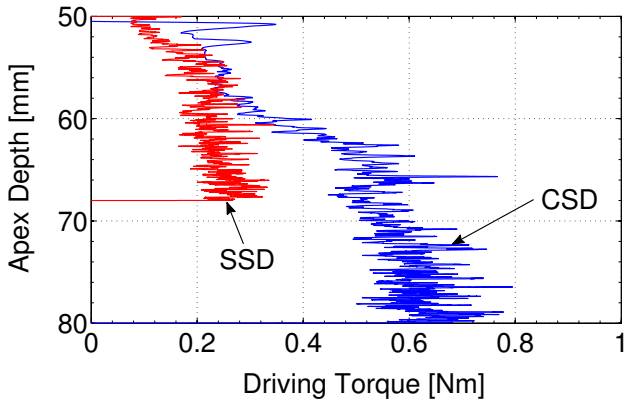

Figure 6.9 : Comparative data of the driving torques of SSD and CSD with maximum inputs.

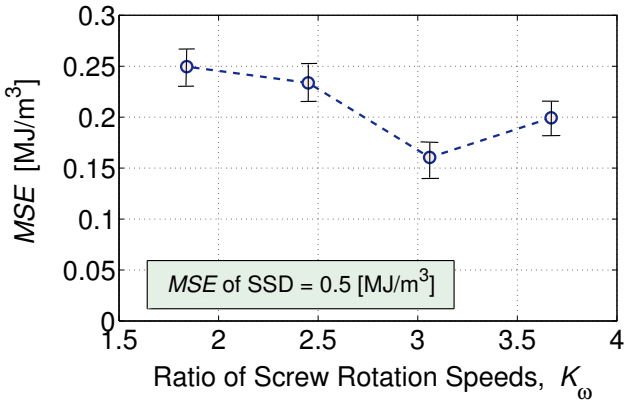

Figure 6.10 : Experimental analysis results of CSD at 65mm depth: Relation of MSE and K_ω ($\eta_M = 0.50$, $W = 5.925$ N and $f_2 = 12.7$ rpm).

6.4 Proposal of Screw Subsurface Explorer

Synopsis of Screw Subsurface Explorer System

On the basis of the previous discussions, this research proposes a novel screw subsurface explorer. Mechanical design of the proposed screw subsurface explorer is shown in Figure 6.11. The explorer consists of an internal body and a front and a rear drilling screws, and the body is inside the rear screw. The front one is a logarithmic helix while the rear one includes a logarithmic and a cylindrical helix.

Figure 6.12 shows the schematic of its prototype. For experimental analyses, its specifications are indicated in Table 6.2. The prototype has two DC micromotors (2642W-024CR; FAULHABER Miniature Drive Systems) with planetary gear head (30/1-159:1; FAULHABER Miniature Drive Systems) and magnetic encoders (IE2-512; FAULHABER Miniature Drive Sys-

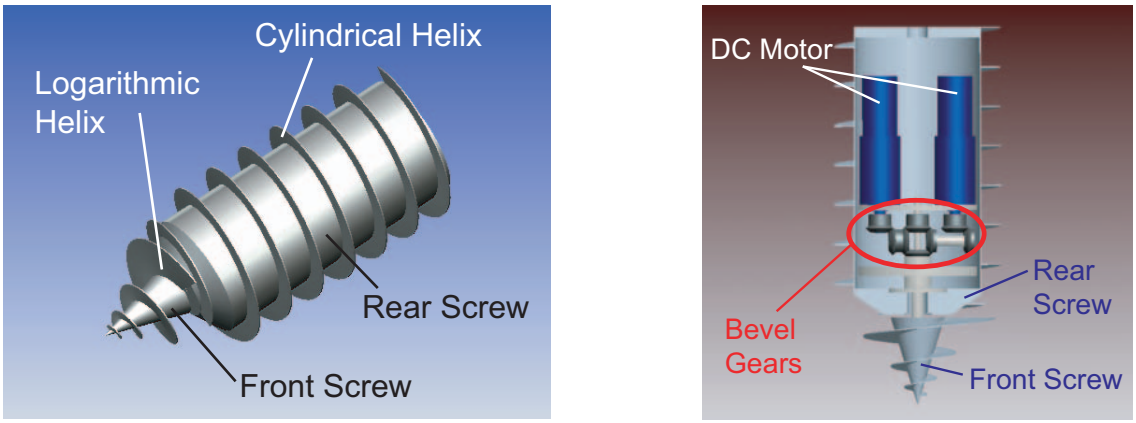

(a) 3D CAD model. (b) Schematic of internal structure.

Figure 6.11 : Mechanical design of screw subsurface explorer.

tems). For driving the front and the rear screw, the motors are attached by differential gears with reduction ratio 1/4. Further, the motor currents can be measured by external current sensors (HPS-3-AS; U.R.D. Co., Ltd.). The two motors inside the body for driving the screws, and so that reaction torques of the motors were canceling each another. The motor currents and rotation speeds were measured by embedded sensors, and their data was taken in the DS1103 PPC Controller Board. The target soil was fly ash which has very fine particles similar to the lunar soils. In addition, the prototype is powered by a stabilized power source with cables. The constant input voltages are given to the driving motors, while to calculate the penetration speed, a movie of the driving motion was taken by a camera.

Experimental Discussion with Theoretical Simulation

In the experimentation, the prototype achieved a certain level of subsurface access as shown in Figure 6.13. However, it stopped driving at 120 millimeters in depth due to a structural issue with the inner gears. Figure 6.14 plots the experimental result and the numerical simulation plots of the proposed dynamics model. Here each soil parameter was basically determined by the reference data of fly ash in the simulation as shown in Table 5.6. Likewise, the geometric and the kinematic parameters are determined based on the experiments performed by the prototype, and the rotation speeds and the penetration speed were given by the experimental result. In Figure 6.14, the simulation analysis is in agreement with the experimental result especially in the deeper area, and this validates the model.

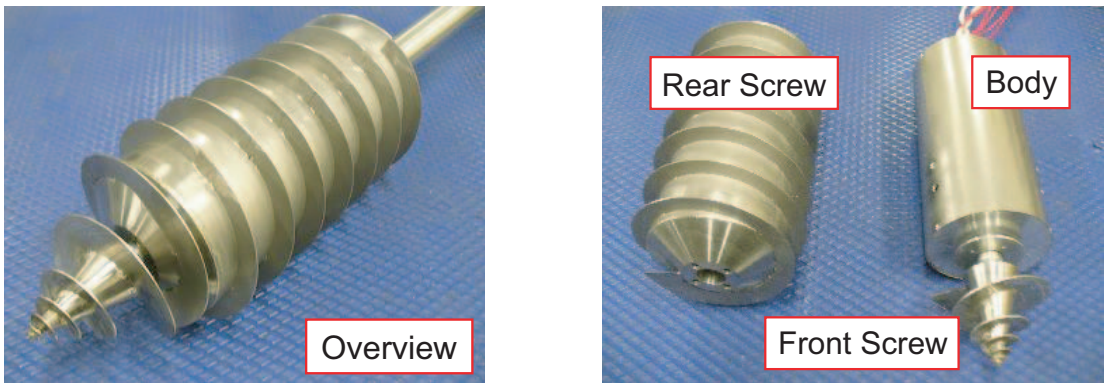

Figure 6.12 : Prototype of robotic screw explorer.

Table 6.2 : Fundamental specifications of the prototype.

	Length [mm]	Max. Diameter [mm]	Weight [kg]	α_{sc} [deg]
Front Screw	65	95	-	10
Rear Screw	225 (15+210)	124	-	5
Total	290	124	3.87	-

(a) Before driving.

(b) During experiment.

(c) After experiment.

Figure 6.13 : Photographs of drilling experiment by subsurface screw explorer.

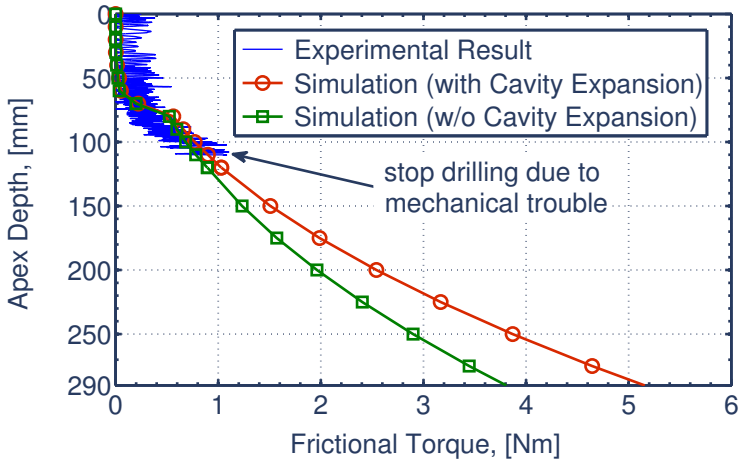

Figure 6.14 : Experimental result with simulation plots.

6.5 Simulation Case Study: A Guideline for Design

It is significant how the model is applied to practical systems. The theoretical model provides a rational design guideline of a screw drilling system. In this section, a design guideline of the screw subsurface explorer are here discussed as a case study. Given some mission requirements, the guideline for the design is provided by simulation analyses.

As a first step, the following mission requirements are assumed to be given:

- The screw subsurface explorer is comprised of front and rear screws.
- The front screw is logarithmic helix and the rear is cylindrical one, and the screw slope angles of the front and the rear screws are set to be same.
- The length of the front screw is set to be 5 centimeters ($L = 0.05$), and the one of the rear screw is set to be 25 centimeters ($L = 0.25$), respectively.
- Maximum borehole diameter is set to be 100 centimeters ($R_0 = 0.05$).
- The diameter of the inner body is set to be 80 centimeters ($r_0 = 0.04$).
  (whence the maximum height of the screw flights is 10 centimeters)
- The targeted soil is set to be the Lunarant.
  (Referring to Table 5.6, the physical parameters of the Lunarant are determined)
- The assumed depth is set to be 1 meter below the surface ($h = 1.0$).

The next step is to calculate the frictional moment M_T at 1 meter in depth under a specific screw slope angle η. Computed values of M_T based on the proposed model are provided as shown in Table 6.3. According to this result, employed motors are selected. The required specification can be achieved by using DC motors and gear heads produced by Maxon Motor ag. For instance, a combination of RE25 (20 watt motor) and GP32C (planetary gear head) can be embedded inside the assumed body, and its maximum continuous torque is 96.8 Nm.

Table 6.3 : Simulation case study for design guideline.

η [deg]	M_T [Nm]
10	38.5
20	33.0
30	25.6
40	17.6

6.6 Summary

In the summary of these experimental analyses, the above results elaborate on the underlying properties of the CSD under various screw driving modes. Through the experimental analyses, the following remarks regarding the proposed screw drilling mechanism, CSD, are especially concluded as key notes:

- Penetration speed was be attributed to rotational speed and input power.
- Penetration speed depended greatly on the driving property of the rear screw.
  (because making a borehole for advancing is governed by the rear screw driving)
- The non-reaction condition was able to be achieved by two motors.
  (realization of efficient drilling)
- Appropriate drilling condition: Neighborhood of $K_\omega = 2$ for quartz sand and $K_\omega = 3$ for the Lunarant (lunar soil simulant).
  (it might be constrained by the relative ratio of the screw geometry and soil properties and the reason for the incidence of a constant appropriate condition is estimated to be the influence by transferring soil from the front screw to the rear one)

Furthermore, this research proposed and developed the screw subsurface explorer. The experimentation of the prototyped robot was carried out, and its result was discussed with the comparative analysis of the numerical simulation. Mechanical issues should be addressed in future works in order for the prototype to conduct more challenging experiments in a deeper subsurface. Model analysis in such conditions should also be conducted in order to enhance the reliability of the robotic explorer. In addition, the effect of the contra-rotor mechanism and the identification of indeterminate soil parameters need to be considered in the theoretical study.

This chapter also indicated the drilling experimental result of the screw subsurface explorer. The result was discussed with the simulations. From this, it was confirmed that the proposed model is feasible to estimate the frictional moment.

Chapter 7. Conclusions

7.1 Concluding Remarks

This research has addressed mainly the soil-screw interaction. This chapter summarizes this dissertation and the main resulting conclusions are described as follows.

Chapter 2: Archimedean Screw Mechanism

Chapter 2 introduced the mathematical definitions of the fundamental screw helices, especially the screw's geometric and kinematic parameters. Based upon the definitions, arbitrary helical shapes of logarithmic and cylindrical screws can be expressed in mathematical form. Then, possible advantages of the screw mechanism for applying to the surface and the subsurface locomotion were stated concisely. Additionally, Chapter 2 summarized related works of the screw applications, not only locomotion in soft terrain.

Chapter 3: Modeling of Screw Surface Locomotion

Chapter 3 elaborated the uncommon locomotion method using the Archimedean screw mechanism. At first, this chapter discussed advantages of the screw mechanism by comparison of conventional locomotion gears such as a wheel and a track. The Archimedean screw mechanism is expected to exert enough traction even it is buried into soil. Accordingly, it is robust to getting stuck in the soil in addition to its structural simplicity. In this dissertation, the Screw Dive Rover system driven by the Archimedean screw units was proposed as a new-typed rover specialized for traveling on the soil. Then, this chapter mainly addressed the soil-screw interaction modeling for the surface locomotion by the Archimedean screw unit. Two types of the model concepts were here considered. One was the interaction model based on the skin friction between the screw flights and the soil. Another was the model based on the terramechanic studies, which are able to cover the compression characteristics and the shear phenomena of soil. These models were evaluated by the simulation analyses. The skin friction model was very simple and it enabled

to easily control the movement. Its consistency with the empirical maneuvers, however, was incompatible in practice. Meanwhile, although the terramechanics-based model indicated preferable compatibility with the empirical maneuvers (as stated in Chapter 4), it became complicated. In particular, the terramechanics model was able to indicate a similar tendency resulted in experimental results (Chapter 4). Based upon these remarks, the new synthetic model was proposed by combining skin friction and terramechanics. The synthetic model can demonstrate more practical interaction, and provided a significant guideline for using the screw mechanism.

Chapter 4: Experimental Characteristics of Screw Surface Locomotion

Chapter 4 addressed the experimental analyses of the Archimedean screw unit for surface locomotion. In this chapter the experimental trafficability of the single screw unit and the experimental maneuverability of the Screw Drive Rover system were investigated by the indoor experiments. The trafficability and the maneuverability suggested how the interactive mechanics between the screw unit and the soil should work. Furthermore, the trafficability was quantitatively discussed by comparing with the simulations of the proposed model. From these analyses, the validity of the proposed model was indicated. In the maneuverability and the trafficability tests, quantitative and qualitative analyses were conducted. The experimental results also contributes to the interaction modeling process in Chapter 3.

Chapter 5: Modeling and Analysis of Screw Subsurface Locomotion

Chapter 5 investigated subsurface locomotion by the Archimedean screw mechanism. To advance in the soil, it was indicated for the subsurface explorer system to require an active force by computational prediction. Also, the subsurface locomotion strategy was qualitatively defined based on the past literature [163]. Through the theoretical discussion on feasibility analyses of the soil compaction for making a space, this research pointed out the importance of removing fore-soil backward. According to these considerations, effectiveness of the Archimedean screw was indicated. Following these remarks, this chapter introduced the novel soil-screw interaction model of the subsurface locomotion in the soil (drilling into the soil). The proposed model was analyzed by the parametric simulations, and then its characteristics were numerically examined. The model validation was also evaluated by the experimental result and the numerical simulation. This chapter

contributes to a novel concept of the soil-screw interaction for general applications of the screw structure in the soft terrain.

Chapter 6: Proposal of Effective Screw Drilling Mechanism

Chapter 6 proposed a new effective screw drilling mechanism, called CSD (Contra-rotor Screw Drilling) mechanism to achieve efficient screw drilling. This new mechanism aimed to agitate compacted subsurface soil. Also, the CSD mechanism was able to cancel the reaction torques of the two motors embedded in the body. This disabled the reacting body rotation, and normal screw rotations and self-propulsion could thus be achieved without any ground bases. The CSD was experimentally analyzed by using *SE* and *MSE* indexes. From the experimental analyses, it was confirmed that the CSD has the proper condition when the front screw's rotational speed is $2\sim3$ times greater than the rear one. Although the condition depends on soil types and the screw geometry, it is an interesting remark that a certain optimal condition exists. In addition, in this chapter a new subsurface explorer by using the Archimedean screw mechanism was proposed. The proposed explorer was designed to burrow into the soil by itself. The drilling experiment of the explorer was carried out, and then its result was examined by comparison with the developed model in the Chapter 5. From the experimentation, it was confirmed that the theoretical estimate moderately meets the experimental result. Finally, the simulation case study of the screw's design guideline was exampled.

7.2 Future Works

This research has several future works to be addressed.

With regard to the surface locomotion by the screw, the interaction model needs to newly consider boundary conditions at the ends of the screw units. Further to this, the model does not include an inclination of the screw units to terrain surface. Thus, as a future work, the model should be improved in order to discuss not only its stationary motion, but its dynamic motion. Also, A quantitative evaluation of the maneuverability remains to be an undiscussed subject. Practically, terrain conditions should be accurately controlled in order to validate quantitative maneuvers. In another viewpoint, path-following control will be needed to apply the Archimedean screw mechanism to exploration rovers. As mentioned before, the precise modeling of the soil-screw interaction is quite difficult due to terrain uncertainty or irregularity. Therefore, a qualitative control will be achieved but a quantitative control will not be realized

by just feedback control technique based on internal sensors. In practical rover missions, visual tracking or landmark tracking by cameras is a prospective approach. To follow the given path, autonomous/semi-autonomous trajectory modification must be conducted by sequential computation of error distance from desired path. By using the feedback control with visual information, the locomotion control will be achieved even in unknown surfaces. The establishment of such control scheme is one of the possible directions.

As for the subsurface locomotion by the screw, identifications of some soil parameters of the proposed model need to be examined, especially at deeper areas in soil layer. Actually, determination of the parameter ranges is enough for evaluating the model at the deep areas. In particular, it is only necessary to deal with the most stringent condition for drilling into the compacted regolith. As a result, selections of the most stringent parameters will be next challenges. To quantitatively evaluate details of the proposed models, each element in the models will be required to be measured by various sensors. Further to these future works, generalized concept of the proposed contra-rotor screw mechanism must be established to broaden the range of its application.

On the other hand, effects of gravity and vacuum environments are additional challenges to be addressed for both the surface and the subsurface locomotion. In fact, gravitational changes and vacuum levels will affect screw's performances. Enhancement of feasibility and reliability of the screw mechanism in harsh space environment should be ensured and is an important task to be discussed.

Appendix A Moving Direction Control based on Skin Friction Model

A.1 Control System

Define the state variable $\mathbf{q}$ to be the state matrix $\mathbf{q}=[X\ Y\ \delta\ \dot{X}\ \dot{Y}\ \dot{\delta}\ \theta_r\ \theta_l]^T \in \mathbb{R}^{8\times 1}$. Furthermore, the input variable $\mathbf{u}$ is the matrix $\mathbf{u}=[\omega_r\ \omega_l]^T \in \mathbb{R}^{2\times 1}$ and the moving resistance is also defined as $\mathbf{F_R} \in \mathbb{R}^{8\times 1}$. Based upon the afore-mentioned modeling of the Screw Drive Rover, its control system can be represented as follows.

$$\dot{\mathbf{q}} = \mathbf{A}\mathbf{q} + \tilde{\mathbf{T}}(\mathbf{B}(\mathbf{q})\mathbf{u} - \mathbf{F_R}) \tag{A.1}$$

where,

$$\tilde{\mathbf{T}} = \begin{bmatrix} \mathbf{T}^{-1} & \mathbf{O}_{3\times 5} \\ \mathbf{T}^{-1} & \mathbf{O}_{3\times 5} \\ \mathbf{O}_{2\times 6} & \mathbf{E}_{2\times 2} \end{bmatrix} \in \mathbb{R}^{8\times 8} \tag{A.2}$$

$$\mathbf{A} = \left[\begin{array}{ccc} \mathbf{O}_{3\times 3} & \mathbf{E}_{3\times 3} & \mathbf{O}_{3\times 2} \\ \hline & \mathbf{O}_{5\times 8} & \end{array}\right] \in \mathbb{R}^{8\times 8} \tag{A.3}$$

$$\mathbf{B}(\mathbf{q}) = \left[\begin{array}{cc} \mathbf{O}_{3\times 2} & \\ \hline B_1 & B_2 \\ B_3 & -B_4 \\ B_5 & B_6 \\ \hline \mathbf{E}_{2\times 2} & \end{array}\right] \in \mathbb{R}^{8\times 2} \tag{A.4}$$

$$\mathbf{F_R} = \begin{bmatrix} \mathbf{O}_{1\times 3} & \dfrac{F'_X}{M} & \dfrac{F'_Y}{M} & \dfrac{F'_\delta}{I} & \mathbf{O}_{1\times 2} \end{bmatrix}^T \tag{A.5}$$

and also,

$$B_1 = B_2 = \frac{\hat{\mu} m_r g (k_2 - 4\sin a)}{4 m_r \pi}$$

$$B_3 = B_4 = \frac{\hat{\mu} m_r g \cos a}{m_r \pi}$$

$$B_5 = \frac{\hat{\mu} m_r g}{4\pi I_r} \sum_{i=1}^{4} r_{ri} \cos(a - b_{ri})$$

$$B_6 = \frac{\hat{\mu} m_r g}{4\pi I_r} \sum_{i=1}^{4} r_{li} \cos(a - b_{li})$$

$$F'_X = C_X F_X,\ F'_Y = C_Y F_Y,\ F'_\delta = C_\delta F_\delta L_W$$

here $\mathbf{O}_{C_R \times C_S}$ and $\mathbf{E}_{C_R \times C_S}$ are a zero matrix and a unit matrix in $C_R \times C_S$, respectively.

Assuming $\mathbf{F_R}$ is ignored (*i.e.*, $F_X = F_Y = F_\delta = 0$), the system Eq. (A.1) can be simplified by

$$\dot{\mathbf{q}} = \mathbf{A}\mathbf{q} + \tilde{\mathbf{T}}\mathbf{B}(\mathbf{q})\mathbf{u} \tag{A.6}$$

The above representation is an essential component for the rover motion and is a nonholonomic affine system. Here $\mathbf{F_R}$ can be regarded as the reaction against movement, and therefore $\mathbf{F_R}$ practically acts to decrease the ideal propulsive forces. So, as a primal study for locomotion control, this dissertation considers the simplified control system written in Eq. (A.6).

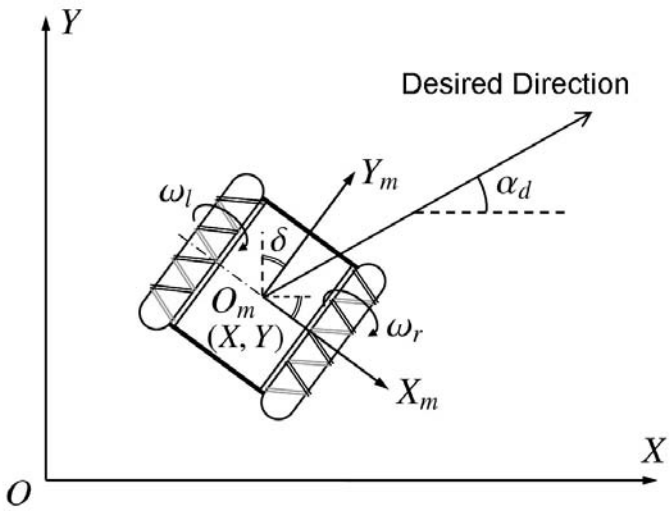

Figure A.1 : Kinematic control model of the Screw Drive Rover.

A.2 Pilot Scheme of Control Law

Based upon Eq. (A.6), ω_r and ω_l can be written as follows.

$$\begin{bmatrix} \omega_r & \omega_l \end{bmatrix}^T = \bar{\mathbf{B}}^{-1}\mathbf{T}\begin{bmatrix} \ddot{X} & \ddot{Y} \end{bmatrix}^T \tag{A.7}$$

where,

$$\bar{\mathbf{B}} = \begin{bmatrix} B_1 & B_2 \\ B_3 & -B_4 \end{bmatrix} \tag{A.8}$$

As a pilot control scheme, the following relation is given for controlling the moving direction as illustrated in Figure A.1.

$$\dot{Y} = \dot{X}\tan\alpha_d \quad \text{where } \dot{X} \neq 0 \tag{A.9}$$

where α_d is a desired angle and is constant.

Thus by differentiating Eq. (A.9), the following control law can be derived for the determination of the controlled input ratio.

$$\ddot{Y} = \ddot{X}\tan\alpha_d \quad \text{where } \ddot{X} \neq 0 \tag{A.10}$$

A.3 Simulation Case Study

The validation of the proposed control scheme is examined by numerical simulation. In the simulation, the desired direction is set to be $\alpha_d = \pi/4\,\text{rad}$. Figure A.2 depicts the simulation result. This indicates the Screw Drive Rover is able to move in the desired direction even though the body consistently rotates. Consequently, it is concluded that the control system is basically controllable in a planar movement.

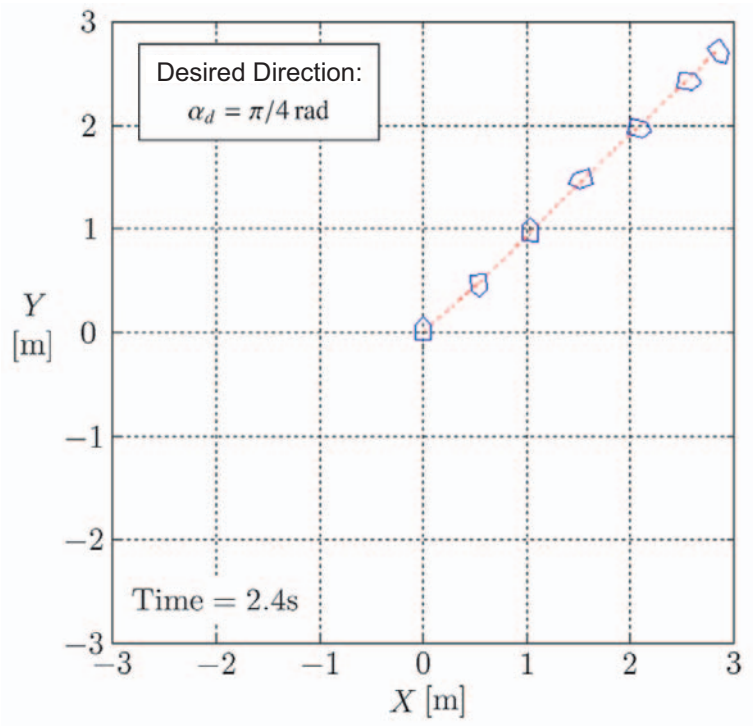

Figure A.2 : Simulation result of motion trajectory with moving direction control $\alpha_d = \pi/4$ rad.

Appendix B Tractive Limitations of Rigid Wheels on Soil

B.1 Identifying Current Situation

In mankind's history, construction of wheels is one of the most outstanding achievements in engineering. Although the exact origin of the wheels is not known, according to a theory, it is believed that wheeled vehicles were first developed in at least between 3500 and 3000 BC. At present, the leading theory is that the wheel was invented by Sumerian more than 5000 years ago. Seen from the Sumerian chariots drawn in Figure B.1, it can be confirmed that Sumerian had used the wheeled vehicles at that time. In general, the wheel is a simple and efficient locomotion gear, and it has thus been applied transportation devices in rough terrain as well as in paved road. While the wheel has broad utility, the wheel has a disadvantage on locomotion in deformable ground such as soft soil, mud or marsh. In particular, wheeled robots often get stuck in soft soil, and then they cannot extricate from the sand trap by themselves. Such immovable situation is a critical issue for the robots to be avoided. This statement determinately exhibits tractive limitations of the wheels on the soil. Therefore, implementation of secure wheeled locomotion in such soil is highly required in an engineering point of view.

Terramechanics focusing on soil-vehicle interaction has taken a considerable role for off-road locomotion on deformable terrain since the mid-20th century. Main targets in terramechanics

Figure B.1 : The Standard of Ur "War" in Sumerian civilization [112].

are basically machines for transportation, agriculture or extraterrestrial investigation. Accumulated findings in terramechanics can provide practical guidelines when discussing locomotion on soft soil such as lunar or martian soil. One of the mainstream approaches in terramechanics is the study on semi-empirical models regarding steady states of wheels and tracks on natural terrain (e.g. [66, 73, 75, 82, 83]). Furthermore, in recent years soil parameter estimation has been also studied from a geological standpoint [84, 89, 95]. Likewise, visual sinkage measurement by a camera [88] or online slip prediction method by motor current [87] has been currently addressed. As technical applications, some have studied slope climbing [86], steering characteristics [72, 76, 90] and slope traversability [94]. Most of them have been commonly discussed based upon the conventional models.

Although the above expansion has been accomplished until now, the tractive limitations of the wheel on the soil is less well understood. The tractive limitations denote an unmovable and a critical state with much slippage, and it should be thus avoided for a mobile robot. Getting stuck in the soil should be avoided for the robots as mentioned previously, and then discussion of the limitations is expected to lead to a solution for that. So this appendix indicates the tractive limitations by using the terramechanics models in an attempt to answer the question "What parameter is a key factor to avoid getting stuck into the soft soil?". In addition to this, an application methodology of the models is also discussed with conventional experimental approaches.

B.2 Terramechanics Model of a Rigid Wheel

Terramechanics contributes to formulate the soil-wheel interaction, including semi-empirical factors. The basic formulae express just static and convergent states, and are generally derived as follows [82].

$$DP_w = r_w b_w \int_{\theta_{wr}}^{\theta_{wf}} (\tau \cos\theta_w - \sigma \sin\theta_w)\, d\theta_w \tag{B.1}$$

$$F_z = r_w b_w \int_{\theta_{wr}}^{\theta_{wf}} (\tau \sin\theta_w + \sigma \cos\theta_w)\, d\theta_w \tag{B.2}$$

$$T_w = r_w^2 b_w \int_{\theta_{wr}}^{\theta_{wf}} \tau\, d\theta_w \tag{B.3}$$

where r_w is wheel radius, b_w is wheel width, θ_w is wheel angle, θ_{wf} is entry angle, θ_{wr} is exit angle, and σ and τ are normal and shear stress of soil, respectively. The wheel is assumed not to deploy any lugs or fins on its surface. These equations calculate drawbar pull DP_w, vertical force F_z and required torque T_w, and are principle parameters of wheel motion. In particular, force equilibrium of F_z and wheel load W must be satisfied.

Next, a wheel slip, which is a principal parameter in elicitation process of the above values, is defined. The wheel slip s_w can be expressed by the ratio of wheel's translational and circumferential velocities as follows [66].

$$s_w = \begin{cases} 1 - \dfrac{v_w}{r_w \omega_w} & \text{if} \quad |r_w \omega_w| \geq |v_w| \quad : 0 \leq s_w \leq 1 \\ \dfrac{r_w \omega}{v_w} - 1 & \text{otherwise} \qquad\qquad : -1 \leq s_w \leq 0 \end{cases} \tag{B.4}$$

where v_w is wheel's translational velocity and ω_w is wheel's angular velocity, and wheel's circumferential velocity is given as $r_w \omega_w$. Here wheel's traveling states are typically divided into self-propelled, driving and braking state. The self-propelled and the driving states introduce $0 \leq s_w \leq 1$, and the braking state $-1 \leq s_w \leq 0$ by Eq. (B.4). In this appendix, the wheel motion under $0 \leq s_w \leq 1$ is elaborated.

Then, the interactive mechanics between the soil and the wheel is described. The diagram of the soil-wheel interaction is illustrated in Figure B.2. Referring to this illustration, wheel angle θ_w is defined as a positive value in a counterclockwise rotation from $\theta_w = 0$ line (see Figure B.2). Let entry angle $\theta_{wf} (\geq 0)$ be geometrically written by using wheel sinkage h_w as follows.

$$\theta_{wf} = \arccos\left(1 - \frac{h_w}{r_w}\right). \tag{B.5}$$

Figure B.3 plots the relationship between θ_{wf} and h_w / r_w. According to this, it is found that, for instance, h_w / r_w becomes approximately 0.29 at $\theta_w = 45\,\text{deg}$. Therefore, angle components, $\sin\theta_w$ for σ and $\cos\theta_w$ for τ, are greatly affected by an increase of h_w.

With respect to the normal stress σ on the wheel surface, the well-known formulation is available as follows [66].

$$\sigma(\theta_w) = \begin{cases} \sigma_{wm} \left(\cos\theta_w - \cos\theta_{wf}\right)^n & \text{if} \quad \theta_{wm} \leq \theta_w \leq \theta_{wf} \\ \sigma_{wm} \left\{ \cos\left[\theta_{wf} - \dfrac{(\theta_w - \theta_{wr})\left(\theta_{wf} - \theta_{wm}\right)}{\theta_{wm} - \theta_{wr}} \right] - \cos\theta_{wf} \right\}^n & \text{otherwise} \end{cases} \tag{B.6}$$

and also,

$$\sigma_{wm} = \left(\frac{k_c}{b_w} + k_\phi\right) r_w^n \tag{B.7}$$

where, as soil parameters, n is pressure sinkage ratio, k_c and k_ϕ are deformation modulus for cohesion stress C and internal friction angle ϕ, respectively. Let the wheel exit angle $\theta_{wr} (\leq 0)$ assume zero [82]. Accordingly, Eq. (B.6) can be simply rewritten as follows.

$$\sigma(\theta_w) = \begin{cases} \sigma_{mw} \left(\cos\theta_w - \cos\theta_{wf}\right)^n & \text{if} \quad \theta_{wm} \leq \theta_w \leq \theta_{wf} \\ \sigma_{mw} \left\{ \cos\left[\theta_{wf} - \dfrac{\theta_w \left(\theta_{wf} - \theta_{wm}\right)}{\theta_{wm}} \right] - \cos\theta_{wf} \right\}^n & \text{otherwise} \end{cases} \tag{B.8}$$

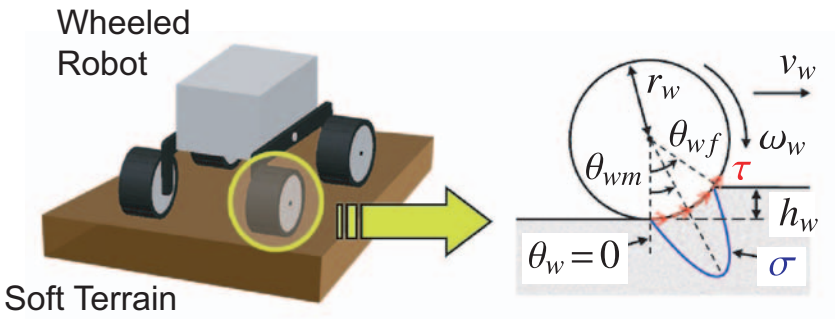

Figure B.2 : Traditional simplified soil-wheel interaction model.

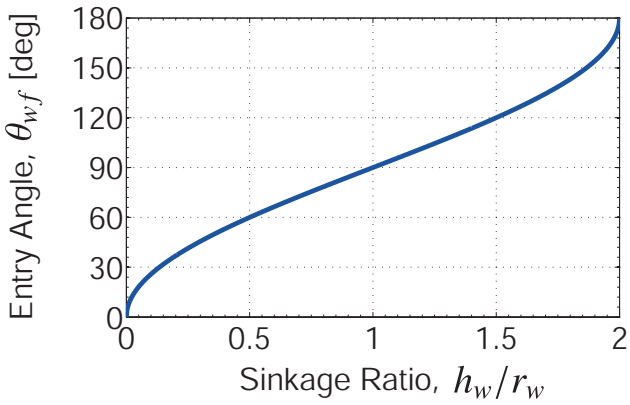

Figure B.3 : Relationship between θ_{wf} and h_w/r_w.

Furthermore, to determine the distribution profile of σ, the ratio of maximum stress angle θ_{wm} and θ_{wf} can be defined as a linear function of s_w as follows [71].

$$\frac{\theta_{wm}}{\theta_{wf}} = c_1 + c_2 s \tag{B.9}$$

where c_1 and c_2 are coefficients defined by soil, and $c_1 \approx 0.4$ and $0 \leq c_2 \leq 0.3$ are generally given by empirically-based data [82, 84].

Most of the terramechanics studies assume that the soil shear stress τ acts on the wheel surface. On the basis of Janosi *et al.* [67, 68], τ of the soft soil can be formulated as follows.

$$\begin{aligned} \tau(\theta_w) &= \tau_{\max}(\theta_w)\,[1-\exp(-j_w/K)] \\ &= \underbrace{(C+\sigma\tan\phi)}_{\text{Shear Strength}}\underbrace{[1-\exp(-j_w/K)]}_{\text{Shear Function}} \end{aligned} \tag{B.10}$$

where $\tau_{\max}$ is soil shear strength, j_w is soil displacement by the wheel and K is soil deformation modulus.

Given the difference of $r_w\omega_w$ and $v\cos\theta_w$ is defined as slip velocity v_{wj}, j_w can be expressed

by the wheel angle θ_w as follows [82].

$$\begin{aligned} j_w(\theta_w) &= \int v_{wj}\, dt \\ &= \int_{\theta_w}^{\theta_{wf}} (r_w \omega_w - v_w \cos\theta_w) \frac{d\theta_w}{\omega_w} \\ &= r_w \left[\theta_{wf} - \theta_w - (1 - s_w)\left(\sin\theta_w - \sin\theta_{wf}\right)\right] \end{aligned} \tag{B.11}$$

B.3 Parametric Analysis based on Terramechanics Model

In this section, the simulation analyses of the terramechanics model are numerically demonstrated. Each parameter dependence to the drawbar pull DP_w is discussed through parametric analyses. According to these analyses, the tractive limitations are discussed from several perspectives.

B.3.1 Fundamental Simulation Conditions

The terramechanics model of the wheel can be outlined by the single wheel test as shown in Figure B.4. The traveling direction of the wheel is fundamentally constrained in forward direction. Also, the simulated terrain is assumed to be dry sand [82, 84]. The parameter conditions of the dry sand in the subsequent analyses are shown in Table B.1. Likewise, nominal parameters of wheel geometry are set to be $r_w = 0.1$ m and $b_w = 0.1$ m respectively. Moreover, based on the past study by Yamakawa *et al.* [92], synthesis sinkage h_w with slip sinkage is calculated by the following equation.

$$h_w = h_{w0} + c_4 s \tag{B.12}$$

where h_{w0} is initial sinkage at $s_w = 0$ and c_4 is a positive coefficient pertaining to the slip. Such tendency of the slip sinkage effect on the wheel has been reported in several literatures [79, 97, 99]. Also, Hegedus [69] has studied the slip sinkage effect by experiments, and then the sinkage increases exponentially with increasing the slip. As for the simulations, the cases of constant sinkage ($h_w = const.$) and variable sinkage by Eq. (B.12) are analyzed. In addition, sinkage ratio h_w/r_w is newly defined for subsequent discussions.

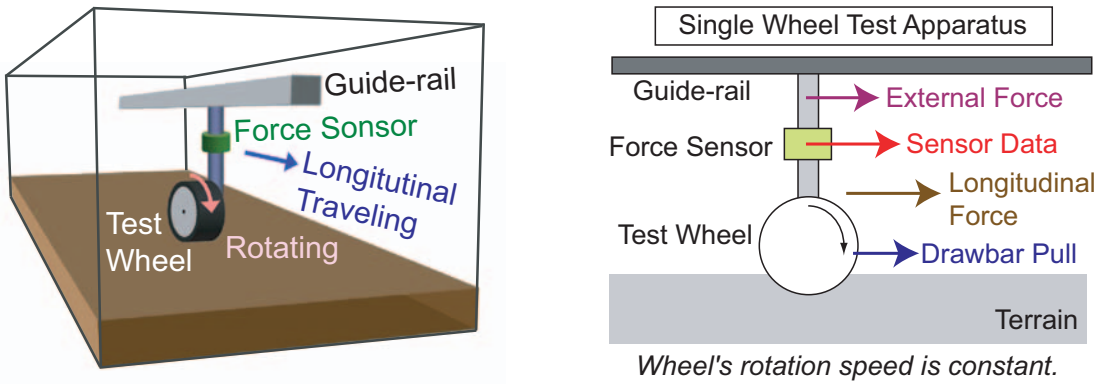

Figure B.4 : Schematic of single wheel test system.

Table B.1 : Nominal parameters of dry sand in simulation analyses [82, 84].

Soil Parameter	Symbol	Value	Unit
Internal Friction Angle	ϕ	28	deg
Cohesion Stress	C	1000	Pa
Pressure-Sinkage Modulus for Internal Friction Angle	k_ϕ	1523.4	kN/m^{n+2}
Pressure-Sinkage Modulus for Cohesion Stress	k_c	900	N/m^{n+1}
Deformation Modulus	K	0.025	m
Pressure-Sinkage Ratio	n	1.1	-
Coefficient for determining the Relative Position of Maximum Radial Stress	c_1	0.4	-
Coefficient for determining the Relative Position of Maximum Radial Stress	c_2	0.15	-

B.3.2 Results and Discussions

Effects of Slip and Sinkage Ratio on Stress Distributions

Simulations are first conducted to analyze dependence properties of slip s_w and sinkage ratio h_w/r_w to the stress distributions. As an example of these simulations, the numerical results under $s_w = 0.2, 0.8$ and $h_w/r_w = 0.2, 0.8$ are depicted in Figure B.5. From these, the tendency that θ_{wm} is proportional to s_w is confirmed as expressed in Eq. (B.9). The maximum values of the stresses do not change with s_w in these results. In the meantime, h_w/r_w affects notably the maximum values, and then they increase more than quadrupled with $h_w/r_w = 0.2 \rightarrow 0.8$. Therefore, it is found that the stresses is governed by h_w/r_w. Moreover, r_w exerts solely the stress equations, and

thus it is concluded that the wheel's geometric radius is a key factor for the stress distributions. Here the other stress distributions under $s_w = 0.2 \sim 0.8$ and $h_w/_w = 0.2 \sim 0.8$ can be summarized in the intermediaries between the states shown in Figure B.5.

Effects of Slip and Wheel Geometry on Shear Function

Simulation analyses with respect to the shear function expressed in Eq. (B.10) are demonstrated. The shear function $\tau/\tau_{\max}$, which is defined as the ratio of the shear stress over the shear strength, is an important index for evaluating the drawbar pull. Figure B.6 plots the effects of s_w and r_w/K on the shear function with constant h_w/r_w (constant θ_{wf}). Seen from this graph, r_w/K is more effective in the change of the shear function than s_w. Given r_w/K affects exponentially the shear function, the increase of the shear function becomes lower with the increase of r_w/K. Thus, since K is an uncontrollable soil parameter, larger r_w should be designed to obtain the enough shear stress on the soil. In contrast with this, it is confirmed that τ does not essentially depend much on s_w itself.

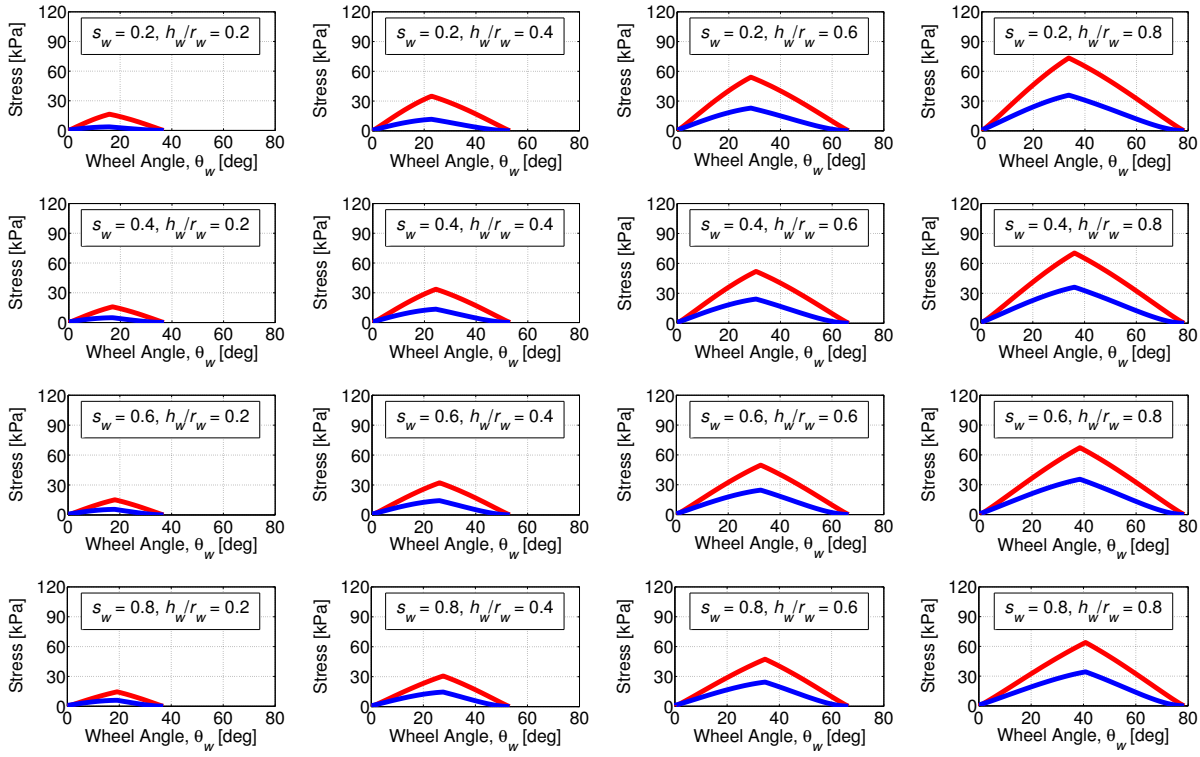

Figure B.5 : Stress distributions along θ_w: — σ, — τ.

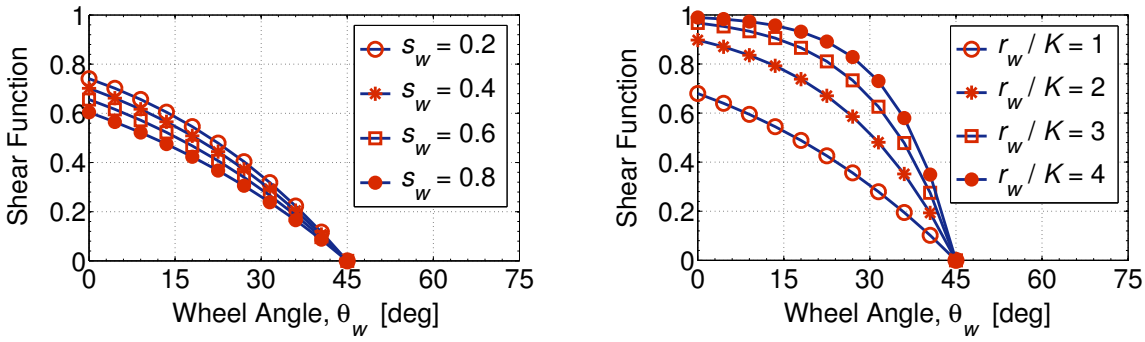

(a) Effect of s_w with $r_w/K = 1$. (b) Effect of r_w/K with $s_w = 0.5$.

Figure B.6 : Shear function along θ_w with constant h_w/r_w.

Effects of Sinkage Ratio on Drawbar Pull and Vertical Force

The drawbar pull DP_w and the vertical force F_z defined by Eqs. (B.1) and (B.2) are fundamental integrated indexes for discussing tractive performance. So this appendix analyzes the dependence of the sinkage ratio h/r to these forces. Figures B.7 and B.8 show the simulation results. While a certain amount of change in DP_w and F_z by s_w can be confirmed, h_w/r_w is obviously a dominant parameter for the forces. The main reason for these results would be that magnitudes of sine and cosine components are reversed once θ_w turns 45deg. These components affect angle components of σ and τ for DP_w, and therefore, these depend much on h_w/r_w because of the relationship in Figure B.3. Likewise, negative DP_w is just the serious state being stuck, and some sort of external forces are needed to move in this situation. Assuming the conventional relationship that F_z is equal to W at any slips in Eq. (B.2), h_w/r_w must slightly decrease with the increase of s_w. However, in the light of the slip sinkage effect in Eq. (B.12), the increase of h_w/r_w pertaining to s_w should become larger. Therefore, the conventional force equilibrium in the vertical direction would contradict this result. At the same time, these simulation analyses reveal the fact that the vertical force balance exerting the sinkage h_w is inconsistent with the empirical outcomes. Further, it is indicated that h_w/r_w depends much on the load W. Then, these results eventually provide an emphasis of wheel's mechanical design, especially the wheel radius r_w and the weight W.

Effects of Slip Sinkage on Drawbar Pull

As the next step, simulations of drawbar pull DP with practical sinkage behavior are analyzed. The result under $h_{w0} = 0.005\,\mathrm{m}$ is depicted in Figure B.10. In particular, DP_w is proportional to s_w at lower c_4 (e.g. $c_4 = 0.015$). Likewise, when c_4 is 0.015, DP becomes zero

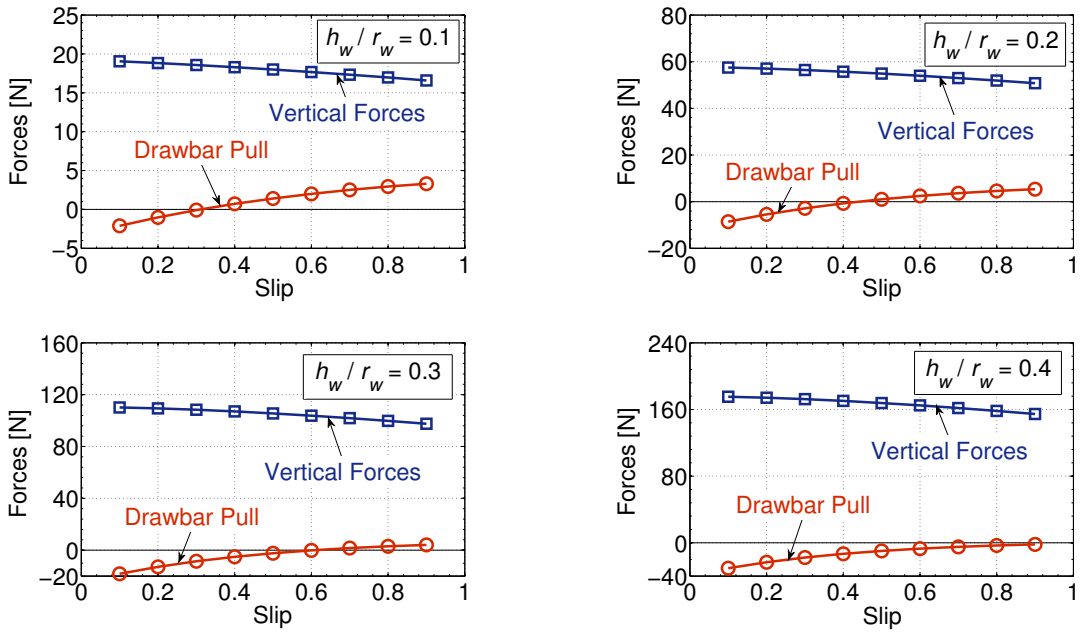

Figure B.7 : Integrated forces vs. slip with constant h_w/r_w.

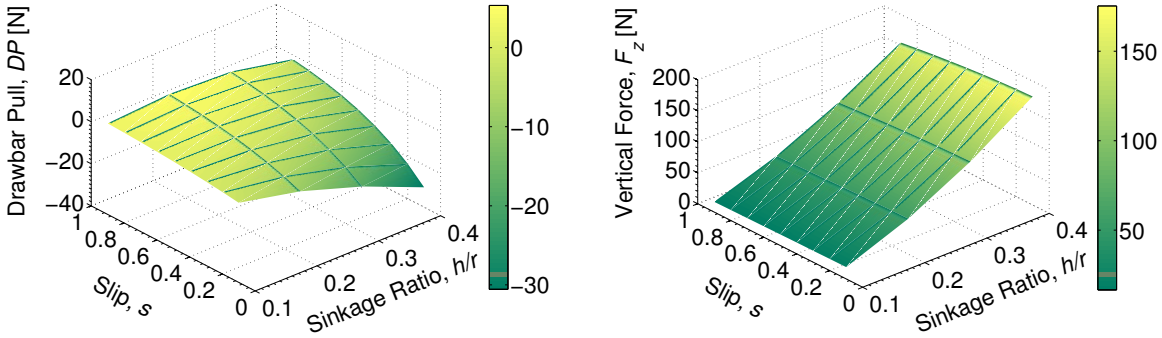

(a) Simulated drawbar pull. (b) Simulated vertical force.

Figure B.8 : Three-dimensional plots of integrated forces vs. slip with constant h_w/r_w.

at neighborhood of $s_w = 0.3$, and thus this proves a steady state can be achieved pertaining to the translational velocity. Moreover, Figure B.10 plots the change of DP_w with respect to s_w at $c_4 = 0.015, 0.03, 0.045$. The critical state that DP_w always indicates less than zero with larger c_4 is confirmed by this result.

Prediction of Tractive Limitations

The tractive limitations are given by a function of the sinkage, especially the sinkage ratio. Figure B.12 plots minimal conditions of h_w/r_w with change of the wheel radius r_w, which satis-

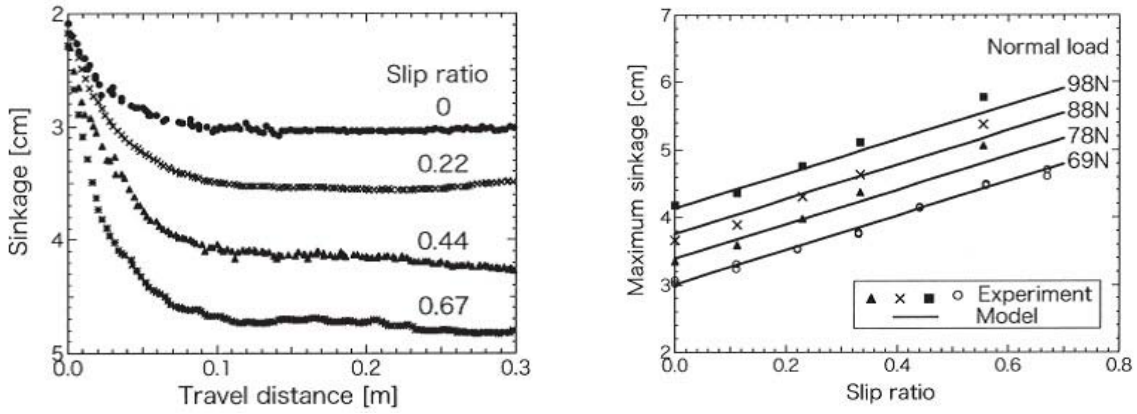

Figure B.9 : Traveling results regarding slip and steady sinkage [92].

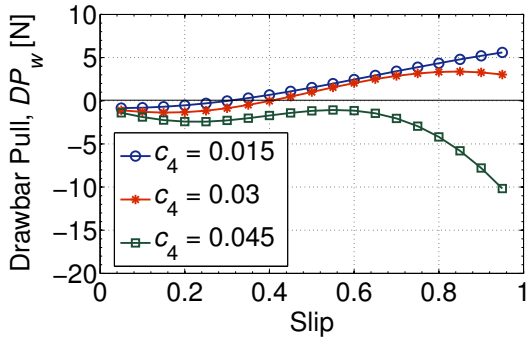

Figure B.10 : Drawbar pull vs. slip with various c_4.

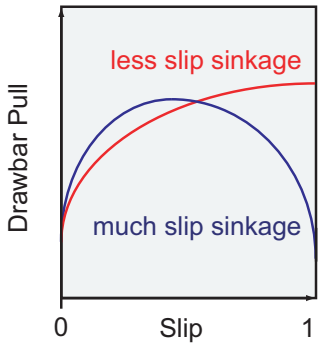

Figure B.11 : Description of slip-traction characteristics.

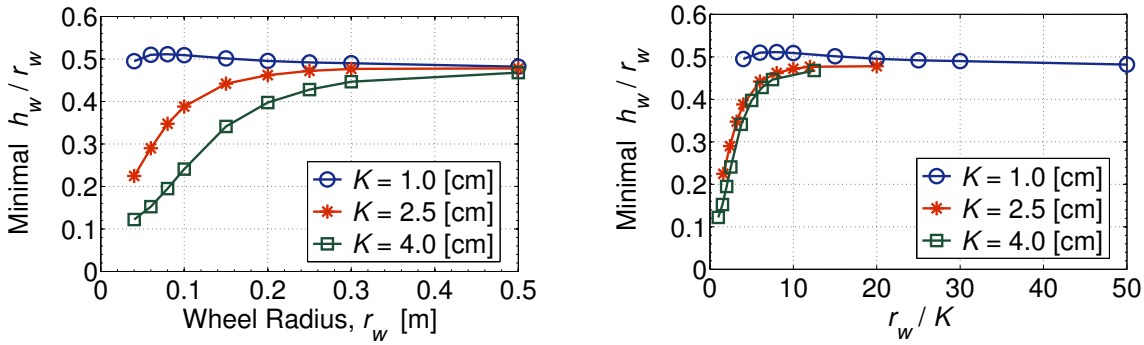

(a) Effect of K. (b) Effect of r_w/K.

Figure B.12 : Minimal h_w/r_w satisfying $DP_w \leq 0$ with various r_w targeting dry sand.

fies negative drawbar pull $DP_w \leq 0$, where targeted terrain is assumed to be dry sand. Seen from Figure B.12(a), it can be confirmed that the minimal h_w/r_w basically increases with an increase of r_w. This denotes that a larger wheel radius is capable of better tractive performance in the dry

Table B.2 : Nominal parameters of lunar soil in simulation analyses [81, 84].

Soil Parameter	Symbol	Value	Unit
Internal Friction Angle	ϕ	35	deg
Cohesion Stress	C	170	Pa
Pressure-Sinkage Modulus for Internal Friction Angle	k_ϕ	814.4	kN/m^{n+2}
Pressure-Sinkage Modulus for Cohesion Stress	k_c	1379	N/m^{n+1}
Deformation Modulus	K	0.0178	m
Pressure-Sinkage Ratio	n	1.0	-
Cohesion for determining the Relative Position of Maximum Radial Stress	c_1	0.4	-
Cohesion for determining the Relative Position of Maximum Radial Stress	c_2	0.15	-

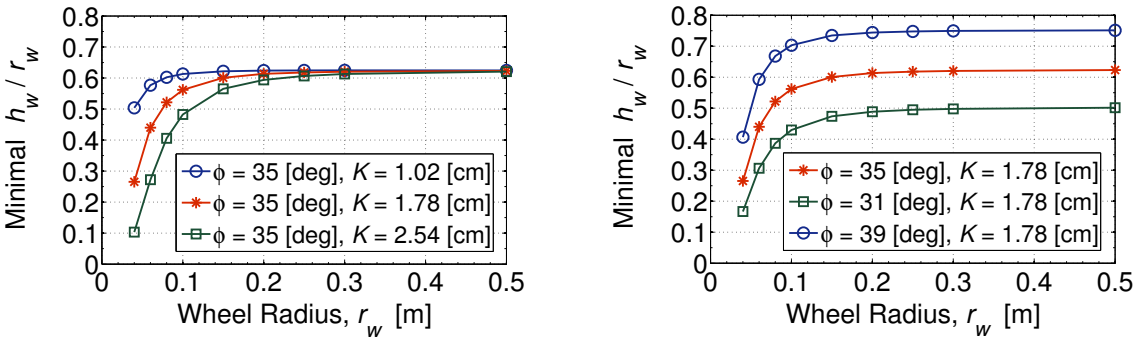

(a) Effect of K. (b) Effect of ϕ.

Figure B.13 : Minimal h_w/r_w satisfying $DP_w \leq 0$ with various r_w targeting lunar soil.

sand. In the meantime, this advantage is saturated beyond a certain r_w (e.g. the minimal h_w/r_w becomes an almost same value at $r_w > 0.5$m in Figure B.12(a)). With normalizing r_w/K, the characteristics of the minimal h_w/r_w become marked as shown in Figure B.12(b).

Furthermore, simulations targeting lunar soil [81] are demonstrated to investigate the limitations. The nominal property of the lunar soil is shown in Table B.2. Figure B.13 depicts the simulation results with the lunar soil. In accordance with Figure B.13(a), similar tendencies of the limitations with the dry sand can be shown. On the other hand, the additional simulation results graphed in Figure B.13(b) indicate the effect of ϕ on the limitations. It is concluded that higher frictional soil poses a better tractive performance. Consequently, the theoretical prediction of the wheel's limitations in the steady state is achieved by the sinkage condition.

B.4 Compliance of Interaction Model with Single Wheel Test

B.4.1 Apparatus of Conventional Single Wheel Test

Figure B.4 illustrates the fundamental configuration of the single wheel test. The wheel is connected to the guide-rail attaching a force sensor. The guide-rail can actively shift back and forth, and also displace freely in a vertical direction without resistance. Accordingly, the total force, governing the wheel motion, can be represented as the summation of the drawbar pull obtained by the wheel and the external force affected by the guide-rail. Consequently, various slip states are able to be performed.

B.4.2 Key Suggestion of Test Outcomes and Their Implications

As mentioned previously, the system motion obtained through the test includes the extra forces by the guide-rail. In this apparatus, obtained data are the sensor output, vertical and horizontal displacements, and the extra force from guide-rail. Assuming the wheel travels horizontally with constant angular velocity and sinkage, the correlation of all data will be resulted as shown in Figure B.14. This indicates the self-propelled state of the wheel is limited in a certain area, which the external force becomes zero on the basis of Figure B.14.

Further to this, a single-wheeled robot is a distant idea for development of actual wheeled robots. On the basis of a mobility performance, a multi-wheeled robot such as four-wheeled

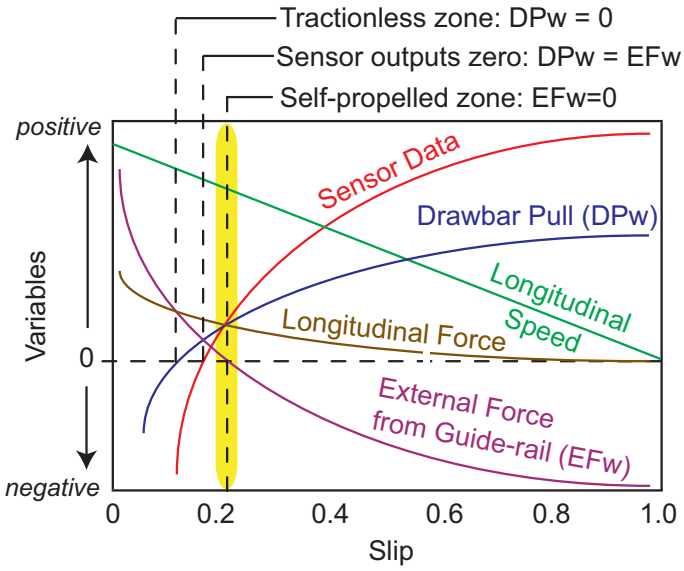

Figure B.14 : Tendency resulted by single wheel test.

or six-wheeled is practical configuration. Hence, most of the data acquired by the test simulate the one wheel of the multi-wheeled robot with a difference between wheel motions. Given an uncertainty by the dynamic behavior of the sinkage with slip change, what a positive traction is able to be generated under lower slip and envisaged sinkage is important for the wheel's mechanical design.

B.5 Summary

This appendix theoretically investigates the tractive limitations of the wheeled robot in the soil based on the conventional terramechanics models. Although all the analyses represent just steady states, the static tractive limitations for the wheels can be newly indicated by evaluating negative drawbar pull. In particular, it is found that the wheel radius and the weight become important factors in order to avoid getting stuck in the soil. Also, the application methodology of the terramechanic findings to the actual mobile robot is described by regarding as the one wheel of the multi-wheeled robot. The subject of this appendix is providing an essential idea to discuss wheeled robots in deformable terrain, and therefore, the results would contribute to the development of such robot. Furthermore, as future works, traveling experiments of wheels are necessary to evaluate and validate the theoretical predictions.

Appendix C Comparative Vehicle Model

C.1 Wheeled Vehicle Model

The terramechanics model of the soil-wheel interaction is described in Appendix B. For the wheeled vehicle model, the model can be applied and a four wheeled vehicle is assumed .

C.2 Tracked Vehicle Model

Traditionally, a tracked vehicle is suitable for traveling on yielding terrain due to a contact surface and a soil shear trajectory of a track [85]. Such tracked locomotion system thus has applied construction machines or tanks for primarily traveling in difficult terrains, and has been discussed in the terramechanic discipline as well as the wheeled one. In the rigid track model illustrated in Figure C.1, the soil thrust F_t is given from the bottom portion, which is l_t in length [82]. Moreover, the soil compaction resistance R_t militates against the anterior portion of the track [75]. Consequently, the drawbar pull DP_t of the track is expressed as follows.

$$DP_t = F_t - R_t \tag{C.1}$$

$$F_t = (b_t l_t C + W_t \tan\phi)\left\{1 - 2\left(\frac{K}{s_t l_t}\right)^2\left[1 - \left(1 + \frac{s_t l_t}{K}\right)\exp\left(-\frac{s_t l_t}{K}\right)\right]\right\} \tag{C.2}$$

$$R_t = \frac{k_c + b_t k_\phi}{n+1} h^{n+1} \tag{C.3}$$

(a) Illustration of vehicle model. (b) Track-soil interaction model.

Figure C.1 : Rigid tracked vehicle model.

Appendix D Penetration Equation

Young [147] has proposed penetration equations of penetrator systems. The equations are called Sandia Equation, and the penetration depth D_p is derived as follows.

$$D_p = 1.8 \times 10^{-5} K_{sp} S_p N_p \left(\frac{m_p}{A_p} \right)^{0.7} (V_p - 30.5) \tag{D.1}$$

where this equation assumes the impact velocity V_p is more than 61 meters per second and the total mass m_p is more than 2 kilograms. Also, the ground surface is assumed to be flat and penetration angle is normal direction to the surface. Here K_{sp} is a correction coefficient, S_p is a penetrability index, N_p is a geometric parameter of the penetrator's nose, A_p is the representative surface area of the penetrator as illustrated in Figure D.1(a). Given penetrating surface is soil, K_{sp} is defined as follows.

$$K_{sp} = \begin{cases} 0.27 \cdot m_p^{0.4} & : m_p < 27\,\mathrm{kg} \\ 1.0 & : m_p \geq 27\,\mathrm{kg} \end{cases} \tag{D.2}$$

In general, lunar and planetary penetrators are required to be small and lightweight, and therefore, the above condition of $m_p < 27\,\mathrm{kg}$ is assumed. With respect to coefficient N_p, the nose section of actual penetrators is not pointed in practice. Given the penetrator has a blunt nose, N_p is given as follows.

$$N_p = 0.125 \left(\frac{L_{np} + L'_{np}}{d_p} \right) + 0.56 \tag{D.3}$$

where L_{np} is the actual nose length, L'_{np} is the ideal nose length and d_p is the diameter of the penetrator as illustrated in Figure D.1(a). Consequently, D_p can be rewritten by

$$D_p = 4.86 \times 10^{-6} S_p N_p \left(\frac{m_p^{1.1}}{A_p^{0.7}} \right) (V_p - 30.5)\,. \tag{D.4}$$

Based upon Eq. (D.4), assuming the impact velocity V_p and the soil's property S_p ($4 \sim 10$: compacted soil $\sim$ soft soil [147]), D_p can be analyzed by numerical simulations. Figure D.1(b) depicts the simulation result. The fundamental simulation parameters are shown in Table D.1. From Figure D.1(b), if $m_p = 10\,\mathrm{kg}$ and $V_p = 150\,\mathrm{m/s}$ (540 km/hr), D_p reaches just 1.6 meters below surface of the soft soil layer. It is said that $D_p = 2\,\mathrm{m}$ is a limit of practical penetrators with sensors from the standpoint of their structural durability.

Table D.1 : Simulation parameters of penetrator model.

Penetrator's Parameter	Symbol	Value	Unit
Actual nose length	L_{np}	0.08	m
Ideal nose length	L'_{np}	0.1	m
Boring diameter	d_p	0.1	m
Total mass	m_p	10.0	kg
Representative surface area	$A_p \left(= \frac{\pi d_p^2}{4}\right)$	7.85×10^{-3}	m^2

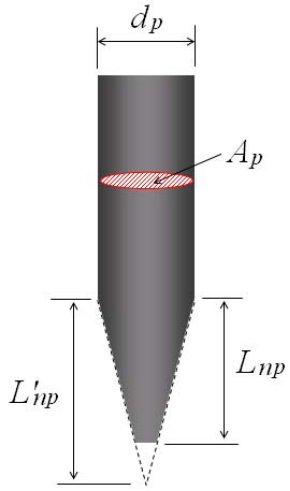

(a) Simplified penetrator model.

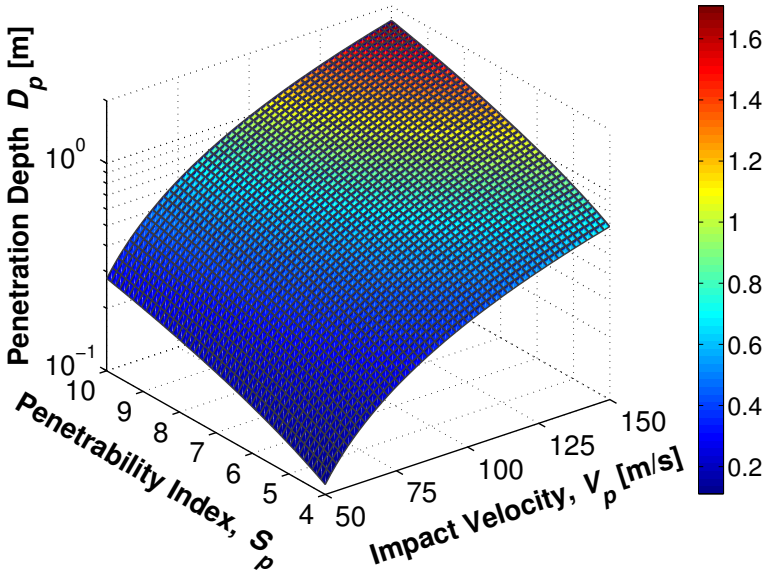

(b) Simulation result.

Figure D.1 : Cone penetration by Sandia equation.

Bibliography

Literature related to “Space Science and Space Missions”

[1] S. Fields, A Study of Friction and Adhesion in Simulated Lunar Vacuum, *Proceedings of the 7th Annual Working Group on Extraterrestrial Resources, NASA SP 229*, pp. 101-105, 1970.

[2] W. Roepke, Friction Test in Simulated Lunar Vacuum, *Proceedings of the 7th Annual Working Group on Extraterrestrial Resources, NASA SP 229*, pp. 107-111, 1970.

[3] G.H. Heiken, D.T. Vaniman and B.M. French, *Lunar Sourcebook: A User’s Guide to the Moon*, Cambridge University Press, NY, 1991.

[4] T. Sugano and K. Heki, High Resolution Lunar Gravity Anomaly Map from the Lunar Prospector Line-of-Sight Acceleration Data, *Earth Planets Space*, vol. 56, no. 1, pp. 81-86, 2004.

[5] P. Ulivi and D.M. Harland, *Lunar Exploration: Human Pioneers and Robotic Surveyors*, Springer, Paxis Publishing, UK, 2004.

[6] J. Watanabe, *Latest Science of the Moon* (in Japanese), NHK Books, Japan, 2008.

[7] S. Tanaka, H. Shiraishi, M. Kato and T. Okada, The Science Objectives of the SELENE-II Mission as the post SELENE Mission, *Advances in Space Research*, vol. 42, no. 2, pp. 394-401, 2008.

[8] C.R. Neal, The Moon 35 Years after Apollo: What’s Left to Learn?, *Chemie der Erde - Geochemistry*, vol. 69, no. 1, pp. 3-43, 2009.

[9] S. Ulamec, J. Biele and E. Trollope, How to Survive a Lunar Night, *Planetary and Space Science*, vol. 58, no. 14-15, pp. 1985-1995, 2010.

[10] http://catless.ncl.ac.uk/Risks/9.24.html#subj3 (accessed on January 5, 2011)

[11] http://www.planetary.org/blog/article/00000987/ (accessed on January 5, 2011)

[12] http://www.jaxa.jp/press/2005/11/20051112_hayabusa_j.html (in Japanese, accessed on January 5, 2011)

[13] http://marsrovers.jpl.nasa.gov/mission/status_spiritAll_2009.html#sol1900 (accessed on January 5, 2011)

[14] http://www.nasa.gov/mission_pages/mer/news/mer20100126.html (accessed on January 5, 2011)

Literature related to "Screwed Pile, Auger and Drilling Technique"

[15] O. Schweisgut, *Earth Auger*, U.S. Patent 1523143, January 13th, 1950.

[16] L.J. Applegate, *Earth Boring Machine*, U.S. Patent 2509410, May 30th, 1925.

[17] R. Teale, The Concept of Specific Energy of Rock Drilling, *International Journal of Rock Mechanics and Mining Sciences*, vol. 2, pp. 57-73, 1965.

[18] S. Hata and N. Ito, Study on Rotary Drilling Mechanism: 2nd Report (in Japanese), *Proceedings of the 9th Annual Meeting, Kansai Chapter of the Japan Society of Civil Engineers*, Kyoto, Japan, pp. 223-224, 1967.

[19] The Society of Geotechnical Engineering ed., Soil Mechanics and Foundation Engineering: Recent Construction Techniques (in Japanese), *The Society of Geotechnical Engineering*, Japan, 1967.

[20] H. Raiba, Specific Energy as a Criterion for Drill Performance Prediction, *International Journal of Rock Mechanics and Mining Science & Geomechanics Abstracts*, vol. 19, pp. 39-42, 1982.

[21] A. Ghaly, A. Hanna and M. Hanna, Installation Torque of Screw Anchors in Dry Sand, *Journal of the Japanese Geotechnical Society: Soils and Foundations*, vol. 31, no. 2, pp. 77-92, 1991.

[22] E. Saeki and H. Ohki, A Study of the Screwed Pile -The Results of Installation and Loading Tests and Analysis of Penetration Mechanism-, *Nippon Steel Technical Report*, no. 82(7), pp. 42-50, 2000.

[23] J.W. Slatter, J.P. Seidel and W. Kingwell, A Proposed Model for Soil/Auger Interaction during Installation of Screw Piling Augers, *Proceedings of the 25th Annual Meeting and Eighth International Conference and Exposition , Deep Foundations Institute*, New York, NY, #897, 2000.

[24] H. Isohata, Historical Study on Iron Pile Foundations and Screw Piles (in Japanese), *Proceedings of the Japan Society of Civil Engineers*, vol. 744, no. 4, pp. 139-150, 2003.

[25] W.P. Hong and S.G. Chai, The Skin Friction Capacity of SDA (Separated Doughnut Auger) Pile, *Proceedings of the 13th International Offshore and Polar Engineering Conference*, Honolulu, HI, pp. 740-745, 2003.

[26] F.E. Dupriest and W. L. Koederitz, Maximizing Drill Rates with Real-Time Surveillance of Mechanical Specific Energy, *Proceedings of the 2005 SPE/IADC Drilling Conference*, Amsterdam, The Netherlands, #92194, 2005.

[27] W.L. Koederitz and J. Weis, A Real-Time Implementation of MSE, *Proceedings of the AADE 2005 National Technical Conference and Exhibition*, Houston, TX, #AADE-05-NTCE-66, 2005.

[28] F. Ohsugi, T. Tsuchiya, M. Shimada and K. Yoshida, Pile Installation Tests of Screwed Piles in A Callibration Chamber (in Japanese), *Journal of Structural and Construction Engineering, Transaction on AIJ*, no. 591(5), pp. 69-75, 2005.

[29] M. Kouda *et al.*, Fundamental Study on Penetration and Bearing Capacity of Screw Pile with Helical Wing (in Japanese), *Journal of Structural and Construction Engineering, Transaction on AIJ*, no. 601(3), pp. 91-98, 2006.

[30] H. Fukada, M. Ootsuka, Y. Tanaka and Y. Shioi, Discharging Characteristics by Screw Auger of Gravel Drain Pile (in Japanese), *JSCE Journal of Construction Engineering and Management*, vol. 62, no. 2, pp. 203-212, 2006.

[31] T. Tsuchiya, F. Nakazawa and M. Shimada, Study on Penetration Mechanism of Screw Pile Based on Soil Movement Around Helical Wing (in Japanese), *AIJ Journal of Technology Design*, vol. 13, no. 25(6), pp. 73-76, 2007.

[32] T. Tsuchiya, F. Nakazawa, F. Ohsugi, M. Shimada, Model Tests of Installation and Bearing Capacity of Screwed Piles (in Japanese), *Journal of Structural and Construction Engineering, Transaction on AIJ*, no. 620(10), pp. 75-80, 2007.

[33] M.J. Kaiser, A Survey of Drilling Cost and Complexity Estimation Models, *International Journal of Petroleum Science and Technology*, vol. 1, no. 1, pp. 1-22, 2007.

Literature related to “Screw Drive Locomotion/Screw Mechanism”

[34] T.J. Wells, *Improvement in the Manner of Constructing and of Propelling Steamboats, Denominated the “Buoyant Spiral Propeller”*, U.S. Patent 2400, December 23rd, 1841.

[35] J.A. Morath, *Agricultural Machine*, U.S. Patent 635501, October 24th, 1899.

[36] O.A. Hollis, *Tractor*, U.S. Patent 1069875, August 12th, 1913.

[37] S.M. Code, *Amphibious Vehicle*, U.S. Patent 1646611, October 25th, 1927.

[38] B.N. Cole, Inquiry into Amphibious Screw Traction, *Proceedings of the Institution of Mechanical Engineers 1847-1982*, vol. 175, no. 19, pp. 919-940, 1961.

[39] U.S. Army, *Final Report of Military Potential Test of Marsh Screw Amphibian*, USATECOM Project, no. 7-5-0524-01-9, Fort Lee, VA, 1964.

[40] M. Neumeyer and B. Jones, The Marsh Screw Amphibian, *Journal of Terramechanics*, vol. 2, no. 4, pp. 83-88, 1965.

[41] S.J. Knight, E.S. Rush and B.G. Stinson, Trafficability Tests with the Marsh Screw Amphibian, *Journal of Terramechanics*, vol. 2, no. 4, pp. 31-50, 1965.

[42] J.J. De Bakker, *De Bakker Amphibian Vehicle*, U.S. Patent 3333563, August 1st, 1967.

[43] H. Dugoff and I. Ehrlich, Model Tests of Buoyant Screw Rotor Configurations, *Journal of Terramechanics*, vol. 4, no. 3, pp. 9-22, 1967.

[44] W.K. Fales, D.W. Amick and B.G. Schreiner, The Riverine Utility Craft (RUC), *Journal of Terramechanics*, vol. 8, no. 3, pp. 23-38, 1972.

[45] E.S. Rush and W.E. William, *Evaluation of the Marsh Screw Amphibian (MSA)*, Technical Report: Evaluation of Herbicide Application Platforms for Use in Aquatic Plant Control, no. A-77-1, Washington, DC, 1977.

[46] C.A. Pickover, Mathematics and Beauty: A Sampling of Spirals and 'Strange' Spirals in Science, Nature and Art, *Leonardo*, vol. 21, no. 2, pp. 173-181, 1988.

[47] Z. Kembłowski, J. Sèk and P. Budzyński The Concept of a Rotational Rheometer with Helical Screw Impeller, *Rheologica Acta*, vol. 27, no. 1, pp. 82-91, 1988.

[48] M. Sendoh, N. Ajiro, K. Ishiyama, M. Inoue and K. I. Arai, Effect of Machine Shape on Swimming Properties of the Spiral-Type Magnetic Micro-Machine, *IEEE Transactions on Magnetics*, vol. 35, no. 5, pp. 3688-3690, 1999.

[49] A.W. Roberts, The Influence of Granular Vortex Motion on the Volumetric Performance of Enclosed Screw Conveyors, *Powder Technology*, vol. 104, no. 1, pp. 56-67, 1999.

[50] C. Rorres, The Turn of the Screw: Optimal Design of an Archimedes Screw, *ASCE Journal of Hydraulic Engineering*, vol. 126, no. 1, pp. 72-80, 2000.

[51] K. Ishiyama, M. Sendoh, A. Yamazaki and K. Arai, Swimming Micro-machine Driven by Magnetic Torque, *Sensors and Actuators A: Physical*, vol. 91, no. 1-2, pp. 141-144, 2001.

[52] A. Yamazaki, M. Sendoh, K. Ishiyama, T. Hayase and K. Arai, Three-dimensional Analysis of Swimming Properties of a Spiral-type Magnetic Micro-machine, *Sensors and Actuators A: Physical*, vol. 105, no. 1, pp. 103-108, 2003.

[53] T. Koetsier and H. Blauwendraat, The Archimedean Screw-Pump: A Note on Its Invention and the Development of the Theory, *Proceedings of the 2004 International Symposium on History of Machines and Mechanisms*, Cassino, Italy, pp. 181-194, 2004.

[54] M.E. Rentschler *et al.*, Modeling, Analysis, and Experimental Study of In Vivo Wheeled Robotic Mobility, *IEEE Transactions on Robotics*, vol. 22, no. 2, pp. 308-321, 2006

[55] M.E. Rentschler, S.M. Farritor and K.D. Iagnemma, Mechanical Design of Robotic In Vivo Wheeled Mobility, *ASME Journal of Mechanical Design*, vol. 129, pp. 1037-1045, 2007.

[56] A. Fuchs and H. Zangl, Measuring Flow Parameters of Particulate and Powdery Solids in Industrial Transportation Processes, *International Journal on Smart Sensing and Intelligent Systems*, vol. 1, no. 2, pp. 388-402, 2008.

[57] M. Ogata, Y. Shimotsuma and N. Shiotsu, Origin of the Concept of Screws (in Japanese), *Transactions of the Japan Society of Mechanical Engineers, Series C*, vol. 74, no. 746, pp. 2356-2362, 2008.

[58] P.J. Owen and P.W. Cleary, Prediction of Screw Conveyor Performance Using the Discrete Element Method (DEM), *Powder Technology*, vol. 193, no. 3, pp. 274-288, 2009.

[59] S. Yim and D. Jeon, Capsular Microrobot Using Directional Friction Spiral, *Proceedings of the 2009 IEEE International Conference on Robotics and Automation*, Kobe, Japan, pp. 4444-4449, 2009.

[60] M. Shikanai *et al.*, Development of a Robotic Endoscope that Locomotes in the Colon with Flexible Helical Fins, *Proceedings of the 31st Annual International Conference of the IEEE/EMBS*, Minneapolis, MN, pp. 5126-5129, 2009.

[61] T.C. Lexen, *Screw Driven Mobile Base*, U.S. Patent 20090044990, February 19th, 2009.

[62] J. Lee, B. Kim and Y. Hong, A Flexible Chain-based Screw Propeller for Capsule Endoscopes, *International Journal of Precision Engineering and Manufacturing*, vol. 10, no. 4, pp. 27-34, 2009.

[63] Q. Liu *et al.*, Development of a Spiral Propulsion Mechanism in Wetlands-Relation between Torque and Load, *Memoirs of the Muroran Institute of Technology*, vol. 59, pp. 133-135, 2010.

[64] L. Ju *et al.*, Experimental Results of a Novel Amphibian Solution for Aquatic Robot, *Proceedings of the 2010 IEEE International Conference on Robotics and Automation*, Anchorage, AK, pp. 2261-2266, 2010.

[65] M. Ceccarelli, *The Mechanics of Archimedes Towards Modern Mechanism Design, in "The Genius of Archimedes -- 23 Centuries of Influence on Mathematics, Science and Engineering"*, Springer, The Netherlands, pp. 177-187, 2010.

Literature related to "Locomotion Mechanics on Soil (Terramechanics)"

[66] M.G. Bekker, *Theory of Land Locomotion*, University of Michigan Press, MI, 1956.

[67] Z.J. Janosi and B. Hanamoto, The Analytical Determination of Drawbar Pull as A Function of Slip for Tracked Vehicle, *Proceedings of the 1st International Conference on Terrain-Vehicle Systems*, Turin, Italy, pp. 707-736, 1961.

[68] Z.J. Janosi, *Performance Analysis of a Driven Non-Deflecting Tire in Soil*, U.S. Army Tank-Automotive Center, Land Locomotion Laboratory, Warren, MI, 1963.

[69] E. Hegedus, Pressure Distribution and Slip-Sinkage Relationship Under Driven Rigid Wheels, *U.S. Army Tank-Automotive Center, Land Locomotion Laboratory*, no. 88, Warren, MI, 1963.

[70] J.Y. Wong and A.R. Reece, Prediction of Rigid Wheel Performance based on the Analysis of Soils - Wheel Stresses Part I. Performance of Driven Rigid Wheels, *Journal of Terramechanics*, vol. 4, no. 1, pp. 81-98, 1967.

[71] O. Onafeko and A.R. Reece, Soil Stresses and Deformations beneath Rigid Wheels, *Journal of Terramechanics*, vol. 4, no. 1, pp. 59-80, 1967.

[72] H. Schwanghart, Lateral Forces on Steered Tyres in Loose Soil, *Journal of Terramechanics*, vol. 5, no. 1, pp. 9-29, 1968.

[73] M.G. Bekker, *Introduction of Terrain-Vehicle Systems*, University of Michigan Press, MI, 1969.

[74] N. Costes and W. Trautwein, Elastic Loop Mobility System: A New Concept for Planetary Exploration, *Journal of Terramechanics*, vol. 10, no. 1, pp. 89-104, 1973.

[75] S. Hata, *Construction Machinery* (in Japanese), Kashima Publishing, Japan, 1987.

[76] D.A. Crolla and A.S.A. El-Razaz, A Review of the Combined Lateral and Longitudinal Force Generation of Tyres on Deformable Surfaces, *Journal of Terramechanics*, vol. 24, no. 3, pp. 199-225, 1987.

[77] X.L. Wang, T. Tanaka and M. Yamazaki, Study on Soil-Lugged Wheel Interaction: Part 1 -Dynamic Behaviour of a Lugged Wheel- (in Japanese), *Journal of the Japanese Society of Agriculture Machinery*, vol. 51, no. 3, pp. 33-40, 1989.

[78] A. Oida, A. Satoh, H. Itoh and K. Triratanasirichai, Three-dimensional Stress Distributions on a Tire-Sand Contact Surface, *Journal of Terramechanics*, vol. 28, no. 4, pp. 319-330, 1991.

[79] Z. Jide, W. Zhixin and L. Jude , The Way to Improve the Trafficability of Vehicles on Sand, *Proceedungs of the 5th European Conference on Terrain-Vehicle Systems*, Budapest, Hungary, pp. 121-126, 1991.

[80] J.A. Okello, Prediction of the Force Distribution between the Soil and a Pneumatic Wheel, *Journal of Agricultural Engineering Research*, vol. 51, pp. 249-262, 1992.

[81] B.E. Wallace and N.S. Rao, Engineering Elements for Transportation on the Lunar Surface, *Applied Mechanics Review*, vol. 46, no. 6, pp. 301-312, 1993.

[82] J.Y. Wong, *Theory of Ground Vehicles (3rd ed.)*, John Wiley & Sons, Inc., NY, 2001.

[83] T. Muro and J. O'Brien, *Terramechanics*, A.A. Balkema Publishers, The Netherlands, 2004.

[84] K. Iagnemma and S. Dubowsky, *Mobile Robots in Rough Terrain*, Springer, NY, 2005.

[85] J.Y. Wong and W. Huang, Wheels vs. Tracks -A Fundamental Evaluation from the Traction Perspective, *Journal of Terramechanics*, vol. 43, no. 1, pp. 27-42, 2006.

[86] A. Miwa, G. Ishigami, K. Nagatani and K. Yoshida, Terramechanics-Based Analysis on Climbing Ability of a Lunar/Planetary Exploration Rover (in Japanese), *Proceedings of the 11th Robotics Symposia*, Saga, Japan, pp. 514-519, 2006.

[87] L. Ojeda, D. Cruz, G. Reina and J. Borenstein, Current-Based Slippage Detection and Odometry Correction for Mobile Robots and Planetary Rovers, *IEEE Transactions on Robotics*, vol. 22, no. 2, pp. 366-378, 2006.

[88] C.A. Brooks, K.D. Iagnemma and S. Dubowsky, Visual Wheel Sinkage Measurement for Planetary Rover Mobility Characterization, *Autonomous Robots*, vol. 21, no. 1, pp. 55-64, 2006.

[89] S. Hutangkabodee, Y.H. Zweiri, L.D. Seneviratne and K. Althoefer, Soil Parameter Identification for Wheel-terrain Interaction Dynamics and Traversability Prediction, *International Journal of Automation and Computing*, vol. 3, no. 3, pp. 244-251, 2006.

[90] G. Ishigami, A. Miwa, K. Nagatani and K. Yoshida, Terramechanics-based Model for Steering Maneuver of Planetary Exploration Rovers on Loose Soils, *Journal of Field Robotics*, vol. 24, no. 3, pp. 233-250, 2007.

[91] H. Nakashima and Y. Takatsu, Analysis of Tire Tractive Performance on Deformable Terrain by Finite Element-Discrete Element Method, *Journal of Computational Science and Technology*, vol. 2, no. 4 pp. 423-434, 2008.

[92] J. Yamakawa, O. Yoshimura and K. Watanabe, Development of Tire Model on Dry Sand by Model Size Experiment: First Report (in Japanese), *Transactions of the Society of Automotive Engineers of Japan*, vol. 39, no. 6, pp. 41-46, 2008.

[93] K. Iizuka, Y. Kunii and T. Kubota, Study on Wheeled Forms of Lunar Robots Considering Elactic Characteristic for Traversing Soft Terrain: Effect of Elastic Wheel Considering in Interaction Between Wheel and Soft Soil (in Japanese), *Transactions of the Japan Society of Mechanical Engineers, Series C*, vol. 74, no. 748, pp. 2962-2967, 2008.

[94] G. Ishigami, K. Nagatani and K. Yoshida, Slope Traversal Controls for Planetary Exploration Rover on Sandy Terrain, *Journal of Field Robotics*, vol. 26, no. 3, pp. 264-286, 2009.

[95] L.E. Ray, Estimation of Terrain Forces and Parameters for Rigid-Wheeled Vehicles, *IEEE Transactions on Robotics*, vol. 25, no. 3, pp. 717-726, 2009.

[96] M. Scharringhausen, D. Beermann, O. Krömer and L. Richter, Wheel-Soil Interaction Model for Planetary Rover Vehicles, *Proceedings of the 11th European Conference of the International Society for Terrain-Vehicle Systems*, Bremen, Germany, #P75, 2009.

[97] M. Lyasko, Slip Sinkage Effect in Soil-Vehicle Mechanics, *Journal of Terramechanics*, vol. 47, no. 1, pp. 21-31, 2010.

[98] V.K. Tiwari, K.P. Pandey and P.K. Pranav, A Review on Traction Prediction Equations, *Journal of Terramechanics*, vol. 47, no. 3, pp. 191-199, 2010.

[99] L. Ding, H. Gao, Z. Deng and J. Tao, Wheel Slip-Sinkage and its Prediction Model of Lunar Rover, *Journal of Central South University of Technology* , vol. 17, no. 1, pp. 129-135, 2010.

Literature related to “Soil Mechanics”

[100] E. Hegedus, A Simplified Method for the Determination of Bulldozing Resistance, *Land Locomotion Research Laboratory, U.S. Army Tank Automotive Command Report*, vol. 61, Warren, MI, 1960.

[101] R.W. Clough, The Finite Element Method in Plane Stress Analysis, *Proceedings of the 2nd ASCE Conference on Electronic Computation*, Pittsburg, PA, USA, pp. 345-378, 1960.

[102] A. Schofield and P. Wroth, *Critical State Soil Mechanics*, McGraw-Hill Education, UK, 1968.

[103] P.A. Cundall and O.D.L. Strack, A Discrete Numerical Model for Granular Assemblies, *Géotechnique*, vol. 29, no. 1, pp. 47-65, 1979.

[104] M. Hirota, T. Oshima and Y. Sugihara, Shear Test of Powder Bed in the Tensile Stress Regions (in Japanese), *Journal of the Society of Powder Technology*, vol. 18, no. 9, pp. 678-680, 1981.

[105] J. Carter, J. Booker and S. Yeung, Cavity Expansion in Cohesive Frictional Soils, *Géotechnique*, vol. 36, no. 3, pp. 349-358, 1986.

[106] K. Ito, S. Katsuki, N. Ishikawa, S. Abe and T. Nakamura, Shear Resistance of Filled Material in Check Dam (in Japanese), *Journal of the Japan Society of Erosion Control Engineering*, vol. 50, no. 1, pp. 3-14, 1997.

[107] H. Kanamori, S. Udagawa, T. Yoshida, S. Matsumoto and K. Takagi, Properties of Lunar Soil Simulant Manufactured in Japan, *Proceedings of the 6th International Conference and Exposition on Engineering Construction, and Operations in Space*, Albuquerque, NM, USA, pp. 462-468, 1998.

[108] S.H. Yu, *Cavity Expansion Methods in Geomechanics*, Kluwer Academic Publishers, UK, 2000.

[109] O. Kusakabe, *Soil Mechanics* (in Japanese), Korona Publishing, Japan, 2004.

[110] Lunarant producted by WEL RESEARCH Co., Ltd. (http://www.wel.co.jp/product.html, accessed on January 5, 2011)

[111] Report on Inorganic Recyclable Resource (Coal Ash & Iron and Steel Slag), Chapter 2, Hokkaido, Japan, 2004. (in Japanese, http://edb.hokkaido-ies.go.jp/edb/junkan/junkankyo_manual/kensetsu-manual15/kensetsu-manual15-2-1.pdf, accessed on January 5, 2011)

Literature related to “Field Robotics and Space Exploration Rover”

[112] http://www.britishmuseum.org/explore/highlights/highlight_objects/me/t/the_standard_of_ur.aspx (accessed on January 5, 2011)

[113] S. Kassel, *Lunokhod-1 Soviet Lunar Surface Vehicle*, LAND Report, no. R-802-ARPA, The Land Corporation, Santa Monica, CA, 1971.

[114] B. Ilon, *Directionally Stable Self-propelled Vehicle*, U.S. Patent 3746112, July 17th, 1971.

[115] A Roving Lunokhod Explores the Moon, 53: Society for Science & the Public, *Science News*, vol. 103, no. 4, 1973. (http://www.jstor.org/stable/pdfplus/3957956, accessed on January 5, 2011)

[116] A. Kemurdjian *et al.*, Soviet Developments of Planet Rovers in Period of 1964∼1990, *Journal of the Robotics Society of Japan*, vol. 12, no. 7, pp. 75-83, 1994. (translated into Japanese)

[117] L. Matthies *et al.*, Mars Microrover Navigation: Performance Evaluation and Enhancement, *Autonomous Robotics*, vol. 2, no. 4, 1995.

[118] A.L. Kemurdjian, Planet Rover as an Object of the Engineering Design Work, *Proceedings of the 1998 IEEE International Conference on Robotics and Automation*, Leuven, Belgium, pp. 140-145, 1998.

[119] K. Yoshida, Robotics for Space Exploration (in Japanese), *Journal of the Society of Instrument and Control Engineers*, vol. 39, no. 9, pp. 576-580, 2000.

[120] K. Kotay and D. Rus, The Inchworm Robot: A Multi-Functional System, *Autonomous Robots*, vol. 8, no. 1, pp. 53-69, 2000.

[121] T. Yoshimitsu, T. Kubota and I. Nakatani, New Mobility System of Exploration Rover for Small Planetary Bodies (in Japanese), *Journal of the Robotics Society of Japan*, vol. 18, no. 2, pp. 292-299, 2000.

[122] B. Kennedy *et al.*, LEMUR: Legged Excursion Mechanical Utility Rover, *Autonomous Robots*, vol. 11, pp. 201-205, 2001.

[123] R. Roncoli and J. Ludwinski, Mission Design Overview for the Mars Exploration Rover Mission, *Proceedings of the 2002 AIAA/AAS Astrodynamics Specialist Conference and Exhibit*, Monterey, CA, USA, #AIAA 2002-4823, 2002.

[124] S.W. Squyres *et al.*, Athena Mars Rover Science Investigation, *Journal of Geophysical Research*, vol. 108, no. E12, p.8062, 2003.

[125] B. Harrington and C. Voorhees, The Challenges of Designing the Rocker-Bogie Suspension for the Mars Exploration Rover, *Proceedings of the 37th Aerospace Mechanisms Symposium*, Houston, TX, pp. 185-196, 2004.

[126] S.W. Squyres *et al.*, Two Years at Meridiani Planum: Results from the Opportunity Rover, *Science*, vol. 313, no. 5792, pp. 1403-1407, 2006. (http://www.sciencemag.org/cgi/content/full/313/5792/1403, accessed on January 5, 2011)

[127] T. Nakamura, T. Kato, T. Iwanaga and Y. Muranaka, Development of a Peristaltic Crawling Robot Based on Earthworm Locomotion, *Journal of Robotics and Mechatronics*, vol. 18, no. 3, pp. 229-304, 2006.

[128] P. Ulivi and D.M. Harland, *Robotic Exploration of the Solar System: Part 1 The Golden Age 1957-1982*, Springer, Paxis Publishing, UK, 2007.

[129] B. Wilcox *et al.*, ATHLETE: A Cargo Handling and Manipulation Robot for the Moon, *Journal of Field Robotics*, vol. 24, no. 5, pp. 421-434, 2007.

[130] A. Gfrerrer, Geometry and Kinematics of the Mecanum Wheel, *Computer Aided Geometric Design*, vol. 25, no. 9, pp. 784-791, 2008.

[131] E. Rohmer, G. Reina, G. Ishigami, K. Nagatani and K. Yoshida, Action Planner of Hybrid Leg-Wheel Robots for Lunar and Planetary Exploration, *Proceedings of the 2008 IEEE/RSJ International Conference on Intelligent Robots and Systems*, Nice, France, pp. 3902-3907, 2008.

[132] K. Tadakuma *et al.*, Crawler Vehicle with Circular Cross-Section Unit to Realize Sideways Motion, *Proceedings of the 2008 IEEE/RSJ International Conference on Intelligent Robots and Systems*, Nice, France, pp. 2422-2428, 2008.

[133] C.M. Gifford, A. Agah, B.L. Carmichael, U.B. Wade and I. Ruiz, Seismic TETwalker Mobile Robot Design and Modeling, *Proceedings of the IEEE International Conference on Technologies for Practical Robot Applications 2008*, Woburn, MA, pp. 7-12, 2008.

[134] S. Ransom, O. Krömer and M. Lückemeier, Planetary Rovers with Mecanum Wheels, *Proceedings of the 10th ESA Workshop on Advanced Space Technologies for Robotics and Automation*, Noordwijk, The Netherlands, #14-04, 2008.

[135] A. Schiele *et al.*, Nanokhod Exploration Rover: A Rugged Rover Suited for Small, Low-Cost, Planetary Lander Mission, *IEEE Robotics & Automation Magazine*, vol. 15, no. 2, pp. 96-107, 2008.

[136] S. Wakabayashi, H. Sato and S. Nishida, Design and Mobility Evaluation of Tracked Lunar Vehicle, *Journal of Terramechanics*, vol. 46, no. 3, pp. 105-114, 2009.

[137] R.A. Kerr, Mars Rover Trapped in Sand, But What Can End a Mission?, *Science*, vol. 324, no. 5930, p.998, 2009. (http://www.sciencemag.org/cgi/content/full/324/5930/998, accessed on January 5, 2011)

[138] S.W. Squyres *et al.*, Exploration of Victoria Crater by the Mars Rover Opportunity, *Science*, vol. 324, no. 5930, pp. 1058-1061, 2009. (http://www.sciencemag.org/cgi/content/full/324/5930/1058, accessed on January 5, 2011)

[139] H. Kinoshita, K. Nagatani and K. Yoshida, Development of a Small-sized Leg-Track Robot to Traverse on Loose Slopes and Irregular Terrains (in Japanese), *Proceedings of the 2010 JSME Annual Conference on Robotics and Mechatronics*, Asahikawa, Japan, #2A1-E25, 2010.

Literature related to "Lunar and Planetary Sampling Technique"

[140] M.V. Winnendael and G. Visentin, Nanokhod Microrover Heading Towards Mars, *Proceedings of the 5th International Symposium on Artificial Intelligence, Robotics and Automation in Space*, Noordwijk, The Netherlands, pp. 69-76, 1999.

[141] T. Muff, L. Johnson, R. King and B. M. Duke, A Prototype Bucket Wheel Excavator for the Moon, Mars and Phobos, *Space Technology and Applications International Forum 2004, AIP Proceedings*, Albuquerque, NM, vol. 699, pp. 967-974, 2004.

[142] S. Mukherjee, P. Brian, B. Glass, J. Guerrero and S. Stanley, Technologies for Exploring the Martian Subsurface, *Proceedings of the 2006 IEEE Aerospace Conference*, Big Sky, MT, #1349, 2006.

[143] E. Re *et al.*, EXOMARS: Two Meters Depth Drilling, *Proceedings of the 59th International Astronautical Congress*, Glasgow, Scotland, #A3.3-B7, 2008.

[144] J. Crabtree, J.L. Klosky, R. Gash and D. Miller, Helical Ancors: Lateral Resistance For Shaping The Lunar Surface, *Proceedings of the Earth & Space 2008*, Long Beach, CA, #7458, 2008.

[145] P.W. Bartlett, D. Wettergreen, W.L. Whittaker, Design of the Scarab Rover for Mobility & Drilling in the Lunar Cold Traps, *Proceedings of the 9th International Symposium on Artificial Intelligence, Robotics and Automation in Space*, Los Angeles, CA, #m145, 2008.

[146] R. Bonitz *et al.*, The Phoenix Mars Lander Robotic Arm, *Proceedings of the 2009 IEEE Aerospace Conference*, Big Sky, MT, #1695, 2009.

Literature related to "Penetration Technology"

[147] C.W. Young, Penetration Equations, *SANDIA Laboratories Report*, #SAND97-2426, 1997.

[148] T. Nakajima *et al.*, Lunar Penetrator Program: LUNAR-A, *Acta Astronautica*, vol. 39, no. 1-4, pp. 111-119, 1996.

[149] Y.A. Surkov and R.S. Kremnev, Mars-96 Mission: Mars Exploration with the Use of Penetrators, *Planetary Space Science*, vol. 46, no. 11, pp. 1689-1696, 1998.

[150] H. Mizutani, A. Fujimura, M. Hayakawa, S. Tanaka and H. Shiraishi, Understanding of Lunar Interior by Penetrators (in Japanese), *Journal of the Japan Society fot Precision Engineering*, vol. 63, no. 10, pp. 1346-1350, 1997.

[151] R.D. Lorenza, J.E. Moersch, J.A. Stone, A.R. MorganJr and S.E. Smrekar, Penetration Tests on the DS-2 Mars Microprobes: Penetration Depth and Impact Accelerometry, *Planetary and Space Science*, vol. 48, pp. 419-436, 2000.

[152] Y. Gao, A. Ellery, M. Jaddou, J. Vincent and S. Eckersley, Planetary Micro-Penetrator Concept Study with Biomimetric Drill and Sampler Design, *IEEE Transactions on Aerospace and Electronics Systems*, vol. 43, no. 3, pp. 875-885, 2007.

Literature related to “Subsurface Drilling Robot”

[153] K. Tomio, H. Igarashi and A. Harada, A Proposal of the Earthworm Rover for Exploring the Moon (in Japanese), *Proceedings of the Annual Conference of the Japanese Society for the Science of Design*, vol. 46, pp. 316-317, 1999.

[154] T. Kudo, K. Yoshida, Basic Examen by Mole-Type Moon Excavation Robot (in Japanese), *Proceedings of the 183th Symposium, Tohoku Chapter of the Society of Instrument and Control Engineers*, Tokyo, Japan, #183-6, 1999.

[155] L. Richter, H. Kochan, V. Gromov and P. Coste, The Development of the “Mole with Sampling Mechanism” Subsurface Sampler, *Proceedings of the 6th ESA Workshop on Advanced Space Technologies for Robotics and Automation*, Noordwijk, The Netherlands, #3.5a-3, 2000.

[156] K. Tateyama, An Idea for a Tunnel Boring Machine without Thrust Force (in Japanese), *Terramechanics*, vol. 20, pp. 29-32, 2000.

[157] K. Yoshida, T. Kudo, Y. Kawakatsu, T. Yokoyama and M. Sonoyama, Development of a Mole-like Robot for Lunar Subserface Exploration (in Japanese), *Proceedings of the 2000 JSME Annual Conference on Robotics and Mechatronics*, Kumamoto, Japan, #1P1-07-019, 2000.

[158] K. Tomio, H. Igarashi and A. Harada, The Robot Using Movement Mechanism of Earthworm (in Japanese), *Proceedings of the Annual Conference of the Japanese Society for the Science of Design*, vol. 47, pp. 198-199, 2000.

[159] W. Zimmerman, R. Bonitz and J. Feldman, Cryobot: An Ice Penetrating Robotic Vehicle for Mars and Europa, *Proceedings of the 2001 IEEE Aerospace Conference*, Big Sky, MT, vol. 1, pp. 311-323, 2001.

[160] N. Mizuno and K. Yoshida, Development of a Robot Prototype for Excavation and Exploration of the Moon and Planet (in Japanese), *Proceedings of the 199th Symposium, Tohoku Chapter of the Society of Instrument and Control Engineers*, Miyagi, Japan, #199-3, 2001.

[161] L. Richter *et al.*, Development and Testing of Subsurface Sampling Devices for the Beagle 2 Lander, *Planetary and Space Science*, vol. 50, no. 9, pp. 903-913, 2002.

[162] K. Yoshida *et al.*, Development of Mole-type Robot for Lunar/Planetary Sub-Surface Exploration, and its Performance Evaluation (in Japanese), *Proceedings of the 20th Annual Conference of Robotics Society of Japan*, Osaka, Japan, #1J35, 2002.

[163] K. Watanabe, S. Shimoda, T. Kubota and I. Nakatani, A Mole-Type Drilling Robot for Lunar Subsurface Exploration, *Proceedings of the 7th International Symposium on Artificial Intelligence, Robotics and Automation in Space*, Nara, Japan, #AS-7, 2003.

[164] S.P. Gorevan *et al.*, Strategies for Future Mars Exploration: An Infrastructure for the Near and Longer Term Future Exploration of the Subsurface of Mars, *Proceedings of the 6th International Conference on Mars*, Pasadena, CA, #3196, 2003.

[165] L. Richter, P. Coste, V. Gromov and A. Grzesik, The Mole with Sampling Mechanism (MSM)- Technology Development and Payload of Beagle 2 Mars Lander, *Proceedings of the 8th ESA Workshop on Advanced Space Technologies for Robotics and Automation*, Noordwijk, The Netherlands, #I-11, 2004.

[166] R. Campaci *et al.*, Design and Optimization of A Terrestrial Guided Mole for Deep Subsoil Exploration-Boring Performance Experimental Analysis, *Proceedings of the 8th International Symposium on Artificial Intelligence, Robotics and Automation in Space, (ESA SP-603)*, Munich, Germany, #4a-1, 2005.

[167] Y. Liu, B. Weinberg and C. Mavroidis, Design and Modeling of the NU Smart Space Drilling System (SSDS), *Proceedings of the 10th ASCE Aerospace Division International Conference Engineering, Construction, and Operations in Challenging Environments (Earth&Space 2006)*, vol. 188, #96, Houston, TX, 2006.

[168] Y. Liu, B. Weinberg and C. Mavroidis, Mechanical Design and Modeling of A Robotic Planetary Drilling System, *Proceedings of the ASME 2006 International Design Engineering Technical Conference & Computers in Engineering Conference*, Philadelphia, PA, #DETC2006-99699, 2006.

[169] T.M. Myrick and S. Gorevan, *Self-Propelled Instrumented Deep Drilling System*, U.S. Patent 7055625, June 6th, 2006.

[170] C.R. Stoker, A. Gonzales, J.R. Zavaleta, Moon/Mars Underground Mole, *Proceedings of the 2007 NASA Science Technology Conference*, Adelphi, MD, #C10P1, 2007.

[171] S. Yasuda and K. Komatsu, Regolith Drilling Mechanism using Reaction Torque (in Japanese), *Proceedings of the 2008 JSME Annual Conference on Robotics and Mechatronics*, Nagano, Japan, #2P2-A20, 2008.

[172] T. Seidl *et al.*, Bio-inspiration from Plants' Roots, *ARIADNA Study 06/6301*, 2008.

[173] S. Yasuda, *Autonomous Excavation Apparatus*, U.S. Patent 20090188137, July 30th, 2009.

[174] Y. Bar-Cohen and K. Zacny, *Drilling in Extreme Environments*, Wiley-VCH, Weinheim, Germany, 2009.

[175] S. Yasuda and K. Komatsu, Research for Regolith Drilling Mechanism Using Reactive Torque (in Japanese), *Proceedings of the 18th Space Engineering Conference*, Tokyo, Japan, #D3, 2010.

[176] B. Mazzolai *et al.*, A Miniaturized Mechatronic System Inspired by Plant Roots for Soil Exploration, *IEEE/ASME Transactions on Mechatoronics*, vol. 16, no. 2, pp. 201-212, 2011.

[177] A. Koller-Hodac *et al.*, Actuated Bivalve Robot Study of the Burrowing Locomotion in Sediment, *Proceedings of the 2010 IEEE International Conference on Robotics and Automation*, Anchorage, Alaska, USA, pp. 1209-1214, 2010.

[178] H. Omori, T. Murakami, H. Nagai, T. Nakamura and T. Kubota, An Earth Auger as Excavator for Planetary Underground Explorer Robot Using Peristaltic Crawling, *Proceedings of the 10th International Symposium on Artificial Intelligence, Robotics and Automation in Space*, Sapporo, Japan, pp. 784-789, 2010.

[179] T. Murakami, H. Omori, H. Nagai and T. Nakamura, Development of Lunar Underground Explorer Robot using Peristaltic Crawling of Earthworm (in Japanese), *Proceedings of the 28th Annual Conference of Robotics Society of Japan*, Nagoya, Japan, #RSJ2010AC3G2-6, 2010.

[180] S. Yasuda and K. Komatsu, Research of Sensor Burying Mechanism (in Japanese), *Proceedings of the 54th Symposium on Space Sciences and Technology*, Shizuoka, Japan, #JSASS-2010-4405, 2010.

[181] R.A. Russel, CRABOT: A Biomimetic Burrowing Robot Designed for Underground Chemical Source Location, *Advanced Robotics*, vol. 25, no. 1-2, pp. 119-134, 2011.

Publications

Journal Papers

- Kenji Nagaoka, Takashi Kubota, Masatsugu Otsuki and Satoshi Tanaka, “An Experimental Study on Contra-Rotor Screw Drilling Mechanism: Effective Screw Mechanism for Lunar Subsurface Exploration Robot” (in Japanese), *Transactions of the Japan Society of Mechanical Engineers, Series C*, vol. 75, no. 758, pp. 2295-2300, 2009.
- Kenji Nagaoka, Takashi Kubota, Masatsugu Otsuki and Satoshi Tanaka, “Experimental Analysis of Screw Drilling Mechanism for Lunar Robotic Subsurface Exploration”, *Advanced Robotics*, vol. 24, no. 8-9, pp. 1127-1147, 2010.

Reviewed International Conference Presentations

- Kenji Nagaoka, Takashi Kubota, Ichiro Nakatani and Satoshi Tanaka, “Drilling Mechanism of Autonomous Burrowing Robot for Lunar Subsurface Exploration”, *9th International Symposium on Artificial Intelligence, Robotics and Automation in Space*, #m063, 2008.
- Kenji Nagaoka, Takashi Kubota and Satoshi Tanaka, “Experimental Study on Autonomous Robotic Screw Burrower for Lunar and Planetary Subsurface Exploration”, *2008 IEEE/RSJ International Conference on Intelligent Robotics and Systems*, pp. 4104-4109, 2008.
- Kenji Nagaoka, Takashi Kubota, Masatsugu Otsuki and Satoshi Tanaka, “Robotic Screw Explorer for Lunar Subsurface Investigation: Dynamics Modelling and Experimental Validation”, *14th International Conference on Advanced Robotics*, #28, 2009.
- Kenji Nagaoka and Takashi Kubota, “Analytic Study on Screw Drilling Mechanism”, *2009 IEEE International Conference on Robotics and Biomimetics*, pp. 1579-1584, 2009.

- Kenji Nagaoka and Takashi Kubota, "Modeling and Analysis on Exploration Rover with Screw Drive Mechanism over Loose Soil", *10th International Symposium on Artificial Intelligence, Robotics and Automation in Space*, pp. 162-169, 2010.
- Kenji Nagaoka and Takashi Kubota, "Maneuverability of Mobile Robot Driven by Archimedean Screw Units on Sand", *Joint 9th Asia-Pacific ISTVS Conference and Annual Meeting of the Japanese Society for Terramechanics*, #086-0042, 2010.
- Kenji Nagaoka, Masatsugu Otsuki, Takashi Kubota and Satoshi Tanaka, "Terramechanics-based Propulsive Characteristics of Mobile Robot Driven by Archimedean Screw Mechanism on Soft Soil", *2010 IEEE/RSJ International Conference on Intelligent Robots and Systems*, pp. 4946-4951, 2010.

Reviewed National Conference Presentations

- Kenji Nagaoka, Takashi Kubota and Satoshi Tanaka, "Non-Reaction Excavation Mechanism for Subsurface Exploration Robot" (in Japanese), *13th Robotics Symposia*, pp. 224-229, 2008.
- Kenji Nagaoka, Takashi Kubota, Masatsugu Otsuki and Satoshi Tanaka, "Development of Subsurface Burrowing Explorer Using Screw Mechanism: Derivation of Theoretical Model Based on Soil Mechanics" (in Japanese), *14th Robotics Symposia*, pp. 173-178, 2009.
- Kenji Nagaoka and Takashi Kubota, "Mobility of Screw Drive Rover on Soft Ground Based on Soil Interaction Model" (in Japanese), *15th Robotics Symposia*, pp. 173-178, 2010.
- Kenji Nagaoka, Takashi Kubota and Kojiro Iizuka, "Trafficability Characterization of an Archimedean Screw Unit on Sand" (in Japanese), *16th Robotics Symposia*, 2011. (*to appear*)

National Conference Presentations

- Kenji Nagaoka, Keisuke Watanabe, Masatsugu Otsuki, Satoshi Tanaka and Takashi Kubota, "Primal Study on Burrowing Subsurface Exploration Robot" (in Japanese), *7th Space Science Symposium*, #P3-43, 2006.
- Kenji Nagaoka, Edmond So, Takashi Kubota, Masatsugu Otsuki and Satoshi Tanaka, "Study on Subsurface Exploration Robot" (in Japanese), *2007 JSME Annual Conference on Robotics and Mechatronics*, #2A2-M06, 2007.

- Kenji Nagaoka, Satoshi Tanaka and Takashi Kubota, “Study on Excavation Mechanism for Lunar Subsurface Exploration by Burrowing Robot”, *17th Workshop on JAXA Astrodynamics and Flight Mechanics*, pp. 380-385, 2007.
- Kenji Nagaoka and Takashi Kubota, “N-RDM System of Burrowing Robot for Lunar Subsurface Exploration” (in Japanese), *25th Annual Conference of the Robotics Society of Japan*, #1K23, 2007.
- Kenji Nagaoka, Takashi Kubota, Masatsugu Otsuki and Satoshi Tanaka, “Study on Drilling Robot for Subsurface Investigation on the Moon” (in Japanese), *8th Space Science Symposium*, #P5-11, 2008.
- Kenji Nagaoka, Takashi Kubota, Masatsugu Otsuki and Satoshi Tanaka, “Burrowing Screw Robot for Lunar and Planetary Subsurface Exploration” (in Japanese), *2008 JSME Annual Conference on Robotics and Mechatronics*, #2P2-A22, 2008.
- Kenji Nagaoka, Masatsugu Otsuki and Takashi Kubota, “Study on Screw Rover Specialized for Locomotion on Lunar Loose Soil” (in Japanese), *2009 JSME Annual Conference on Robotics and Mechatronics*, #1A2-F17, 2009.
- Kenji Nagaoka, Takashi Kubota, Masatsugu Otsuki and Satoshi Tanaka, “Development of Lunar Exploration Rover Using Screw Propulsion Units: Note on Dynamic Behavior and Moving Direction Control”, *19th Workshop on JAXA Astrodynamics and Flight Mechanics*, pp. 143-148, 2009.
- Kenji Nagaoka and Takashi Kubota, “An Empirical Review on Mobile Rover Using Screw Drive Mechanism for Lunar Exploration” (in Japanese), *10th Space Science Symposium*, #P3-43, 2010.
- Kenji Nagaoka, Noriaki Mizukami, Masatsugu Otsuki and Takashi Kubota, “Study on Terramechanics Application to Wheeled Robot in Rough Terrain” (in Japanese), *2010 JSME Annual Conference on Robotics and Mechatronics*, #2P2-F14, 2010.
- Kenji Nagaoka, Takashi Kubota and Satoshi Tanaka, “Maneuverability Analysis of Screw Drive Rover on Soft Terrain”, *20th Workshop on JAXA Astrodynamics and Flight Mechanics*, 2010. (in press)
- Kenji Nagaoka and Takashi Kubota, “Interaction Model between Helical Screw Propulsion Unit and Soil”, *2011 JSME Annual Conference on Robotics and Mechatronics*, 2011. (to appear)

Co-authored International Conference Presentations

- Takashi Kubota, Kenji Nagaoka, Satoshi Tanaka and Taro Nakamura, "Earth-worm Typed Drilling Robot for Subsurface Planetary Exploration", *2007 IEEE International Conference on Robotics and Biomimetics*, pp. 1394-1399, 2007.
- Takashi Kubota, Kenji Nagaoka, Masatsugu Otsuki and Satoshi Tanaka, "Autonomous Burrowing Robot for Lunar Subsurface Exploration", *59th International Astronautical Congress*, #IAC-08-A3.2.INT9, 2008.
- Takashi Kubota, Kenji Nagaoka and Yasuharu Kunii, "Intelligent Explorer with Smart Manipulator and Drilling Mechanism for Lunar or Planetary Exploration", *12th International Conference on Engineering, Science, Construction, and Operations in Challenging Environments (Earth and Space 2010)*, #83, 2010.
- Takashi Kubota, Kenji Nagaoka and Edmond So, "Robotics Technology for Planetary Surface Exploration", *2010 IEEE International Conference on Robotics and Automation, Workshop on Planetary Rover*, #W14-10, 2010.

The Graduate University for Advanced Studies (Sokendai)
School of Physical Sciences
Department of Space and Astronautical Science
JAPAN